UNIVERSITY OF NAIROBI

MODELING AND SIMULATION OF SOLAR-ASSISTED DUAL-SOURCE HEAT PUMP SYSTEM WITH UNDERGROUND THERMAL STORAGE FOR SPACE HEATING AND COOLING

BY

FABIAN CHIDUBEM EZE

I80/57289/2020

A Thesis Submitted in Fulfillment of the Requirements for Award of the Degree of Doctor of Philosophy in Physics of the University of Nairobi

September 2024

DECLARATION

I declare that this thesis is my original work and has not been submitted elsewhere for examination, award of a degree, or publication. Where other people's work or my own work has been used, this has properly been acknowledged and referenced in accordance with the University of Nairobi's requirements.

Signature  Date **September 4, 2024**

Fabian Chidubem Eze

I80/57289/2020

Department of Physics

Faculty of Science and Technology

University of Nairobi

This thesis is submitted for examination with our approval as research supervisors:

	Signature	Date
Prof. Julius M. Mwabora Department of Physics University of Nairobi P. O. Box, 30197 – 00100, Nairobi, Kenya mwabora@uonbi.ac.ke		**5th September 2024**
Prof. Julius Maima Ogola Department of Mechanical and Manufacturing Engineering University of Nairobi P. O. Box, 30197 – 00100, Nairobi, Kenya julius.ogola@uonbi.ac.ke		5th September 2024
Dr. Kyoung-ho Lee Principal Researcher, Renewable Energy System Laboratory Korea Institute of Energy Research 152 Gajeong-ro, Yuseong-gu, Daejeon 34129, Republic of Korea khlee@kier.re.kr		5th September 2024

DEDICATION

To my beloved family for their endless love, encouragement, and sacrifices. You have been my pillars of strength, shaping me into who I am today. This achievement is as much yours as it is mine.

ACKNOWLEDGEMENT

I extend my deepest gratitude to my esteemed supervisors, Prof. Julius Mwakondo Mwabora, Prof. Julius Maima Ogola, and Dr. Kyoung-ho Lee, for their unwavering guidance, support, and invaluable insights throughout my Ph.D. journey. Your mentorship has been instrumental in shaping both my academic and personal growth.

I am profoundly grateful to the Partnership for Skills in Applied Sciences Engineering and Technology – Regional Scholarship and Innovation Fund (PASET-RSIF) for their generous funding, which made this research possible. Your investment in education and research makes a tangible difference in advancing knowledge and innovation in our region.

I must also thank the other team members at the Renewable System Laboratory at the Korea Institute of Energy Research: Dr. Jong-gyu Kim, Dr. Hongjin Joo, Dr. Youngsub An, Wang-je Lee, and Dr. Han Gwangwoo. Their support and work ethics inspired me to accomplish this work.

To my esteemed colleagues at the Department of Physics, University of Nairobi, your camaraderie and intellectual exchange have enriched my academic experience and fostered a stimulating research environment. Special appreciation goes to my wonderful friends, particularly Dr. Egbo Munonyedi Kelvin, whose unwavering support and willingness to engage in discussions have inspired and motivated me. Your encouragement has been invaluable, and I am deeply grateful for your friendship.

Thank you to everyone who has contributed to my academic and personal growth in visible and invisible ways. Your support has been the cornerstone of my success.

ABSTRACT

The adoption of renewable energy, such as solar, to meet the energy demand in buildings has become one of the keys to achieving the global target for net-zero emissions. As a result, solar photovoltaic installations have increased tremendously, giving rise to an enormous redundancy of electricity generation. This has become an issue requiring alternative ways to be addressed. Underground thermal energy storage (UTES) for power-to-heat operations has gained interest in this area due to its reliability, cost-effectiveness, and carbon-free nature. However, UTES systems face challenges of thermal losses requiring improvement through thermal insulation of the storage volumes. This solution is yet to be applied in developing and evaluating inverse-grey-box (IGB) models for application in water heating and building space conditioning. The goal of this study was to model and simulate a solar-assisted dual-source heat pump system combined with UTES for application in water heating, space heating, and space cooling.

This study conducted an experimental investigation of vertical and horizontal configurations of UTES with insulation on the top and sides of its storage volumes. A detailed transient system (TRNSYS) model representing the actual experimental set-up was developed, in addition to a 4 resistance, 2 capacitance (4R2C) IGB model, which was developed using thermal network analysis. These models were calibrated for application using the measured data from the experiment. Additionally, the data generated from the calibrated TRNSYS model was used to re-calibrate the IGB model and evaluate its short- and long-term performance. Furthermore, an original system configuration with an operational strategy guided by simple control algorithms integrating the calibrated UTES model for inter-seasonal consumption of surplus solar energy in a public-school building was also developed and evaluated using four distinct study cases. Case 1 involves an air-source air-load (ASAL) with UTES for power-to-heat and cool (P2HC) operation, Case 2 and Case 3 involve an air-source water-load (ASWL) heat pump with 1.5m-deep and 150m-deep UTES, respectively, for P2HC operation. Each case was modelled with a corresponding conventional case without UTES for P2HC operation. Case 4 involves a dual-source dual-load heat pump with a conventional ASAL heat pump without UTES for P2HC operation as the base case.

The results of the TRNSYS and IGB model calibration showed that the TRNSYS model agreed with the measured data, predicting the output water temperature with a coefficient of variation of root mean square error (CVRMSE) of 3.16% and 2.97% for the vertical and horizontal

configurations, respectively. Similarly, the IGB model agreed with the measured data with CVRMSE of 7.91% and 3.17% for vertical and horizontal types, respectively. Moreover, sensitivity analysis on the IGB model showed that the longer the training duration, the higher the performance was, with a convergence point of 20 weeks. These results indicate that the models are well-calibrated and validated for application.

The evaluation of the developed system configuration and control strategy improved the performance of the incorporated heat pumps in different case studies. A P2HC efficiency, energy savings, and UTES thermal efficiency of 16%, 18%, and 22%, respectively, were obtained for Case 1, while 26%, 16%, and 34%, respectively, were obtained for Case 2. In Case 3, 22%, 13%, and 28% were obtained, similar to 28%, 20%, and 91% obtained for Case 4. In each case, above 70% self-consumption ratio (SCR) and 21% surplus energy utilisation ratio (SEUR) were obtained, except for Case 1, where 73% SCR and 34% SEUR were obtained.

The parametric analysis in Case 2 examined how changes in UTES size, solar PV capacity, and power-to-cool/heat durations affect system performance. Larger UTES size and increased solar PV capacity generally decreased thermal and P2HC efficiency, with slight energy savings improvements. Adjusting P2C and P2H durations enhanced efficiency while maintaining energy savings. An economic analysis showed promising results with a levelized cost of heat at $0.45/kWh.

The results signify that simplified IGB models, particularly useful when model parameters are unknown and require plenty of resources to be determined, were developed and well-calibrated with data from actual field experiments. These models can be applied in heating and cooling systems using heat pumps to reduce energy consumption and consequent climate change. This is a crucial path to carbon neutrality. The system configuration and its control method can be applied anywhere in the globe for commercial and residential buildings by modifying the control technique to accommodate periods of surplus energy. This solves the problem associated with integrating surplus energy into the grid and the energy wastes from solar energy systems in countries where policies that allow for feed-in-tariff (FiT) and net-metering are yet to be implemented. The study recommends detailed techno-economic analysis for commercial and domestic applications, as well as exploring different thermal network models to optimise system performance.

TABLE OF CONTENTS

LIST OF TABLES

LIST OF FIGURES

LIST OF ABBREVIATIONS

Symbols	Description (unit)
A_f	Heat transfer surface of the pipe (m^2)
A_f	Area of collector
C_g	Volumetric heat capacitance of the grouting material (kJ/K)
c_{pw}	Specific heat capacity of water (kJ/kg·K)
h_f	Fluid convective heat transfer coefficient (kJ/hr·m^2·K)
N	Number of boreholes
$\dot{m}_w$	Mass flow rate of working fluid (kg/hr)
$\dot{Q}_w$	Heat transfer rate (kJ/hr)
T_g	Temperature at the grouting node (°C)
T_G	The effective temperature of far-field soil outside the insulation (°C)
T_{soil}	The soil (ground) temperature of the borehole storage volume (°C)
$\bar{T}_w$	Average water temperature (°C)
T_{in}	Inlet water temperature to the borehole (°C)
T_{out}	Outlet water temperature from the borehole (°C)
Soil	
Thermal Resistances	
C_{soil}	Thermal capacitance of soil (kJ/K)
R_{as}	Ambient to soil thermal resistance (K·hr/kJ)
R_{gs}	Grout to soil thermal resistance (K·hr/kJ)
R_{sG}	Thermal resistance between T_G and the T_{soil} (K·hr/kJ)
R_{wg}	Water to grout thermal resistance (K·hr/kJ)
V_s	Volume of the borehole (m^3)
c_{ps}	Specific heat capacity of soil (kJ/kg·K)
ρ_s	Density of the soil (kg/m^3)
Pipe	
L	The effective length of the borehole pipe (m)
r_b	Borehole Radius (m)
r_{p1}	Inner radius of the pipe (m)
r_{p2}	The outer radius of the pipe (m)

Other borehole parameters

$\dot{Q}_{cool/heat}$	Cooling or heating rate (kW)
$h_{\_air}$	Convective heat transfer coefficient of air (kJ/hr· m²·K)
$A_{ins,G}$	Area of side (vertical) insulation to far-field (m²)
$A_{ins,s}$	Soil area below top insulation slab (m²)
A_{ins}	Area of insulation slab (m²)
$A_{s,ins}$	Area of soil to side (vertical) insulation (m²)
A_s	Surface area of borehole (m²)
$A_{surf,ins}$	Soil area above top insulation slab (m²)
C	The zone capacitance (kJ/K)
c_p	Specific heat capacity (kJ/kg·K)
c_{pg}	Heat capacity of the grouting material (kJ/kg·K)
c_{ps}	Heat capacity of soil (kJ/m³/K)
E_{conv}	power consumption of the conventional heat pump (kW)
E_{test}	power consumption of the test heat pump (kW)
E_{HP}	Power consumption of the heat pump (kWh)
E_{com}	Power consumption of heat pump compressor (kW)
E_{fan}	Power consumption of heat pump fan (kW)
E_{p2hc}	Power consumption of heat pump during UTES charging (kW)
$E_{pv,surplus}$	Surplus PV power generation per given time (kWh)
$E_{pv,total}$	Total PV power generation per given time (kWh)
$E_{pv,HnC}$	Total PV power consumed during winter heating and summer cooling (kWh)
$E_{pv,P2HC}$	Total annual PV Power consumed by heat pump for P2HC operation (kWh)
$E_{pv,etc}$	Total PV power used for other electricity demands of the building including lighting and water pumps (kWh).
$E_{pv,used}$	Total PV power consumed per given time (kWh)
$FhoS1$	Flow meter for measuring the flow from the storage tank (horizontal)
$FhraR1$	Flow meter for measuring the fluid flow from the radiator (horizontal)
$FhraR2$	Flow meter for measuring the fluid flow from the radiator (vertical)
$FhvS2$	Flow meter for measuring the flow from the storage tank (vertical)
h	Heat transfer coefficient
k	Thermal conductivity

k_{grout}	Thermal conductivity of grout material (kJ/hr·m·K)
k_{ins}	Thermal conductivity of insulating material (kJ/hr·m·K)
k_p	Thermal conductivity of pipe (kJ/hr·m·K)
k_s	Thermal conductivity of soil (kJ/hr·m·K)
l_b	Effective length of the heat conduction path (m)
$L_{ins,G}$	Distance from side insulation slab to far-field (m)
$L_{ins,s}$	Distance below the top insulation slab (m)
L_{ins}	Insulation thickness (m)
$L_{s,ins}$	Distance from soil to side insulation slab (m)
$L_{surf,ins}$	Distance above the top insulation slab (m)
$\dot{m}$	Mass flow rate (kg/hr)
Q	Heat gain/loss (kW)
$Q_{BT2load}$	Heat transfer to load from the buffer tank (the met load in kWh)
$Q_{HP2water}$	Heat transfer to the liquid on the heat pump load side (kWh)
Q_{Load}	Building load (kWh)
$Q_{UTES,c-d}$	Fluid-to-ground heat transfer from heat pump to UTES during charging in spring and autumn and during discharging in winter and summer (kWh)
r_g	Radius of grout (m)
t	Time (hour)
TH_C_i	Temperature sensor on the center side of the storage volume (horizontal)
TH_E_i	Temperature sensor on the east side of the storage volume (horizontal)
TH_N_i	Temperature sensor on the north side of the storage volume (horizontal)
TH_S_i	Temperature sensor on the south side of the storage volume (horizontal)
TH_W_i	Temperature sensor on the west side of the storage volume (horizontal)
TH_o_i	Temperature sensor outside the insulation of the storage volume (horizontal)
$ThoR1$	Return the temperature sensor to the storage tank for horizontal
$ThoS1$	Supply temperature sensor from the storage tank for horizontal
$ThraR1$	Temperature sensor for measuring the return fluid temperature from the radiator (vertical)
$ThraS1$	Temperature sensor for measuring the supply fluid temperature from the radiator (horizontal)
TV_C_i	Temperature sensor on the center side of the storage volume (vertical)
TV_E_i	Temperature sensor on the east side of the storage volume (vertical)

$TveR2$	Return the temperature sensor to the storage tank for vertical
$TveS2$	Supply temperature sensor from the storage tank for vertical
$TvraR2$	Temperature sensor for measuring the return fluid temperature from the radiator (vertical)
$TvraS2$	Temperature sensor for measuring the supply fluid temperature from the radiator (vertical)
TV_N_i	Temperature sensor on the north side of the storage volume (vertical)
TV_S_i	Temperature sensor on the south side of the storage volume (vertical)
TV_W_i	Temperature sensor on the west side of the storage volume (vertical)
TV_o_i	Temperature sensor outside the insulation of the storage volume (vertical)
$T_{ambient}$	The ambient temperature (°C)
T_{in}	Inlet water temperature (°C)
T_{inf}	Temperature of infiltrating air (°C)
T_{out}	Outlet water temperature (°C)
T_z	Temperature of zone (°C)
UA	Product of zone loss coefficient and the zone area (kJ/hr·K)
V	Volume (m^3)
V_g	The volume of the grouting material (m^3)
V_s	Volume of the borehole (m^3)

Greek Symbols

η_{P2HC}	Power-to-heat and cool (P2HC) efficiency
ρ_g	Density of the grouting material (kg/m^3)
α	A dimensionless factor
ρ	Density (kg/m^3)

Subscripts

a	air
c and d	Charge and discharge
hp	Heat pump
i and f	Initial and final
w	water

Abbreviations

4R2C	4 resistance 2 capacitance
7R5C	7 resistance 5 capacitance
AI	Artificial Intelligence
ANN	Artificial Neural Network
ANSYS CFX	Analysis system (Computational fluid dynamics tool)
ASAL	Air-source air-load
ASHP	Air Source Heat Pump
ASHRAE	American Society of Heating, Refrigeration, and Air-Conditioning Engineers
ASWL	Air-source water-load
CFD	Computational Fluid Dynamics
COP	Coefficient of Performance
CVRMSE	Coefficient of Variation of Root Mean Square Error
DHW	Domestic Hot Water
F2G	Fluid-to-ground
FEFLOW	Finite Element subsurface FLOW system
FiT	Feed-in-Tariff
FPC	Flat plate collector
ETC	Evacuated tube collector
PTC	Parabolic trough collector
GenOpt	Generic Optimization Program developed by NREL
GHG	Greenhouse gas
GSHP	Ground-source heat pump
HP	Heat pump
HVAC	Heating, Ventilation, and Air-Conditioning
HX	Heat exchanger
IEA	International energy agency
IGB	Inverse-grey box
LCM	Lumped capacity method
LCoH	Levelized cost of heat ($/kWh)
MATLAB	Matrix laboratory
MBE	Mean bias error

MPC	Model Predictive Control
NREL	National Renewable Energy Laboratory
NRMSE	Normalized Root Mean Square Error
P2C	Power-to-cool
P2H	Power-to-heat
P2G	Power-to-gas
P2HC	Power-to-heat and cool
PCM	Phase Change Material
PSO	Particle Swarm Optimization
PV	Photovoltaic
PVSC	Photovoltaic self-consumption
PVSS	Photovoltaic self-sufficient
PVT	Photovoltaic Thermal
RE	Renewable energy
RMSE	Root Mean Square Error
SAGSHP	Solar-assisted ground-sourced heat pump
SAHP	Solar-assisted heat pump
SCOP	Seasonal coefficient of performance
SCR	Self-consumption ratio (%)
SE	Solar energy
SEUR	Surplus energy utilization ratio (%)
SSE	Sum of square Errors
sUTES	Shallow Underground Thermal Energy Storage
SWH	Solar water heating
TES	Thermal Energy Storage
TRNSYS	Transient System Simulation Program
TRRA	Trust-reflective algorithm
UTES	Underground Thermal Energy Storage
WWHP	Water-to-water heat pump

CHAPTER 1: INTRODUCTION

1.1 Background of the Study

The relationship between fossil fuel utilization and climate change, along with other major environmental challenges, has become obvious recently, and many scientists and researchers have carried out several studies to address the issue. Variable energy prices, the exponential growth of the world's populace, and the economic prosperity of developing countries all contribute to the steady rise in energy demand (IEA, 2022). Due to the low energy access rate, especially in sub-Saharan Africa, energy prices tend to fluctuate. In Sub-Saharan Africa (SSA), the population without access to electrical energy decreased from 980 million in 2017 to 860 million in 2018, with around 600 million people still living without power in 2019 (IEA, 2019). The global population is currently around 7.7 billion people, with forecasts of 9.7 billion by 2050 and a total peak projection of 11 billion by the end of the 21st century. Asia and SSA are driving this exponential growth, with the SSA population expected to expand by 50% by 2050 (United Nations, 2019). According to the current policy scenario, global energy consumption will increase by 1.3 percent until 2040 if no energy policy changes and efficiency improvements are made. (IEA, 2019).

Another factor is the concern over the fast depletion of fossil fuels and the urgent need to alleviate the effect of climate change. The stated policies scenario of the IEA indicated that in 2018, the carbon dioxide emission related to energy increased by 1.9% and is projected to reach approximately 36 gigatonnes by the end of 2050 (IEA, 2019). The major challenge for all scientists and researchers remains how to satisfy the rising demand for energy while alleviating the effects of climate change in accordance with the Paris Accord to limit the global increase in temperature below 2^{o}C, preferably 1.5^{o}C. To accomplish the target of the Paris Accord, the emissions relating to energy production and consumption need to decrease to zero by 2050 (IEA, 2019).

The remedy to the electrical energy conundrum has been identified in the last decade as the application of energy conservation and energy efficiency strategies and actions, and the adoption of renewable energy (RE) as alternative energy solutions (Adenle, 2019). Renewable energy is energy that is replenished by a natural process at the same rate or faster than the rate at which they are consumed (Eze et al., 2022). Various sources of renewable energy include

solar, wind, biomass, and ocean tides, among others. Solar energy, derived from the sun, has been harnessed through technologies such as solar photovoltaic (PV) and solar photovoltaic thermal (PVT). These advancements have greatly benefited the global economy by providing electricity demand and heating needs to areas without access to the national grid or where it is either expensive or unreliable (Babatunde et al., 2022). However, there remains a challenge in fully utilizing the potential of solar energy across the globe, particularly with solar PV and solar PVT technologies, due to inadequate reliable, carbon-free, and inexpensive storage (Deguenon et al., 2023; Herrando et al., 2021; Li et al., 2023 and Rashmi et al., 2021). Researchers have attempted to address these issues through various means, such as combining solar energy with water heating, solar drying, solar cooking, and solar heating and cooling systems as decribed in the following section.

1.1.1 Solar Energy Applications

Solar water heating (SWH) has made significant progress in water heating operations, thanks to the growth of solar energy (SE). This notion entails using SE as a source of energy to heat water for residential or industrial use. In this system, SE is collected through the solar collector and transformed to heat by forcing or allowing water to circulate through the system (Shoeibi et al., 2022; Tahiri et al., 2023; Vengadesan and Senthil, 2020). The hot water is then kept in a storage tank until it is needed again. A typical implementation of this technology is depicted in Figure 1.1. The system has been developed and advanced by employing several techniques for its component designs. Research into the development of its energy storage capacities, water flow management, and system economic reduction were all explained explicitly (Mane and Kale, 2021; Nwaji et al., 2019; Pandey et al., 2021).

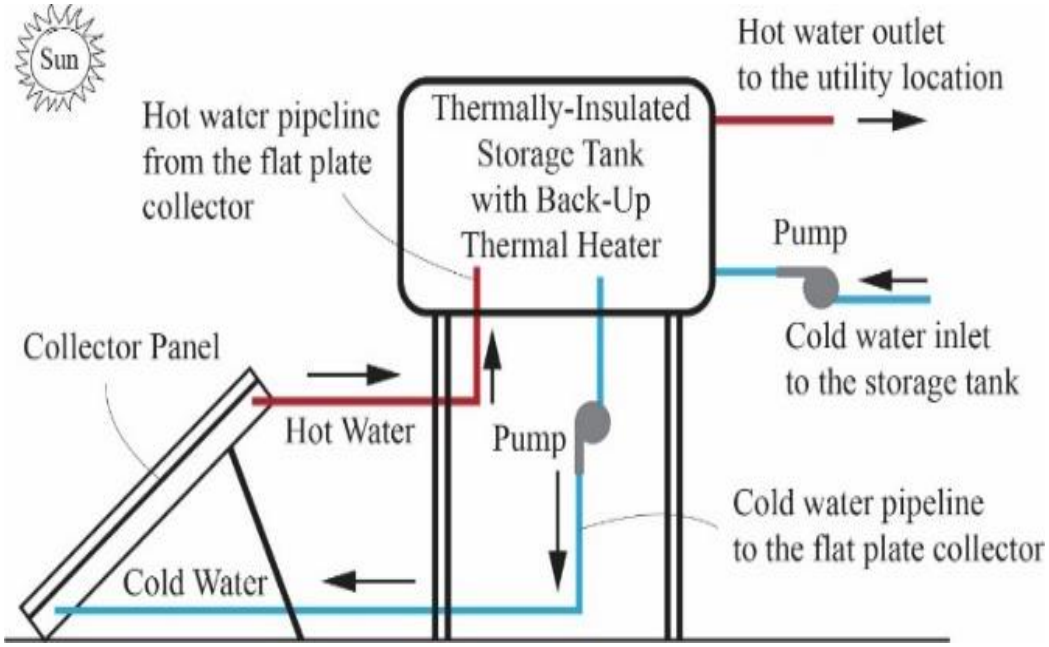

Figure 1.1: Solar water heating Technology *(Eze et al., 2024)*

Solar energy applications have also gained interest in drying technologies, where it is applied with other components, such as air heaters and blowers for drying agricultural products (Mohana et al., 2020). The technology uses either forced convection heat or natural convection heat transfer process for the drying of products in an attempt to their conservations for easy processes. A typical solar drying system is shown in Figure 1.2. The general working principle is such that the air's relative humidity is decreased in the collector chamber before being carried to the drying chamber, where it picks up the product's moisture content and discharges it through the chimney.

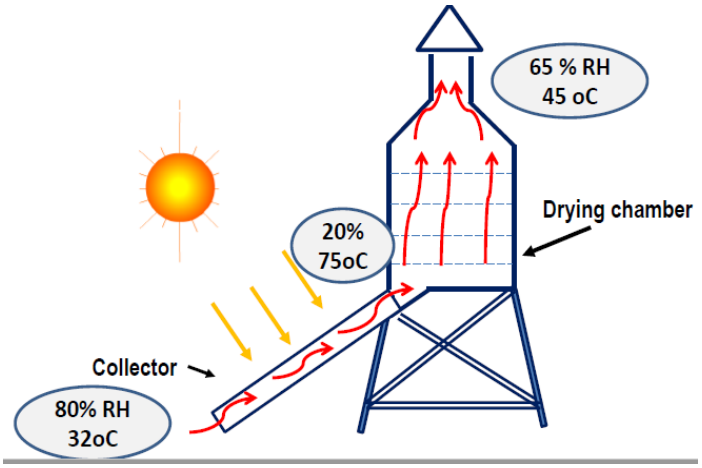

Figure 1.2: Solar Drying Technology (Ramde, (2017))

The applications of solar energy in thermal processes extended to solar cooking technologies ranging from its designs to the establishment of their cost-effectiveness (Arunachala and Kundapur, 2020). Solar energy is captured by the solar collector in the application of solar energy for cooking, as shown in Figure 1.3. The absorbed solar radiation is channeled to a well-insulated cooking chamber either naturally or with the help of a mechanical blower. The heat is finally transferred to the cooking pot for cooking food. Overwhelming interests have been developed in this technology; hence, it currently possesses different designs, although their commercialization has been limited, according to research by Ebersviller and Jetter, (2020).

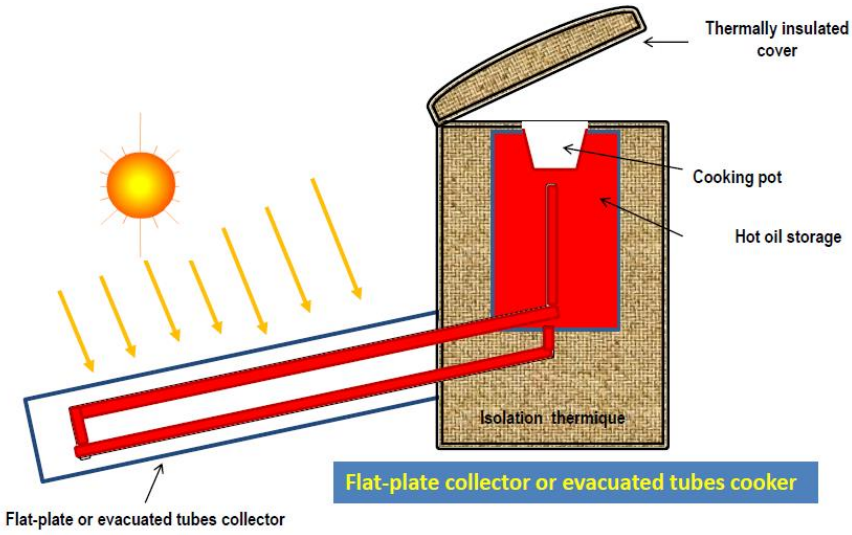

Figure 1.3: Solar Cooking Technology (Ramde, (2017))

In cooling applications, solar energy has also been used to minimize energy consumption and greenhouse gas (GHG) emissions in two applications – solar PV cooling systems and solar thermal cooling systems (Duffie et al., 2020). Energy consumption relating to heating and cooling is rising, and matching their demand with conventional energy sources leads to high GHG emissions in the atmosphere. This issue has led to the development of solar cooling systems in recent years in the form of vapour compression systems, Peltier effect systems, Stirling solar systems, and heat-driven systems such as the vapour absorption cycle systems. An evaluation of the evolution and state-of-the-art solar cooling technologies was conducted by Alahmer and Ajib, (2020).

1.1.2 Hybrid HVAC Systems

The integration of solar energy systems with heating and cooling systems, such as heat pumps, has garnered significant attention among researchers (Wang et al., 2022). The thermodynamic process of space heating or cooling entails regulating the temperature and humidity of a building's interior to ensure optimal comfort for occupants. Solar PVT technology, when combined with heat pumps and TES tanks, has proven effective in achieving this (Belmonte et al., 2022; Bordignon et al., 2022). Figure 1.4 depicts a possible configuration of a SE system, a TES unit, and a HP for space conditioning. The combination of these components is more efficient and carbon-free for heating and cooling purposes. This is because the coupled heat pump is aided by the solar PVT system, and the TES helps in maintaining the thermal balance during heating and cooling operations (Gaonwe et al., 2022; Miglioli et al., 2023). This type of heat pump operation is called the solar-assisted heat pump. By combining the heat supply from the TES with other fluid sources, such as air on the source-side or on the load-side of the heat pump, a dual-source or dual-load heat pump can be achieved. In Figure 1.4 the concept on the study of space conditioning using solar energy to assist a heat pump along with a conventional TES system is shown. Heat energy is generated and transported through water, which is stored in a well-insulated storage tank and pumped to the heat pump when needed to be discharged into the space (house) for conditioning. This method has proven reliable and efficient. However, heat retention in the storage tank has been a challenge due to the time variation of the energy source. Therefore, the exploration of a more sophisticated heat storage system is worth doing. The PVT can be replaced with PV, and in the application of seasonal thermal storage, surplus electricity from either can be used to charge the TES during mild weather conditions when little or no heating or cooling is needed. This is the concept that the present work explores.

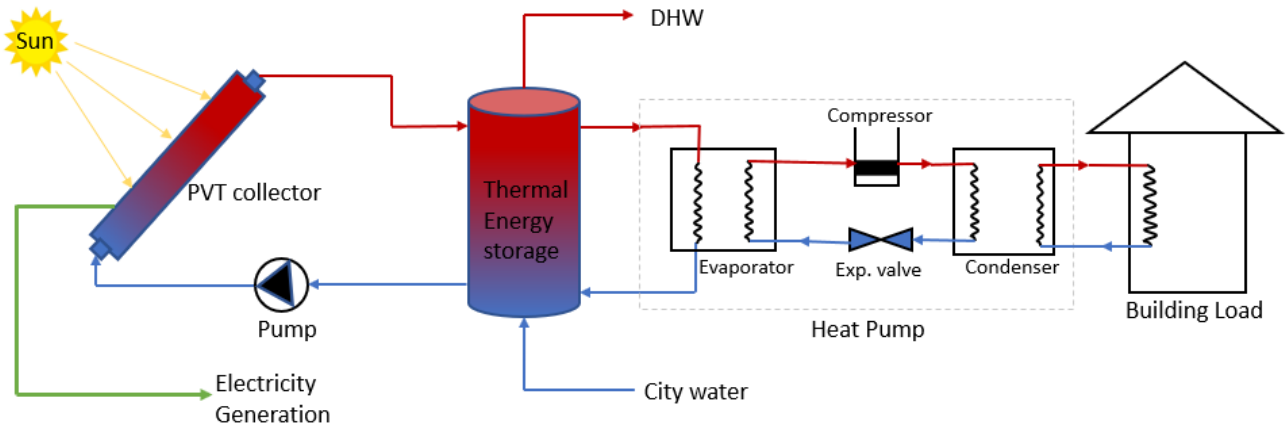

Figure 1.4: Solar assisted heat pump for space conditioning application

1.1.3 Challenges in the application of solar energy

Globally, solar PV is becoming cheap, and several countries are rolling out policies that mandate institutions, or simply commercial buildings, to meet a percentage of their energy requirements with renewable energy. Due to this, many commercial energy consumers resort to the installation of large-capacity of PV, and consequently, energy redundancy exists at different seasons of the year when energy demand is low. Integrating this energy into the grid causes voltage and frequency instability, as well as high demand ramping rates (Hossain et al., 2023; Jha and Shaik, 2023; Salah, 2022; Shafiullah et al., 2022). Another option is the use of Lithium-ion batteries for storing this excess energy however, they are expensive and possess a short lifespan (Aranzabal et al., 2023; B. Li et al., 2023; Okay et al., 2022). As a result, P2H and power-to-gas (P2G) strategies have become the recent trend in storing this excess power since other thermal energy storage strategies such as conventional TES using insulated tanks, phase change material (PCM), and vacuum insulated tanks are expensive (Vaziri et al., 2023). Moreover, when P2H or P2G are employed, optimized system configuration and operational control that enables the system to operate self-sufficiently throughout the season is a need that has posed a challenge, resulting in decreased system efficiency (Calise et al., 2023; Fambri et al., 2023). Previous studies have focused more on the daily consumption of energy from an installed solar energy system rather than seasonally, as demonstrated in Figure 1.5. Therefore, by accomplishing this, the system may be able to operate inter-seasonally and adequately utilize the existing excess energy from the solar energy solar energy systems. To accomplish

P2H as a method of solving this issue, the use of thermal energy storage, particularly the UTES for storing this surplus electricity in the ground in form of heat for a later use is required. However, UTES still face challenges related to significant thermal energy loss from the top and sides of their storage volumes, necessitating improvements. Additionally, simplified but reliable models for UTES are difficult to come by. So far, there is no developed UTES model with insulation. Hence, it is necessary to develop a simplified or detailed inverse model with thermal insulation around the storage volume that can be applied to simulating the behavior of the system when integrated with a heat pump assisted with a solar energy system. Previous studies on UTES have shown that they are cost-effective and reliable for storing and releasing thermal energy in building applications. However, their application in space heating and cooling is limited. Therefore, this research focused on developing and calibrating inverse models of UTES and, through modeling and simulation, combines it with solar energy systems and heat pumps for building space conditioning. The aim is to develop an optimal system looping configuration and investigate the use of UTES to bridge the gap in the existing energy redundancies in the application of time-dependent solar energy.

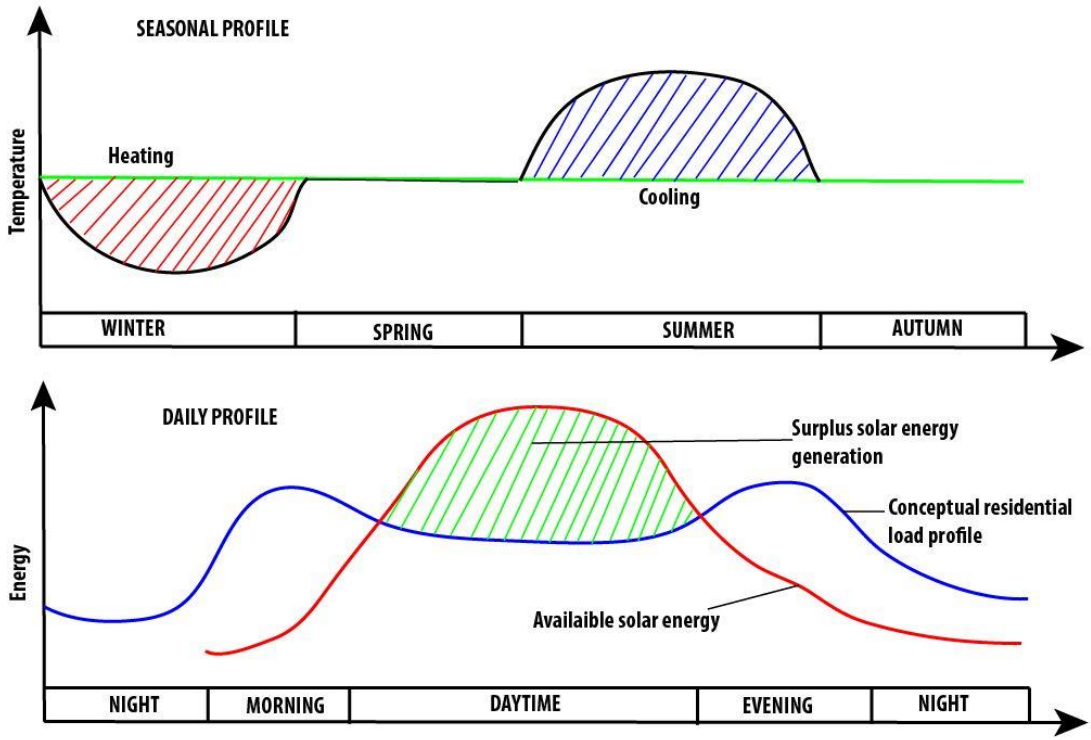

Figure 1.5: Available solar energy in comparison with the daily energy demand of residential homes showing excess energy (Modified from *(Fleischer, 2015)*)

1.2 Statement of the Problem

Recent studies have shown that combining solar PV and PVT systems with heat pumps can provide energy-efficient heating and cooling solutions, reducing energy consumption and greenhouse gas emissions. However, these systems face challenges in energy storage and optimization. Additionally, there is a lack of sophisticated system configuration with an operational strategy guided by simple or advanced control methods for optimum performance, necessitating further research. As solar PV becomes more affordable and policies of various countries mandate increased use of renewable energy, many commercial consumers are installing large-capacity PV systems. This often leads to energy surpluses during low-demand periods, which can cause grid instability when fed back into the national electricity grid. While Lithium-ion batteries offer one storage solution, they are expensive and have short lifespans. Consequently, power-to-heat (P2H) and power-to-gas (P2G) strategies have emerged as cost-effective alternatives for storing excess energy. UTES is a promising P2H method, but it still faces challenges with thermal losses and lacks reliable models, especially those incorporating insulation. This research addresses these issues by developing and calibrating inverse UTES models and integrating them with solar systems and heat pumps for optimal building space conditioning. The goal is to create an efficient system configuration that can operate year-round, effectively utilizing excess energy from solar systems and bridging the gap in seasonal energy redundancies. By focusing on these aspects, the study seeks to expand the application of UTES in space heating and cooling, contributing to more sustainable and efficient building energy systems.

1.3 Objectives of the Study

1.3.1 Main Objective

The primary goal of this study is to model and simulate a solar-assisted dual-source heat pump system combined with a ground thermal energy storage (UTES) for application in water heating, space heating, and space cooling.

1.3.2 Specific Objectives

I. To perform experimental investigation of underground thermal energy storage systems
II. To develop and calibrate inverse models for underground thermal energy storage systems.

III. To develop a simulation model of the entire system configuration employing adequate control algorithms.
IV. To perform comparative evaluation on different heat pump case scenarios for application
V. To perform a parametric study of the system for optimum performance evaluation.

1.4 Justification of the Study

The global energy use is heavily reliant on buildings, with about 40% of the energy consumed in this sector. Within that percentage, space cooling and heating in buildings contribute to approximately 60% of the energy demand. Projections indicate that by 2050, heating and cooling needs will account for around 84% of total energy consumption in residential buildings (IEA, 2023). Unfortunately, the predominant method of meeting this demand involves the use of fossil fuels, which not only contributes to climate change but also releases harmful gases. To address these challenges and promote cleaner energy to achieve carbon neutrality, solar power has emerged as a sustainable solution. However, the widespread adoption and efficient use of solar energy face obstacles, such as the lack of affordable and reliable energy storage systems and difficulties in configuring systems for optimal performance. Consequently, a significant amount of energy generated by solar energy technologies is wasted, particularly in developing countries, where relevant policies like feed-in tariff (FiT) and net-metering are lacking. Although these policies and technologies are already in place in developed countries like Europe and America (Ndiritu and Engola, 2020), only 13 countries in Africa have adopted them however, implementation poses a challenge (Kazimierczuk, 2019). In developed countries where they are fully implemented, the challenge of voltage and frequency instabilities when integrated into the grid and the expensive nature of other storage methods, such as Lithium-ion batteries, are disturbing challenges. These issues necessitate the exploitation of more affordable and carbon-free energy storage, such as shallow UTES, through implementing P2H and P2C strategies to utilize the excess electricity from solar energy systems for inter-seasonal operation. This will not only reduce energy consumption and save money, but will help in accomplishing net-zero use of energy in the future upon successful deployment.

1.5 Significance of the Study

This study addresses critical issues in the realm of energy efficiency and sustainability. It centers on the combination of solar energy systems with heat pumps, offering a promising

avenue for more energy-efficient heating and cooling applications. This approach not only has the potential to reduce energy consumption but also contributes significantly to the reduction of greenhouse gas emissions. Additionally, one of the primary challenges in the utilization of solar energy is the issue of energy storage. Solar energy availability is time-dependent, and traditional solutions like lithium-ion batteries are not always cost-effective and have a limited lifespan. To overcome these limitations, the study emphasizes the use of underground thermal energy storage (UTES) as a viable alternative. By storing surplus electricity in the form of heat, UTES can significantly reduce energy waste and grid instability, as well as save money. However, the study recognizes that UTES systems are not without their challenges, particularly in terms of thermal energy loss from storage volumes, which needs improvement, which is addressed in this study.

Furthermore, the research acknowledges the seasonal and daily variations in energy demand, particularly in the context of heating and cooling applications. This study aims to balance energy production and consumption more effectively by optimizing system configurations and employing advanced control strategies. This optimization can minimize redundancies and enhance overall system efficiency, a crucial aspect of sustainable energy solutions. Finally, the study's focus on expanding the application of UTES is of paramount importance. While UTES has proven cost-effective and reliable in certain building applications, its utilization in space heating and cooling remains limited. By developing and calibrating inverse models and integrating them with solar PVT and heat pumps, the research strives to broaden the scope of UTES applications. This expansion may open new doors for sustainable energy solutions in various sectors beyond traditional building applications.

In summary, this research contributes significantly to the real-life and academic discourse on sustainable energy systems by addressing energy storage challenges, reducing energy waste, optimizing system configurations, and expanding the application of UTES. Its findings and insights have the potential to pave the way for more efficient and environmentally friendly heating and cooling solutions, with broader implications for the adoption of renewable energy in diverse contexts. The study's outcome will address energy wastage and redundancies in solar energy systems and shall be most relevant in developing countries, where policies and frameworks like feed-in-tariff (FiT) and net-metering are absent or not effectively implement.

1.6 Scope of the Study

The scope of this study focuses on integrating solar PV/PVT systems with heat pumps and underground thermal energy storage (UTES) for commercial buildings. It addresses the challenges of seasonal energy surpluses from large-capacity solar installations and explores efficient storage solutions beyond conventional methods. The research aims to develop and calibrate inverse models of UTES with thermal insulation, optimizing system configurations and operational strategies for year-round efficiency. By taking a seasonal approach, the study seeks to bridge the gap in energy redundancies and expand UTES applications in space heating and cooling. The ultimate goal is to create an optimal system that effectively utilizes excess solar energy, enhances building energy management, and contributes to more sustainable practices in commercial building operations.

CHAPTER 2: LITERATURE REVIEW

2.1 Thermal Energy Storage

Energy storage with the use of batteries suffers many demerits, including their high initial capital costs, limited energy density, short lifespan, safety, and environmental concerns (Dehghani-Sanij et al., 2019; Olabi et al., 2022; Rana et al., 2022). These issues are necessitating the growing interest in thermal energy storage (TES) systems. TES is an important technology that permits the storage of energy in the form of heat for later use, consequently bridging the gap between energy production and use. The common types of thermal energy storage systems include the use of conventional insulated tanks, vacuum insulated tanks, phase change materials (PCM), and underground thermal energy storage (UTES) (Eze et al., 2024b). The thermal energy stored using any of these methods can be applied directly or indirectly in domestic or commercial buildings for water heating and building space conditioning through the application of heat pumps (Zou et al., 2023). Among the types of TES, UTES proves to be the best option in terms of reliability and cost-effectiveness, with the potential to help in the achievement of the 2050 global net-zero emission target (Brown et al., 2024). The operation of UTES involves a two-step process: charging, which refers to the injection of thermal energy into the ground through a working fluid, typically when there is an excess of energy available depending on the intended use, and discharging, which involves the extraction of thermal energy for the purposes of water heating, space heating, or space cooling when required (Eze et al., 2024b). The ground maintains a relatively stable temperature at certain depths throughout the season, which creates a thermal balance (Pan et al., 2020). This characteristic makes the ground-source heat pump (GSHP) more efficient than the conventional air-source heat pump (ASHP). However, as the depth of the UTES increases, so does the cost of the system. Therefore, it is worth considering the shallow type of UTES as a more cost-effective alternative (Kim et al., 2021).

2.1.1 Types of Underground Thermal Energy Storage

Underground thermal energy storage is classified into two major types- horizontal and vertical types. However, other sub-categories, such as the slinky and pond-loop types, exist, as shown in Figure 2.1. In practice, horizontal and vertical types have been used extensively (Başer and McCartney, 2020; Mahon et al., 2022; Selamat et al., 2016). The vertical types are usually cylindrical in shape and consist of single or multiple U-tube pipes buried within the grouting

material. On the other hand, the horizontal types are buried horizontally in layers within the soil. The ground properties, working fluid properties, storage volume, length of pipes, depth, and borehole spacing are majorly the driving parameters of the UTES (Kupiec et al., 2015; Lamarche, 2019). The size of the systems is dependent on the application, either for commercial purposes or for residential applications. The deep UTES are usually vertically configured and are primarily installed at depths between 10 – 100m (Brown et al., 2023; Mahon et al., 2022; Welsch et al., 2016), as opposed to the shallow UTES, which are basically installed within 1.5m to 10m (Kim and Nam, 2020). The system capacities affects the overall cost requiring the check for the best or optimum capacity in terms of depth (Kim et al., 2021; Oh et al., 2024; Xue et al., 2024 and Yang et al., 2023).

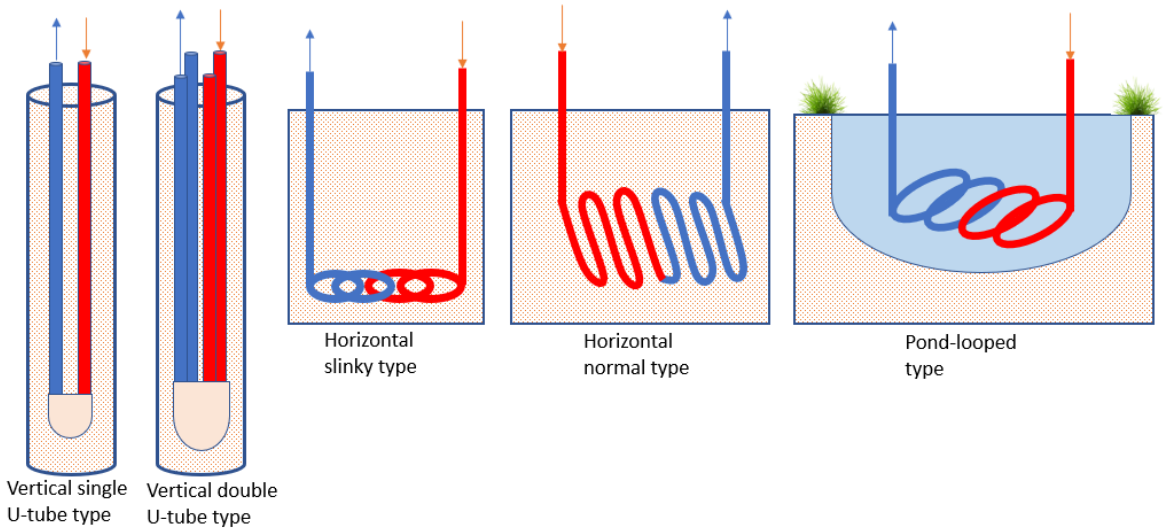

Figure 2.1: Types of Underground Thermal Energy Storage

2.1.2 Application of Underground Thermal Energy Storage

Experimental and numerical applications for the study of UTES have been carried out by many researchers, especially for the purpose of water heating and building space conditioning. The size of the system is dependent on the use and the available capital cost. However, some researchers have tried to prove the advantages of the shallow UTES over the deep-type UTES and vice versa. For example, Kim et al., (2021) considered the cost of installation of conventional vertical UTES and performed an experimental study of a modular ground heat exchanger buried at a depth of 4m. The study found average fluid-to-ground rates of 78.98 W/m and 88.83W/m during heating and cooling seasons with a ground temperature decrease of 1.2 ^{o}C during heat discharge and an increase of 4.4 ^{o}C during the charging period, arguing

that the shallow UTES is more cost-effective than the deep vertical type. Another experiment by Naranjo-Mendoza et al. (2019) explored a solar-assisted GSHP system with shallow boreholes for TES application in homes, featuring 16 boreholes insulated with polyisocyanurate and a polythene cover to prevent water entry. Utilizing a mix of glycol and water, the system included a 3kW heat pump and a 200L water tank. The findings revealed that the system could store energy during summer (18% from geothermal and 82% from solar sources) for winter use, with 54% of energy directly used by the heat pump, 46% stored, and 6% lost as thermal losses. The research conducted by Başer and McCartney, (2020) delved into the performance assessment of a California UTES system, focusing on evaluating its benefits within a vadose zone. Both simulations and experimental outcomes demonstrated a strong alignment, highlighting the significance of considering coupled heat transfer and water flow dynamics in soil borehole TES systems placed within vadose zones. Numerous numerical assessments have also been conducted to evaluate the performance of UTES systems. In a study by Gultekin et al., (2016), the effects of various parameters, such as the spacing of borehole heat exchangers (BHEs), operational duration, and thermal conductivity, were examined concerning the thermal performance of highly interactive boreholes. Their research employed a 2D finite element method and revealed that the thermal energy interaction among boreholes intensifies as the number of boreholes increases. This suggests that increased borehole quantity leads to progressively higher thermal losses over time. Furthermore, Gultekin et al. (2016) reported a reduction in thermal losses as the distance between individual boreholes increased. Additionally, Abualqumboz and Rodley, (2018) conducted numerical modeling of a solar system incorporating UTES. While their study made certain simplifying assumptions, the results from their numerical modeling aligned with other findings present in the existing literature. However, it is worth noting that further validation through experimental approaches is necessary to enhance the robustness of the conclusions drawn.

Previous research indicates that UTES is a viable method for heating and cooling. However, in order to fully understand its principles and ensure optimal performance, it's important to question how it works. In some cases, numerical evaluations may not be enough, and an inverse model may be necessary to predict the ground and fluid thermal behaviors. This will help determine the UTES system's abilities and ensure optimal performance.

2.1.3 Underground Thermal Energy Storage Modeling

Due to variation in weather conditions as well as the thermal properties of the ground across the globe, various parameters affect the accuracy of UTES model. It is a challenge to develop a generalized model that may be used in different localities for predicting the thermal behavior of UTES system. According to the ASHRAE handbook (ASHRAE, 2001), modeling of energy systems involves forward and inverse models. Forward modeling involves the physical description of the system, which is the focus of forward modeling, which is utilized in the creation of HVAC systems. On the other hand, the inverse model pertains to the representation of the system's driving forces through their physical properties and the observation of the system's behavior through the use of collected data (Braun and Chaturvedi, 2002). The inverse model is further classified into white-box, black-box, and grey-box model.

2.1.3.1 The White-Box Model

The white box model relies solely on the system's physical characteristics for predicting and evaluating its performance. This method often utilizes energy simulation software like TRNSYS and EnergyPlus. However, its main drawback is the requirement for many parameters that are either already known or necessitate significant time and resources to determine, making it not very cost-effective. It also needs validation against actual system data. Research by Maestre et al., (2013) and Maestre et al., (2015) falls under this category. Maestre et al., (2013) proposed a simplified one-dimensional R-C model, which was later enhanced to a two-dimensional version in Maestre et al., (2015) to simulate heat transfer in a single U-tube UTES system. These models, validated against a CFD reference model from ANSYS CFX, showed good agreement with the reference, with very low RMSE values for water outlet temperatures. Further, Tu et al., (2017) improved the R-C model for the same system considering freezing ground conditions, validated by field data showing accurate results under specified parameters. Kim and Nam, (2020) developed a model for a low-depth ground heat exchanger using finite element analysis, which showed good alignment with both predictive and numerical models according to ASHRAE's RMSE method, despite some discrepancies attributed to weather and operational conditions in an 8-hour experimental trial.

2.1.3.2 The Black-Box Model

On the contrary, the black box model operates by analyzing the system's input and output data, employing methods such as regression analysis, transfer functions, or artificial neural networks

(ANN) for system description. This approach is effective for predicting a thermal system's future behavior, provided that there is an extensive collection of data over time to accurately represent the system's physics. The success of the black box model hinges on both the quantity and quality of the data collected. For a deeper understanding, Lee et al., (2020) implemented a model predictive control (MPC) utilizing ANN to forecast the long-term performance of a building's energy system coupled with UTES, configuring the model with 64 datasets and allocating 70% for training, 15% for verification, and 15% for testing. In thermal energy storage applications, Ren et al., (2022) demonstrated the efficiency of using ANN to forecast the charge and discharge cycles of Phase Change Material (PCM), which is contingent upon the dependability of the training data. Furthermore, Amarasinghe et al., (2015) explored the use of an ANN-based TES system for the management and control of building operations, considering TES and power availability. The authors utilized ANN with a large range of measured data to forecast building power requirements and utility loads over time, leading to enhanced cost savings and reduced waste.

2.1.3.3 The grey-box model

The grey-box model merges the principles of both white and black box models to forecast and assess systems. It harnesses the power of mathematics, incorporating both key physical parameters and empirical data. By training the mathematical model with observed input-output data, it identifies optimal parameters, enhancing the efficiency of system predictions and evaluations by saving time and costs, speeding up computations, and reducing uncertainties. However, its use in thermal engineering is underexplored. Braun and Chaturvedi, (2002) developed an inverse grey-box model to optimize parameters through learning, enabling nearly precise predictions of building energy loads. This model, which uses a transfer function, requires only a short duration of measured data for training and sets specific bounds for optimization parameters. When tested on a different building in another location, the model demonstrated that brief data periods are adequate for training, accurately forecasting HVAC needs. Liu and Cai, (2021) applied the grey-box approach to model servo direct expansion systems, employing a two-stage training method that prioritizes parameter impacts, and found it to deliver reasonable accuracy with limited data on a variable-speed heat pump. Jeon et al., (2018) utilized the grey-box model to predict building loads and energy demands for an optimal predictive control strategy, developing a 7R5C model with parameters estimated through particle swarm optimization, showing high accuracy in predictions with or without weather

forecasts. The comparative effectiveness of white, black, and grey-box models in system analysis has been recognized, with studies like those by Khan and Khan, (2012) noting the white-box model's suitability for algorithm testing despite its higher demands for expertise and resources. Pintelas et al., (2020) demonstrated a grey-box model's superiority in various fields including education, finance, and health. The outcome of the review by Li et al., (2021) highlighted the robustness of grey-box models in building modeling, especially for thermal energy systems, while recommending their application be extended to diverse systems.

2.2 Modeling and simulation of water heating, space heating, and cooling

Globally, water heating, space heating, and space cooling are the most end-use energy activities in commercial and residential buildings (Yıldız et al., 2023). It has already been mentioned that the application of fossil-fuel-based energy for meeting their requirements is deemed unsustainable proving the fact that more carbon-free heating and cooling should be explored. To accomplish this, researchers have tried the combination of several components such as the solar PVT, UTES, and heat pump. This approach not only addresses the problem of excess energy in solar photovoltaic (PV) and photovoltaic-thermal (PVT) systems but also offers self-sustaining solutions for heating and cooling. Over recent decades, there has been a growing interest in combining flat-plate collectors with vapor-compression heat pumps. According to Buker and Riffat, (2016), Solar Assisted Heat Pumps (SAHPs) can be divided into serial, parallel, and indirect types, with numerous studies demonstrating their enhanced efficiency in various configurations. For instance, Bee et al., (2019) conducted an analysis on a system for heating and cooling spaces that combines a heat pump with solar PV panels across different European locations, discovering that the PV panels' energy was adequate for running the heat pump. The system's self-sufficiency improved with the addition of a 12.5 kWh energy storage. Martínez-Gracia et al., (2022) evaluated the integration of a PV system, a seasonal storage tank, and a water-water heat pump (WWHP) in terms of its energy, environmental, and economic benefits, using DesignBuilder for energy demand forecasts and TRNSYS for simulations. The system configuration for this study is shown in Figure 2.2. The results showed that the system meets 80% of the hot water requirements, offers a payback period of 8.5 years, and could decrease CO2 emissions by 44,200 kg annually.

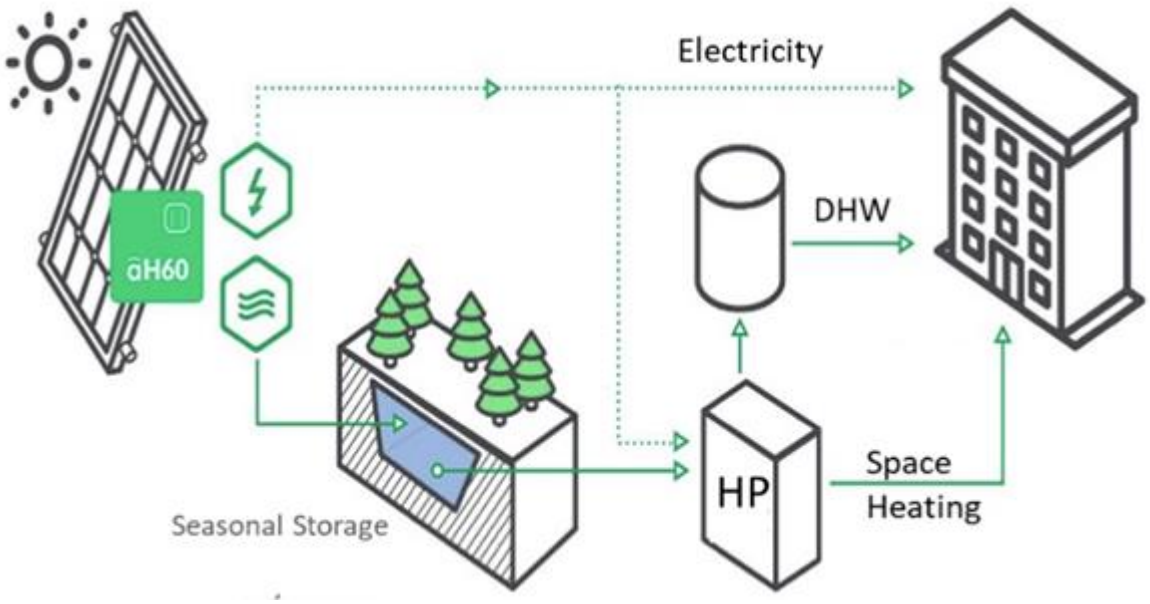

Figure 2.2: A combined solar collector, HP, and TES for space conditioning (Source: Martínez-Gracia et al., 2022)

Ismaeel and Yumrutaş, (2020a, and 2020b) combined Ground Source Heat Pump (GSHP), Photovoltaic Thermal (PVT) system, and Underground Thermal Energy Storage (UTES) to improve performance even for drying purposes. They modified the configuration and conducted a thermal analysis of each system component. Sensitivity analysis for over 10 years showed that the heat pump's coefficient of performance increased continuously for the first 5 years. Similarly, Koşan and Aktaş, (2021) managed to increase the HP efficiency by 15.67% by harnessing the thermal energy released by its condenser with the use of Phase Change Material (PCM) coupled with solar energy. Moreover, Yıldız et al. (2023) employed PCM with a Water-to-Water Heat Pump (WWHP), which improved the heating duration by 30.6%, and achieved a 33.9% COP enhancement, proving the reliability of PCM for temporal heat storage and use.

2.2.1 Modeling and Simulation Tools

Modeling and simulation involve the development of a concise numerical or analytical model that can accurately represent the system under study. In many occasions, the models may be simplified (Cox et al., 2022; Sezen and Gungor, 2022) or detailed (Jakubek et al., 2023). As mentioned in the previous section, such tools as Transient system (TRNSYS), Matrix laboratory (MATLAB), Analysis system (ANSYS), EnergyPlus etc. are tools that extensively used for modeling and simulation of energy system depending on the interest of the study

(Karami and Abdshahi, 2023; Lu et al., 2023; Ma et al., 2023; Wetter et al., 2023). These systems use a detailed mathematical representation of the system they study embedded in complex computer algorithms to calculate various parameters of interest. Their accuracy depends on the knowledge, skills, and expertise of the researcher.

2.3 Control Strategy for Solar-assisted heat pumps

Implementation of the hybrid heating and cooling system has been successful. However, they are still lagging in their configurations and advanced control strategy for inter-seasonal operation. It is necessary to develop a system that can operate self-sufficiently and to accomplish this; adequate control must be employed. Previous studies have attempted to solve this issue. For instance, Naranjo-Mendoza et al., (2019) investigated the combination of shallow UTES at a depth of 1.5m with heat pump and solar PVT system. The result of the study showed that the system could provide adequate energy required during the heating period. However, the authors emphasized the need for an advanced control strategy for more efficient improvement. Similarly, Belmonte et al., (2022) studied SAHP for residential heating purposes in Spain, integrating a PCM as a form of thermal energy storage. The results showed that the operation of PCM could lower the performance of the heat pump without an advanced control strategy. Gaonwe et al., (2022) studied grid-connected heat pumps assisted by solar power, attempting the use of an optimal control scheme. The control algorithm employed was able to improve the cost-effectiveness of the system. Similarly, using the basic fuzzy-logic control method, Hohne, (2023) determined the temperature behavior in solar water heating systems. This method was able to keep in check the water temperature between the upper and lower bounds. Many other researchers, such as in (Youssef et al., 2017; Qu et al., 2020; Zou et al., 2023), have emphasized the need for an advanced control strategy as a way of improving the performance of combined systems for heating and cooling purposes, including the reviews found in (Lin et al., 2022; Zhang et al., 2022; Zhou et al., 2022; Sezen and Gungor, 2023).

2.4 Literature Summary and Research Gaps

Previous studies highlight that underground thermal energy storage (UTES) is a viable solution to the existing energy storage issues by mitigating energy wastes, especially in the application of solar PV and solar PVT systems. In light of this, the shallow UTES may have an advantage over its deep counterparts in terms of cost and reliability, making the shallow UTES the prevailing choice. However, in this application, the thermal losses on the top and sides of the

thermal storage volume are issues that must be addressed to increase the system's thermal efficiency. Additionally, it has been established that for energy systems such as UTES, there are three inverse modeling methods available: white box, black box, and inverse grey box (IGB). Among these, the grey-box model is considered to be the most suitable because it uses a combination of field data obtained over a long or short period of time and a mathematical representation of the system under study. This approach is preferred because measuring the driving parameters of a system or performing an experiment over a long period can require a significant amount of resources. More to this, the grey-box model accurately predicts the long-term performance systems using a short range of training data unlike other AI models such as the ANN. It improves the computational speed and eliminates uncertainties. However, the application is limited to thermal engineering.

Furthermore, a literature review has confirmed that the combination of solar energy systems, UTES, and heat pumps for water heating and building space conditioning improves performance, increases energy savings, and reduces energy consumption and consequent environmental issues. However, determining the optimum configuration for this purpose and applying a suitable and advanced control algorithm for inter-seasonal ground thermal storage and extraction and adequate utilization of the surplus energy generated from solar energy systems remains a big challenge and is currently under-explored. It is possible to convert excess electricity to heat for later use through the application of UTES. This operation is referred to as the power-to-heat and cool (P2HC) technique. Without an excellent control strategy, it has proven difficult to accomplish a self-consumption inter-seasoning operation of space heating and cooling, which is a requirement in both extreme and mild weather conditions. It is important to note that the use of shallow UTES is limited in research and practice when it comes to large and small-scale applications. However, by implementing a heat pump system that is assisted by solar energy and maintaining thermal balance through the use of UTES, it is possible to achieve dual-source and dual-load functionalities (Grossi et al., 2018; Marinelli et al., 2019). This advanced configuration and control strategy paves the way for an efficient and sustainable use of energy.

2.5 Current Research Focus

In this current study, experimental studies of shallow UTES with insulation on the sides for horizontal and vertical configurations were conducted. A similar system was developed in the

TRNSYS simulation tool, and the TRNSYS model was calibrated using the measured data. Additionally, a simplified inverse model for shallow UTES was created using thermal network analysis. This model incorporates the top and side insulations of the UTES systems, as well as the influence of environmental and ground far-field temperatures on the storage boreholes. To evaluate the performance of the developed 4R2C model, it was calibrated through training and testing processes using both measured data and TRNSYS simulation data. MATLAB was utilized for the training and testing, employing a nonlinear optimization method. Further to this, other models from previous studies were reviewed, and their results were compared with the simplified inverse model.

Additionally, a novel system configuration that uses surplus solar energy and an advanced control strategy to power an inter-seasonal heating and cooling system coupled with seasonal thermal energy storage is presented. The system was modeled and simulated in the TRNSYS 18 simulation tool and comprises a single-source, dual-load heat pump, the calibrated shallow UTES, the flat-plate heat exchanger (HEX), and the building load. The proposed system was applied to a school building located in Jincheon, South Korea, for performance evaluation. The energy for operating the heat pump is provided by an independent solar energy installed on the building, which also provides hot water for the building consumption. A conventional system without a Power-to-heat (P2H) configuration was also modeled as a baseline for comparison. This system configuration can be applied to a commercial or residential building in any location of the globe by making a few modifications to the control method to suit the periods when surplus energy from solar energy systems exists.

CHAPTER 3: THEORETICAL FRAMEWORK

3.1 Solar Radiation

When radiant energy from the sun hits the earth's surface or any collector surface, three radiation components are received, which include beam (direct) radiation, diffused radiation, and ground reflected radiation (Duffie and Beckman, 2013). The Sum of these radiations gives the total solar radiation; however, in practical application, measurements are usually done with the total radiation obtainable on a horizontal surface (direct and diffused radiations), usually known as the global radiation. The radiation that is received without the presence of the atmosphere is known as extraterrestrial radiation, G_{on}, and this is given mathematically in Equation (3.1) (Duffie and Beckman, 2013). The value usually varies by approximately $\pm 3.3\%$ due to the change in the earth-sun distance.

$$G_{on} = G_{sc}\left[1 + 0.033cos\frac{360n}{365}\right] \tag{3.1}$$

Where G_{sc} is the solar constant approximated to 1367W/m^2 and $1 \leq n \leq 365$. The rate at which solar radiation strikes a surface is known as solar irradiance, and it is measured in Watt per square meter (W/m^2). The integration of solar irradiance over a time often in hours gives the energy of the sun that strikes a surface per unit area. This is referred to as solar irradiation. Based on the local mean solar irradiance of a location, the electrical and thermal potentials can be established. Since solar energy is location-specific, assessing its potential for a specified location requires consideration of solar time, the sun's position angles, and the number of daylight hours. Solar time (ST) is given in Equation (3.2) (Duffie and Beckman, 2013).

$$ST = T_{standard} + 4(L_{st} - L_{loc}) + E \tag{3.2}$$

Where $T_{standard}$ the standard time and E is known as the equation of time expressed mathematically as:

$$E = 229.2\,(0.000075 + 0.001868cosB - 0.032077sinB - 0.014615cos2B - 0.04089sin2B) \tag{3.3}$$

Where $B = (n-1)\left(\frac{360}{365}\right)$ and$1 \leq n \leq 365$, L_{st} equals standard meridian (longitude) of the native time zone and L_{loc} equals longitude at the specified site. Another important factor to

be defined is the declination angle. The angle made by a line drawn between the earth's center and the sun and the planet's equatorial plane is referred to as the declination angle, δ. and this is expressed in Equation (3.4) (Duffie and Beckman, 2013).

$$\delta = 23.45\, sin\left(360\frac{284+n}{365}\right) \tag{3.4}$$

The declination angle takes care of the seasonal variations in the exploration of the sun's energy for a specified location. On a surface, the incident angle is described as the one formed by the beam energy and the normal to that surface. This is written as:

$$cos\theta = (sin\varphi cos\beta - cos\varphi sin\beta cos\gamma)sin\delta + [sin\beta sin\gamma sin\omega + (cos\varphi cos\beta + sin\varphi sin\beta cos\gamma)cos\omega]cos\delta \tag{3.5}$$

Where β is the slope, φ equals the location's latitude, and γ equals the surface azimuth angle. The hour angle, ω is described as the one via which the planet has alternated from the solar noon and this is given in Equation (3.6) (Duffie and Beckman, 2013).

$$\omega = 15^0 h^{-1}(solar\ time - 12h) \tag{3.6}$$

The number of daylight hours is also important for specified locations, and this is given in equation (3.7) (Duffie and Beckman, 2013).

$$N = \frac{2}{15}cos^{-1}(-tan\varphi tan\delta) \tag{3.7}$$

3.2 Solar Collector

Solar collectors are special types of heat exchangers (HEX) that transform energy from the sun (solar radiation) into heat through working fluids such as air and water (Hohne et al., 2019). They can be differentiated by their modes of design and operation, which include the Flat Plate Collector (FPC), Evacuated tube collector (ETC), and parabolic trough collector (PTC). In heating and cooling, especially space heating using water and air as working fluids, FPC is usually applied. The FPC has essential parts of interest – the solar absorber, which transfers energy to the fluid; the glazed material transparent to solar radiation; and the insulation thickness for thermal heat losses (Toapanta; et al., 2020).

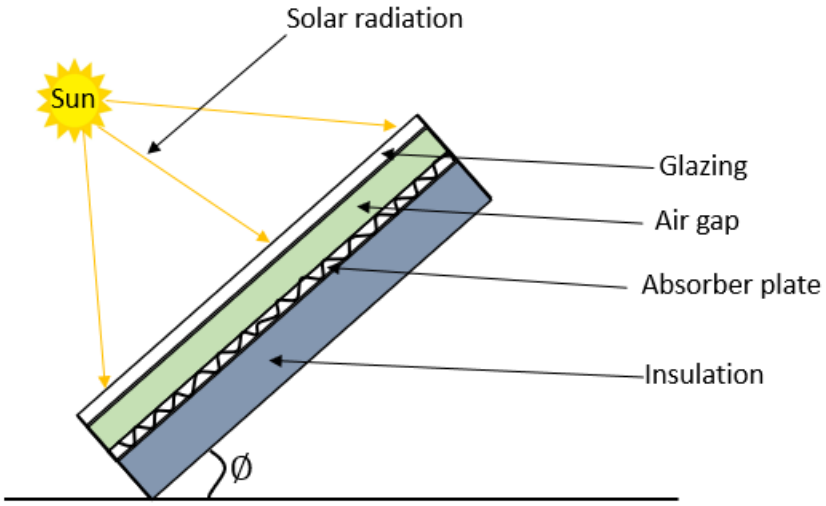

Figure 3.1: Flat plate collector (adapted from Toapanta et al., (2020))

In a FPC as shown in Figure 3.1, the amount of solar energy absorbed per unit area of the absorber by the collector is defined as the variance that exists between the solar irradiation striking the collector and the optical losses. The Energy balance is given in equation (3.8) (Duffie and Beckman, 2013).

$$\dot{Q}_{abs} = \dot{E}_{opt} = \dot{Q}_u + \dot{Q}_{losses} + \dot{Q}_{st} \tag{3.8}$$

Where:

$\dot{Q}_u$ = Useful energy gain

$\dot{Q}_{losses}$ = Total heat losses from the collector

$\dot{Q}_{st}$ = Heat stored by the collector

Each of the above parameters is defined based on their dependable functions and are expressed mathematically in Equations (3.9), (3.10), and (3.11) (Duffie and Beckman, 2013).

$$\dot{Q}_u = \dot{m}_c c_p \left(T_{f,out} - T_{f,in}\right) \tag{3.9}$$

$$\dot{Q}_{losses} = U_{loss} A_c \left(T_{m,abs} - T_{amb}\right) \tag{3.10}$$

$$\dot{Q}_{st} = \left(m_c C_p\right)_{abs} \frac{dT}{dt} \tag{3.11}$$

Where $\dot{m}_c$ equals fluid's mass flow rate, c_p equals fluid specific heat capacity, $T_{f,out}$ and $T_{f,in}$ are exit and supplied fluid temperatures, respectively. U_{loss} is the total heat transfer coefficient of the collector, $T_{m,abs}$ equals the absorber plate mean temperature, and T_{amb} equals surrounding temperature, $(m_c C_p)_{abs}$ equals product of the defined parameters for the absorber while T equals temperature and t equals the operating time. The collector thermal efficiency is given by Equation (3.12) (Duffie and Beckman, 2013).

$$\eta_c = \frac{Q_u}{I_c A_c} = a_0 - a_1 \frac{\Delta T}{I_c} - a_2 \frac{(\Delta T)^2}{I_c} \tag{3.12}$$

Where I_c is incident radiation striking the collector surface and $a_0, a_1, and\ a_2$ are efficiency constants.

3.3 Heat Pump

Heat pumps are devices that use mechanical energy for the movement of heat energy from a "heat source" having a low temperature to a "heat sink" having a high temperature using the principle of the reversed heat engine cycle, as shown in Figure 3.2. The application of a reversed heat engine cycle is found in systems such as refrigerators, air conditioners, and heat pumps. Its aim is to transfer heat energy, Q_L from a cold source having temperature, T_L to a heat sink, having a higher temperature, T_h.

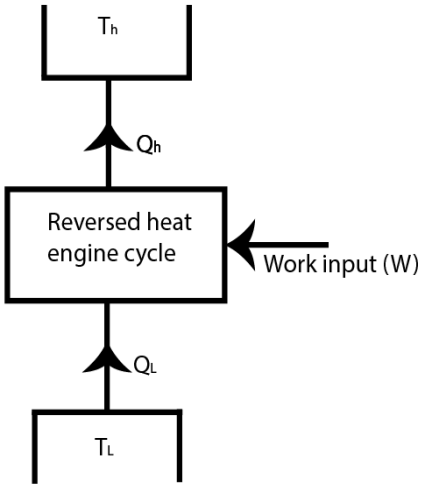

Figure 3.2: Reversed heat engine cycle for heat pump demonstration (adapted from Eastop and McConkey, (2009))

The parameter of interest in this type of system is the work input, W because it is the parameter that has to be paid for and which constitutes the high running cost. For cost reduction and migration of running cost of the systems, solar-energy-driven heat pumps have been developed and have become a topic of great interest for researchers. The relationship between the heat input QL and the rejected heat to the surrounding Qh is given in Equation (3.13) (Eastop and McConkey, 2009).

$$W + Q_L = Q_h \tag{3.13}$$

Where $W = E_{com} + E_{fan}$. The performance of heat pumps and refrigerators are investigated by their Coefficient of performance, $COP_{cool/heat}$ for either heating or cooling as given in Equations (3.14) and (3.15).

$$Q_{cool/heat} = \int_{t_i}^{t_f} \dot{m}_a C_{pa} (T_{in} - T_{out})\, dt \tag{3.14}$$

$$COP_{cool/heat} = \frac{Q_{cool/heat}}{\int_{t_i}^{t_f} (E_{com} + E_{fan}) dt} \tag{3.15}$$

Where $Q_{cool/heat}$ is the cooling or heating load, $\dot{m}_a C_{pa}$ is the product of heat capacity of air and the mass flow rates of air, $T_{in} - T_{out}$ is the temperature difference between the inlet and outlet air temperature, and $E_{com}\ and\ E_{fan}$ are power consumption of the heat pump's compressor and fan, For application to solar heat pumps, the energy balance can be given in Equation (3.16) (Duffie and Beckman, 2013).

$$L_T = E_C + E_S + E_E + E_A \tag{3.16}$$

Where L_T is the total load, E_C is the supplied energy from the collector and tank, E_S is the absorbed energy by the HP from the source, E_E is the electrical energy required to run the HP and E_A is the secondary energy input. The performance of an HP is evaluated by calculating its COP, which is the ratio of "free" energy to the net load. This is given in Equation (3.17) (Duffie and Beckman, 2013).

$$COP = \frac{E_C + E_S}{L_T} \tag{3.17}$$

3.4 Underground thermal energy storage

Thermal energy storage stores heat energy and extract it for future consumption using the time-dependent heat transfer approaches. In the analytical method for modeling of heat transfer systems such as the UTES, two basic approaches are employed: the lumped capacitance approach and the analytical approach using the Fourier heat conduction expressions (Laloui and Rotta, 2020). The lumped capacitance leverages the energy balance and permits time-dependent heat profile modeling for systems assumed to possess a uniform temperature variation during the transient heat transfer process, while the analytical approaches leverage the Fourier's equation for heat conduction to permit time-dependent heat transfer modeling of the system. Both approaches yield acceptable results; however, unlike the lumped capacitance approach, where the temperature within the system is assumed uniform, the temperature variations within the system control volume cannot be neglected in the analytical approach.

3.4.1 Lumped Capacitance Method (LCM)

Typically, when a solid body which is at an initial temperature T_1 and a heat capacity C_p volume, *V*, mass, *m*, and density, ρ, is placed in a fluid having different temperature T_2 at a time, $t = 0$, or the fluid is allowed to come in contact with the solid body, lump capacitance model assumes the heat transfer between the fluid and the body to be conventional with a heat transfer coefficient, h_f, and the temperature of the body is uniform and only changes with time $T = T(t)$. According to Laloui and Rotta, (2020), the energy balance of this case study is given in Equation (3.18) as:

$$h_f A_s (T_2 - T) = mC_p \frac{dT}{dt} = \rho V C_p \frac{dT}{dt} \tag{3.18}$$

Solving the energy balance by considering necessary parameters and integrating from $t = 0$ to any other time, t, The Equation (3.19) is obtained (Çengel and Ghajar, 2015).

$$\frac{T(t) - T_2}{T_1 - T_2} = e^{-bt} \tag{3.19}$$

Where: $\mathrm{b} = \frac{h_f A_s}{\rho V C_p}$ referred to as the time constant with unit $(time)^{-1}$. This concept enables us to determine the change in temperature of the body at any time, t and consequently determine

the net heat transfer occurring between the body and its surrounding, say the fluid. The heat transfer is therefore given in kJ in Equation (3.20) as:

$$Q = mC_p[T(t) - T_1] \tag{3.20}$$

Although the lumped capacitance model is simplified and provides an adequate heat transfer profile, it has its own limitations and is used under certain conditions. First, the characteristic length L_c, which is the ratio of the Volume of the body to the surface area, must be determined, followed by determining the Biot Number as shown in Equation (3.21) (Çengel and Ghajar, 2015).

$$Bi = \frac{hL_c}{k} = \frac{h}{k/L_c}\frac{\Delta T}{\Delta T} \tag{3.21}$$

Where h is heat transfer coefficient and k is the thermal conductivity of the material. This is the ratio of the convection heat transfer on the surface of the body to the conduction heat transfer within the body. The lumped capacitance method is exact, when the Bi = 0 and approximate when $Bi > 0$. The acceptable value where the lumped capacitance method is acceptable is when $Bi \leq 0.1$ although it can also be applied without satisfying $Bi < 0.1$ depending on whether high accuracy is required or not.

3.4.2 Analytical approach for heat conduction

This approach can evaluate the temperature changes of the body, such as the ground, when the Biot number is not small or within the acceptable range for LCM application and when the temperature changes cannot be neglected. Generally, for a one-dimensional problem of a cylindrical pipe in a medium, Fourier's equation for conduction is stated as given in Equation (3.22) and is applied, considering all necessary boundary conditions (Çengel and Ghajar, 2015). For example, a constant conductivity problem for steady-state, transient state with no heat generation, and steady-state, no heat generation is shown in Equations (3.23), (3.24), and (3.25) (Çengel and Ghajar, 2015).

$$[Rate\ of\ change\ of\ internal\ energy\ of\ the\ element] \tag{3.22}$$
$$= [Rate\ of\ \ heat\ conduction\ at\ a\ radius, r\ ]$$
$$- \ [Rate\ of\ heat\ conduction\ at\ a\ radius, r\ +\ dr]$$
$$+ \ [Rate\ of\ heat\ generation\ inside\ the\ element]$$

$$\frac{1}{r}\frac{d}{dr}\left(r\frac{dT}{dr}\right) + \frac{\dot{q}}{k} = 0 \tag{3.23}$$

$$\frac{1}{r}\frac{\delta}{\delta r}\left(r\frac{\delta T}{\delta r}\right) = \frac{1}{\sigma}\frac{\delta T}{\delta t} \tag{3.24}$$

$$\frac{d}{dr}\left(r\frac{dT}{dr}\right) = 0 \tag{3.25}$$

Where d is the diameter of the piping material, r is its radius, $\dot{q}$ is heat transfer rate, k is the thermal conductivity of the material, and T is the temperature. The term $\sigma = k/\rho C$ is the heat diffusivity of the body and represents the rate at which heat travels through the body where C is the heat capacity.

3.4.3 Thermal Resistance approach

When modeling heat transfer in a large medium like the ground, the thermal resistance approach can be used. This approach considers the flow of heat to be similar to the flow of electric current in a circuit. In time-dependent systems like underground thermal energy storage, two things are important. First, the rate of heat in the storage volume, which is determined by the temperature difference between the working fluid and the ground must be considered. Second, the time-dependent temperature difference, which considers the rate of heat transfer must be factored in. In general, these two considerations are combined to give the mathematical expression presented in Equation (3.26) as defined by Laloui and Rotta, (2020):

$$\dot{Q} = A\dot{q}_o = \frac{\bar{T}_f(t) - T_{ini}}{R_{total}(t)} = \frac{\bar{T}_f(t) - T_{ini}}{R_b + G_f\ (x_i, t)} \tag{3.26}$$

Where $\overline{T}_f(t)$ is the mean temperature of the working fluid, T_{ini} is the initial temperature of the ground, A is the total heating surface, $\dot{q}_o$ is the heat flux, and $R_{total}(t)$ is the total heat resistance. While R_b is the time-independent heat resistance, the term $G_f\ (x_i, t)$ is the time-dependent function of the heat resistance that considers the coordinate, x_i over the time, t,

often refers to as the G-function. Further methods of modeling heat transfer in restructures are explained vividly by Laloui and Rotta, (2020).

3.5 Simulation Tools

Simulation tools are the computer tools used for simulating different systems for proper analysis so as to describe fully the dynamic behavior of systems. Researchers tend to provide answers to some research questions through chains of experimentation, and this has proven difficult in its own ways because practical problems involve a lot of variations and uncertainties. In most cases, experimentations became impossible due to their excessive time consumption, exchange, and the technical, social, and economic implications. Modeling and simulation have been identified to solve the problems associated with experimentations since they reduce significantly the number of repetitive and iterative experiments (Shrivastava et al., 2017). Recently, it has been referred to as numerical experimentation, where the analytical results are dependent on the accuracy of the mathematical models. Many studies have been carried out utilizing different software for thermal and electrical energy systems.

3.5.1 TRNSYS and MATLAB Software

TRNSYS is a flexible and graphical simulation tool that is used based on the designed environment to simulate the dynamic and transient behavior of systems. Although this software can be used for simulating such systems as traffic flow and biological processes, it is commonly used for investigating electrical and thermal energy systems. TRNSYS contains two parts – the engine, often referred to as the kernel, and the library. The kernel is the part that reads and processes the input parameters and solves them using iteration methods for the determination of their convergence and plotting of the system variables for interpretation. It also makes available utilities that find the thermophysical properties and inverse metrics, carry out regressions, and interpolate external files. In literature, it has been used to investigate energy systems by (Li et al., 2020; Plytaria et al., 2018; Ramos et al., 2017).

CHAPTER 4: METHODOLOGY

Various steps are followed to model and simulate a solar-assisted dual-source heat pump combined with underground thermal energy storage (UTES) for application in water heating, building space heating, and cooling. In this chapter, the methodology for the current study is presented. First, the technique for developing, simulating, and calibrating inverse grey-box models for horizontal and vertical UTES configurations was explained. Similarly, the approach for developing a simulation model in TRNSYS and the application of the calibrated models for a public building is presented. Further to this, the parametric analysis methods for determining the models' sensitivity were presented.

4.1 Development and Evaluation of Inverse Models for Underground Thermal Energy Storage

4.1.1 Experimental set-up and measurement

Inverse grey-box models for the UTES system were developed and calibrated for application. To accomplish this specific objective, an experimental investigation of shallow UTES for horizontal and vertical configurations was carried out. The experiment was set up at the Korea Institute of Energy Research located in Daejeon, South Korea, with the main purpose of obtaining data for calibrating the inverse models for universal application. Figure 4.1 shows an overview of the site installation of the thermal energy storage for vertical and horizontal configurations with experimental set and measurement shown in Figure 4.2 as well as the dimensions depicted in Figure 4.3.

For these shallow UTES systems, the borehole pipes were installed at a depth of 2 m below the earth surface although to create rooms for insulations and grouting materials, the total depth dug was 2.5 m. The total lengths of pipe installed were 56 m and 189 m for vertical and horizontal configurations, respectively. Additionally, the surface dimension for the storage volume for each configuration was 4.0 m x 3.4 m x 2.5 m as shown in Figure 4.3, and to minimize the effects of thermal losses, the systems were improved by providing insulations by the sides and top of the storage volume using a rigid polyurethane foam.

a) b)

Figure 4.1: An overview of the underground thermal energy storage a) vertical configuration, and b) horizontal configuration

On the top of each storage volume, an insulation of thickness, 0.2 m was provided 0.3 m from the soil surface while the same was done for the sides of the storage volume where 0.2 m insulation was provided, just after the piping materials. Six temperature sensors of precision ± 0.5 ℃ were installed vertically downward at a distance of 0.3 m from each other, just 0.2 m away from the side insulation on the east, west, north, and south of the storage volume to measure the ground temperatures as indicated in Figure 4.2. The resistance temperature detector (RTD) sensors were given nomenclatures of TV_E_i, TV_W_i, TV_N_i, TV_S_i, and TV_C_i for the east, west, north, south, and center of the storage volume for the vertical configuration in contract to the horizontal configuration whose temperature sensors were named TH_E_i, TH_W_i, TH_N_i, TH_S_i, and TH_C_i for east, west, north, south and center of the storage volume where i represent the sensor number progressing downwards into the depth of the storage volume. Similarly, at the sides of the storage volumes, immediately after the insulation, temperature sensors, TV_o_i and TH_o_i for vertical and horizontal systems, respectively were installed vertically downwards to determine the effectiveness of the insulation in preventing the thermal losses. The location of this sensor is shown in Figure 4.4 for a better visualization.

The experimental investigation was such that during the heat storage (ground charging) phase, water was heated using the auxiliary heater to a temperature of 65 ^{o}C, and supplied to the storage volumes, at varied flow rates between 0 – 550 kg/h for the horizontal configuration, and flow rates between 0 – 1560 kg/h for the vertical configuration.

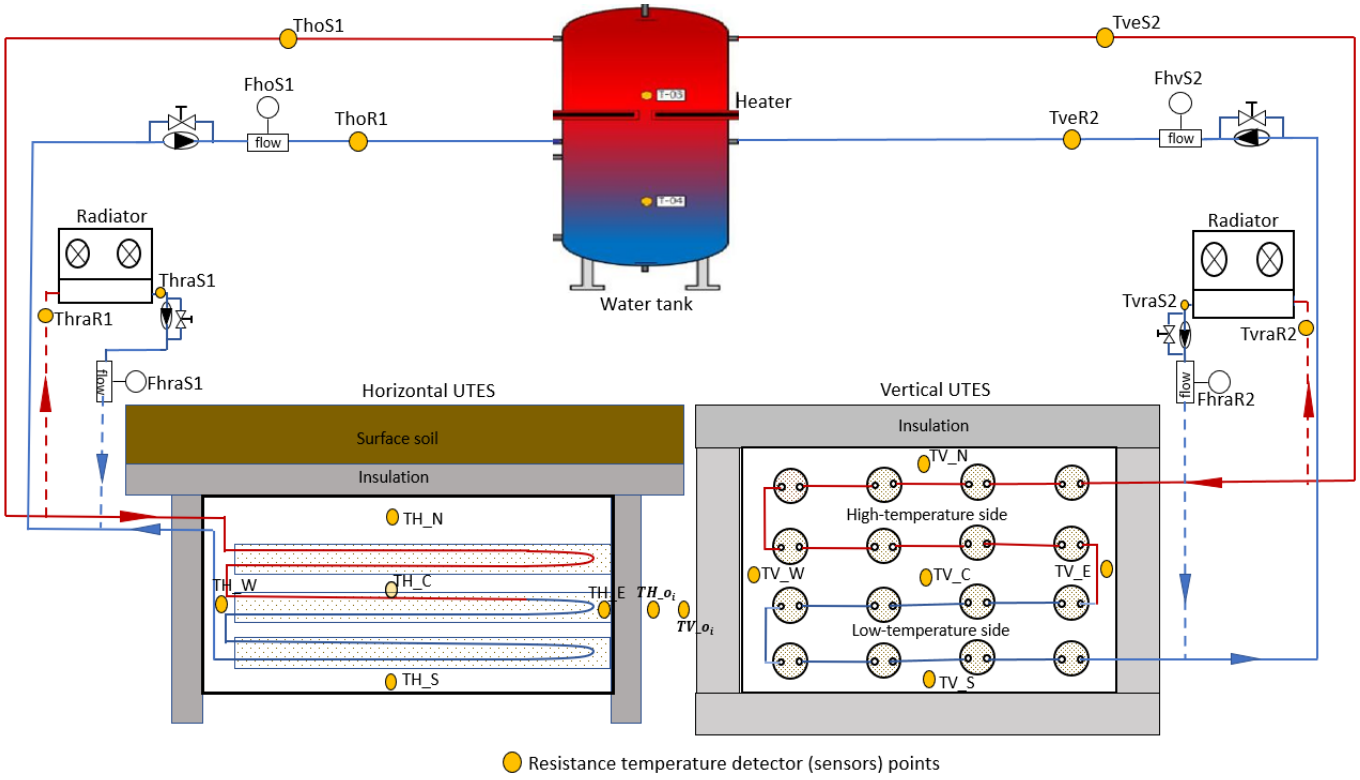

Figure 4.2: Experimental set-up and measurement

To measure the supply and return temperatures of the thermal storage systems, temperature sensors, $TveS2$ and $TveR2$ were installed, with corresponding magnetic flow meter, $FhvS2$ of precision ± 0.5 kg/h to measure the flow rates for the vertical configuration. Similarly, temperature sensors, $ThoS1$ and $ThoR1$ were installed to measure the supply and return temperature for the horizontal configuration with a corresponding flow meter labeled $FhoS1$ for measuring the flow rate during the experiment. During the heat release (ground discharging) phase, water at a constant temperature of 20 ^{o}C was supplied to the systems from the installed radiators as indicated in Figure 4.2. Similarly, the supply and return temperature sensors, $TvraS2$ and $TvraR2$, were installed to measure the supply and return temperatures from the radiator, respectively for the vertical configuration. Additionally, supply and return temperature sensors $ThraS1$ and $ThraR1$ were installed for measuring the supply and return temperatures from the radiator, respectively, for the horizontal system. Furthermore, flow meters, $FhraS1$ and $FhraR2$ were installed for measuring the flow rates of the fluid during this phase for the horizontal and vertical configurations, respectively.

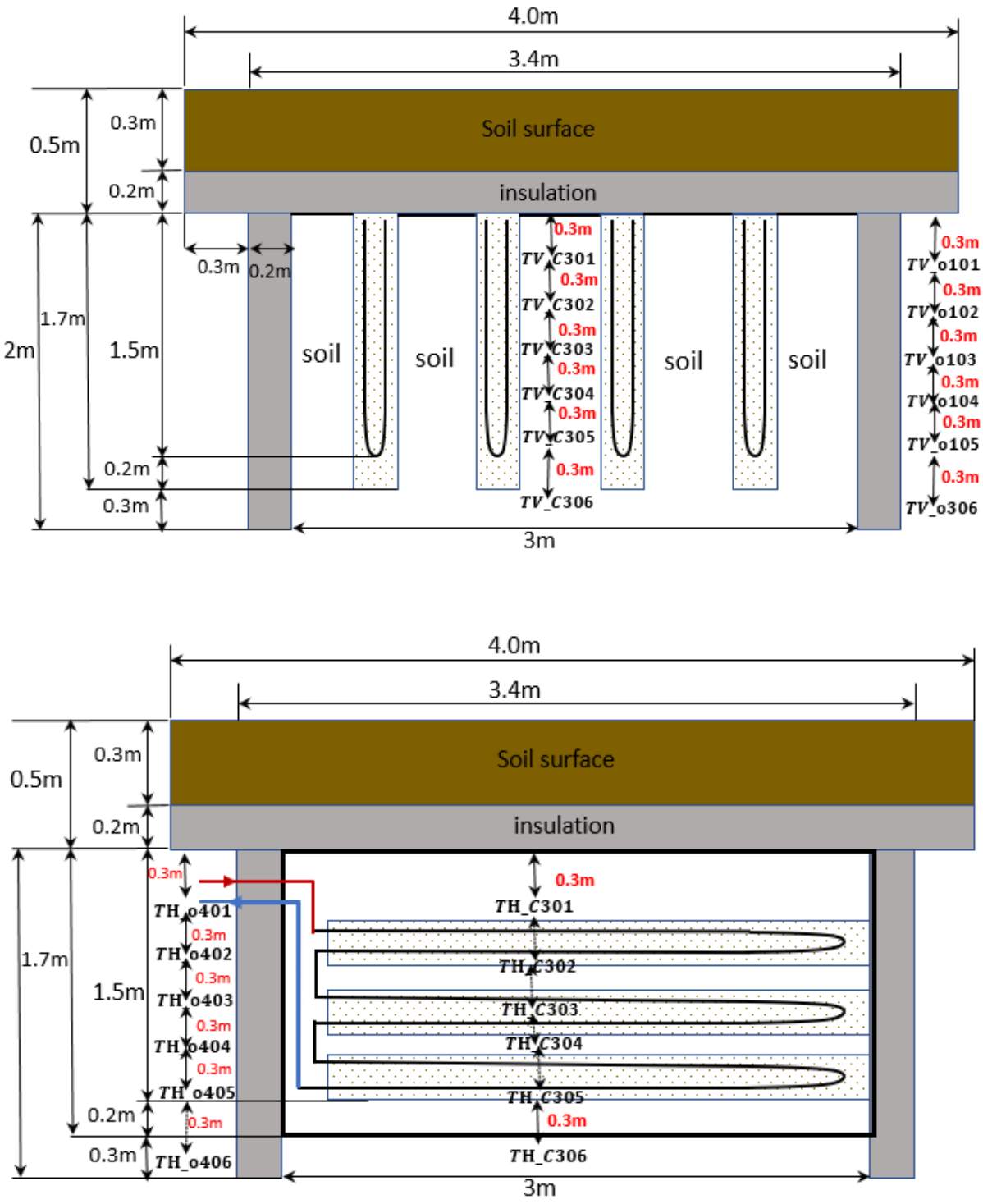

Figure 4.3: Installation and dimensions of the UTES, a) vertical configuration and b) horizontal configuration

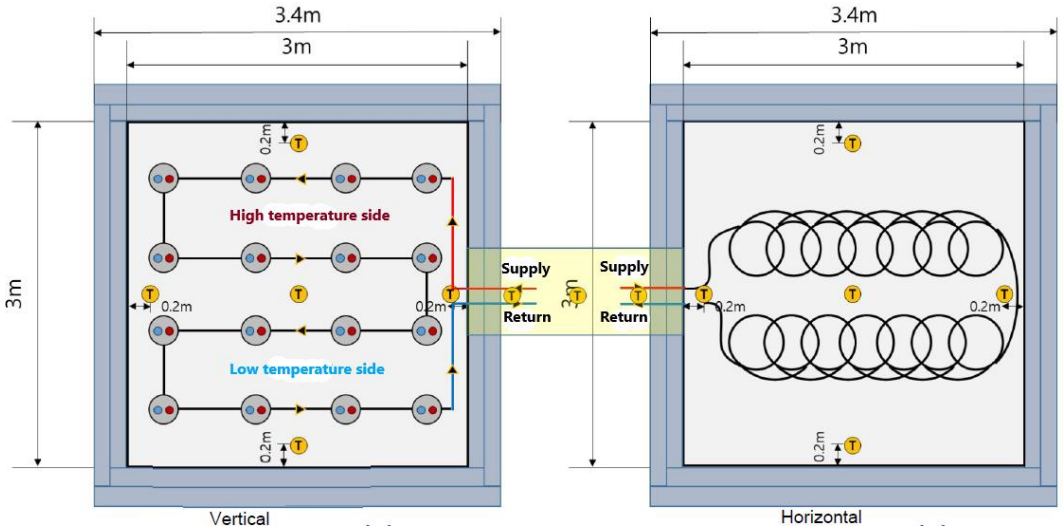

Figure 4.4: Diagram of the top view of the installation

4.1.2 Development of Detailed TRNSYS Grey-box Model

In this study, a detailed TRNSYS model that can properly represent the field experiment was developed for the vertical and horizontal configurations using TRNSYS simulation tool (*TRNSYS - Official Website*) as shown in Figure 4.5. Standard U-tube ground heat exchanger (Type557a) from the TRNSYS TESS library was used for modeling the vertical configuration as shown in Figure 4.5a. Measured meteorological data such as the solar irradiance, ambient temperature, etc. specific for the site was used to model the weather, using Type15 from the TRNSYS component library. For the horizontal model, standard Type997 from TRNSYS library, and the same weather data and type was used. The weather data and the data collected during the experiment were utilized as input to identify system driving parameters which were used for the model calibration. To achieve adequate model calibration, Type583, a generic optimization program (GenOPT) developed by the National Renewable Energy Laboratory (NREL) in the United States, was used. The model impacting parameters, such as soil's thermal conductivity, heat capacity, and density, are not known and are challenging to determine. Therefore, they were approximated by an optimization method, utilizing reasonable lower and upper limits adapted from experimentally determined values present in literature (ASHRAE, 2014; Aydin et al., 2012; Kodešová et al., 2013; Nikiforova et al., 2013). For calibration of this model, Hook-Jeeves Optimization algorithm was employed. This algorithm uses a direct search method for finding the local minimum point of a function, which is particularly useful when

gradient information is not available. It relies on comparing function values at different points to guide the search for a minimum. It is a simple yet effective method for solving non-linear optimization problems in various fields, including engineering, economics, and computer science; hence is the most suitable for the model calibration in this study. Optimal values of the driving parameters were obtained and recorded in each complete iteration. The best iterate was used to improve calibration and calculate the Root Mean Square Error (RMSE) and the Coefficient of Variation of the RMSE (CVRMSE).

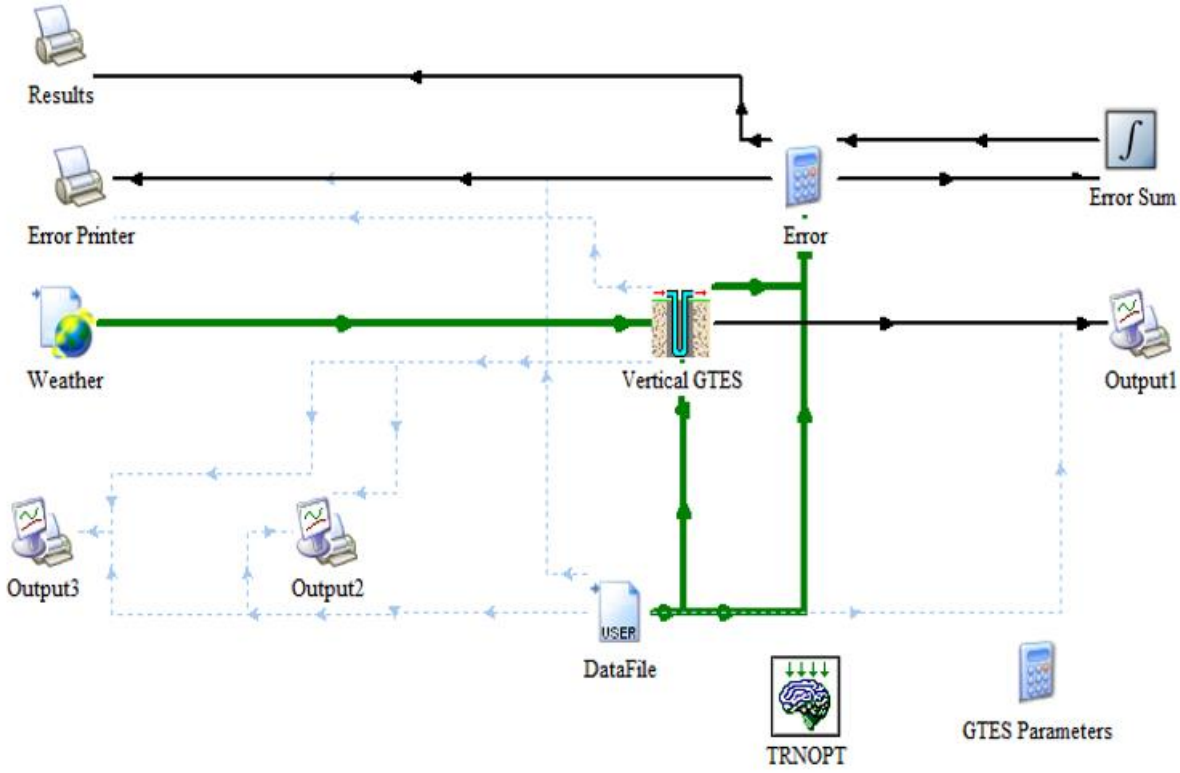

a)

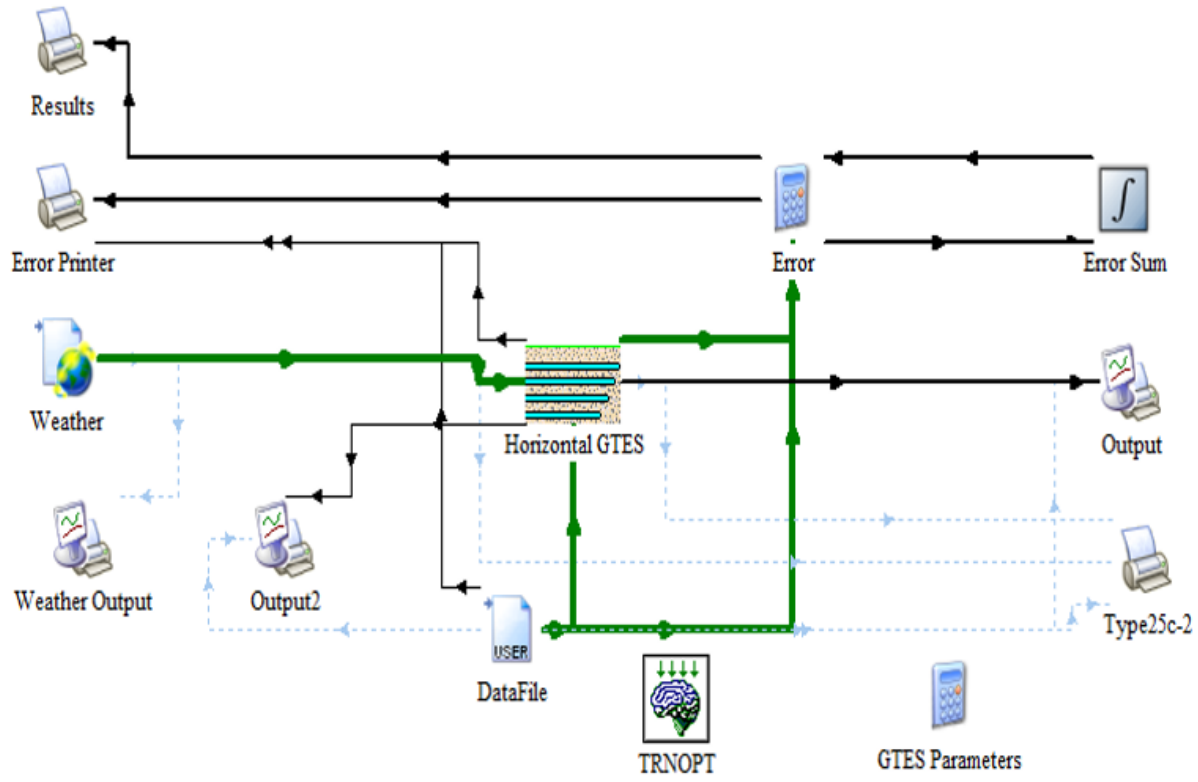

b)

Figure 4.5: Detailed TRNSYS model representing the field experiment, a) vertical configuration, b) horizontal configuration

4.1.3 Development of the Inverse Models

A simplified inverse model was developed for performance prediction of the vertical and horizontal UTES systems using thermal network analysis. For the vertical configuration as shown in Figure 4.6, the U-tube heat exchanger is considered, alongside the top and side insulations of the system. For simplification, one side of the U-tube is considered bearing in mind the heat interaction of the fluid-to-ground with the mean temperature of the inlet and exiting fluid in the pipe. The effects of the ground temperature outside the insulation, T_G and the ambient temperature, T_a over the storage volume were taken into consideration. As a result, a 4 resistance, 2 capacitance model was developed, considering 5 nodes as shown in Figure 4.6b with the following assumptions:

- The effects of ground water were not considered since the system dept is shallow
- Component materials are assumed to be isotropic, homogenous, and categorized by effective parameters
- Fluid-to-pipe and air-to-ground heat transfer is regarded as convection heat transfer

only while the heat transfers within the pipe materials, grout, and the ground is by conduction only.

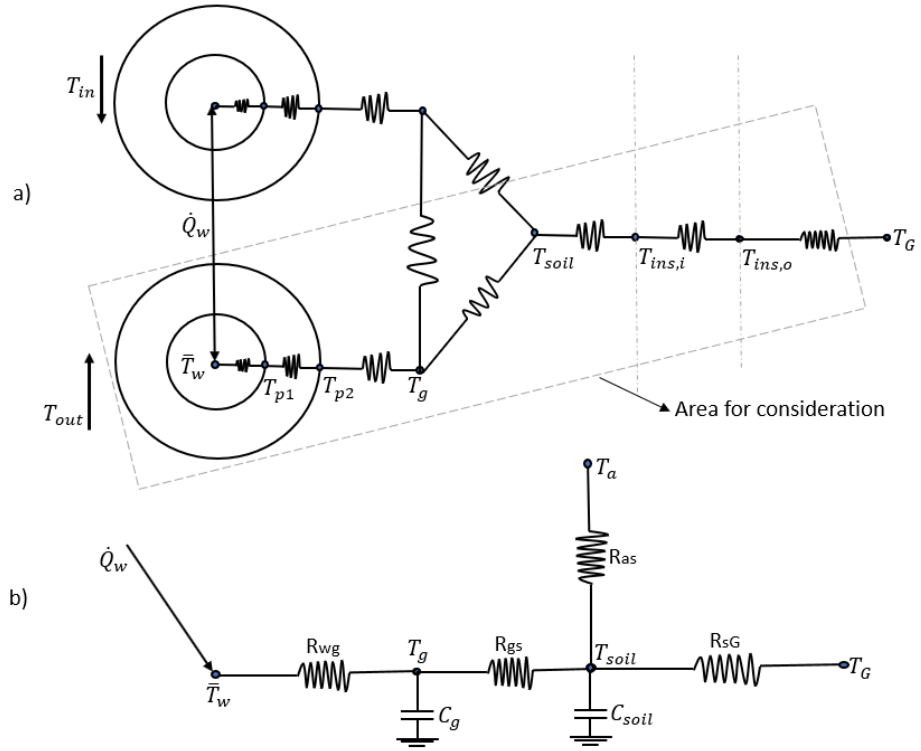

Figure 4.6: Simplified inverse model for vertical UTES type. a) detailed heat interaction in the U-tube heat exchanger, and b) simplified 4R2C thermal network.

Consequently, the following equations for the nodes were obtained:

For node $\bar{T}_w$:
$$0 = \dot{Q}_w + \frac{T_g - \bar{T}_w}{R_{wg}} \tag{4.1}$$

$$Where\ \bar{T}_w = \frac{T_{in}+T_{out}}{2}\ \ and\ \ \dot{Q}_w = \dot{m}_w c_{pw}(T_{in} - T_{out}). \tag{4.2}$$

For Node T_g:
$$C_g \frac{dT_g}{dt} = \frac{\bar{T}_w - T_g}{R_{wg}} + \frac{T_{soil} - T_g}{R_{gs}} \tag{4.3}$$

For node T_{soil}:
$$C_{soil} \frac{dT_{soil}}{dt} = \frac{T_g - T_{soil}}{R_{gs}} + \frac{T_a - T_{soil}}{R_{as}} + \frac{T_G - T_{soil}}{R_{sG}} \tag{4.4}$$

Where the effective capacitance of the soil, and the effective capacitance of the grouting materials for the vertical configuration are given in equations (4.5) and (4.6). Where all parameters are defined in the table of the nomenclature and abbreviations. The term α is the

user-defined factor that considers the thermal inertia of the systems defined by Maestre et al., (2013) and the storage volume, V_s is defined according to Thornton et al., (2014).

$$Where\ C_{soil} = \rho_s c_{ps} V_s\ with\ V_s\ =\ N\pi\Delta x(0.525 \times borehole\ spacing)^2 \tag{4.5}$$

$$Where\ C_g = \alpha\rho_g c_{pg} V_g = \alpha\rho_s c_{pg}\pi\left(l_b^2 - 2r_{p_o}^2\right)\Delta x \tag{4.6}$$

The thermal resistances (R_{wg}, R_{gs}, R_{as}, and R_{sG}) on the fluid-to-ground heat conduction path are defined in the following equations:

$$R_{wg} = \frac{1}{A_f h_f} + \frac{ln\left({}^{r_{p2}}/_{r_{p1}}\right)}{2\pi L k_p} + \frac{ln\left({}^{r_g}/_{r_{p2}}\right)}{2\pi L k_{grout}} \tag{4.7}$$

$$and\ R_{gs} = \frac{ln\left({}^{l_b}/_{r_g}\right)}{2\pi L k_{grout}} \tag{4.8}$$

Where,

$$l_b\ =\ \sqrt{r_b^2 + \left(\frac{d}{2} + r_p^2\right)^2} \tag{4.9}$$

$$r_g\ =\ \sqrt{\frac{l_b^2 + r_p^2}{2}} \tag{4.10}$$

In the same way, R_{as} and R_{sG} are obtained, considering the resistances on their heat transfer pathways as shown in equation (4.11) and (4.12).

$$R_{as} = \frac{1}{A_s h_{\_air}} + \frac{L_{surf,ins}}{A_{surf,ins} k_s} + \frac{L_{ins}}{A_{ins,top} k_{ins}} + \frac{L_{ins,s}}{A_{ins,s} k_s} \tag{4.11}$$

$$R_{sG} = \frac{L_{s,ins}}{A_{s,ins} k_s} + \frac{L_{ins}}{A_{ins,side} k_{ins}} + \frac{L_{ins,G}}{A_{ins,G} k_s} \tag{4.12}$$

The estimation of the heat transfer coefficient, h_f can be done by considering few dimensionless numbers such as the Reynold's, R_e, Prandtl, Pr, and Nusselt, N_u numbers adopted from Çengel and Ghajar, (2015) and Thornton et al., (2014). Mathematically they given in (4.13), (4.14), and (4.15) (Çengel and Ghajar, 2015).

$$R_e = \frac{\dot{m}_f D_i}{\mu_f} \tag{4.13}$$

$$P_r = \frac{c_{p,w}\mu_f}{K_f} \tag{4.14}$$

$$N_u = \begin{cases} 3.66 & (if\ Re \leq 2300) \quad laminar\ flow \\ 0.023Re^{0.8}Pr^{0.4} & (Re > 10000\ or\ 0.6 \leq Pr \leq 160) \quad rbulent\ flow \end{cases} \tag{4.15}$$

h_f can then be estimated using the relationship given in equation (4.16), with all parameters defined in the table of abbreviation.

$$h_f = \frac{N_u K_f}{D_i} \tag{4.16}$$

These nodal equations were solved to obtain the inverse models in the result section. The configuration was modified as shown in Figure 4.7 for derivation of the inverse model for the horizontal configuration. In this modification, the temperature on the grouting node, T_g was considered as the temperature of the ground, near the pipe while the soil temperature, T_{soil} is regarded as the temperature of the ground farther away from the pipe. With this modification and the following the dimension of the horizontal configuration, the model was calibrated for application.

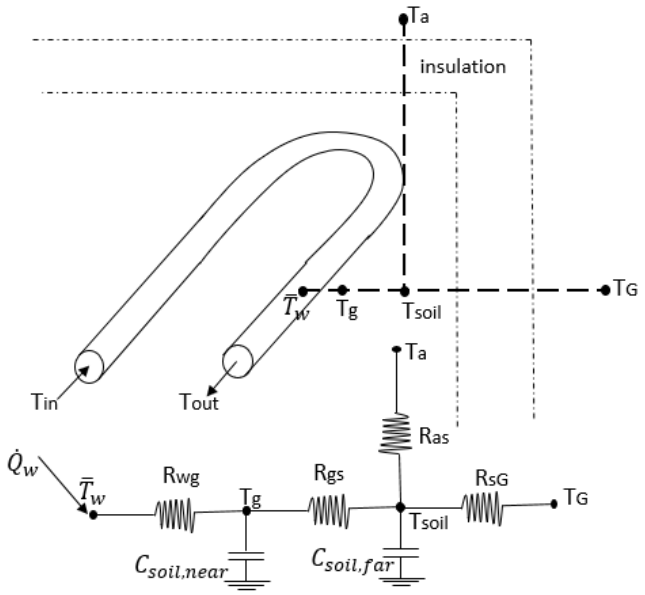

Figure 4.7: Modification for horizontal configuration inverse model

The developed model was modeled and simulated in MATLAB Simulink, with the assumption that the variation in inlet temperature over time ($\frac{dT_{in}}{dt}$) was minimal because the UTES was fed water at a stable temperature during the field test. Model parameters as shown in Figure 4.8 were optimized through training using the input (T_{in}, $\dot{m}_w$, T_a, $and\ T_G$) and the output (T_{out}) data. In this model, the ground temperature (T_G) is considered as a constant average effective temperature of the distant ground, beyond the insulation, to reflect the standard underground temperature. Thus, when T_G is unknown, such as in simulations with TRNSYS for model training and testing, the long-term average measured T_G is utilized as a constant, assuming the insulation maintains the temperature range. The nonlinear optimization method applied was the Trust-Region-Reflective algorithm (TRRA), which is optimal when gradient information is needed because it accommodates only upper and lower bounds or linear equality constraints, making it ideal for evaluating the model. Model calibration was based on the sum of squared error (SSE) and calibration accuracy was assessed using RMSE and CVRMSE.

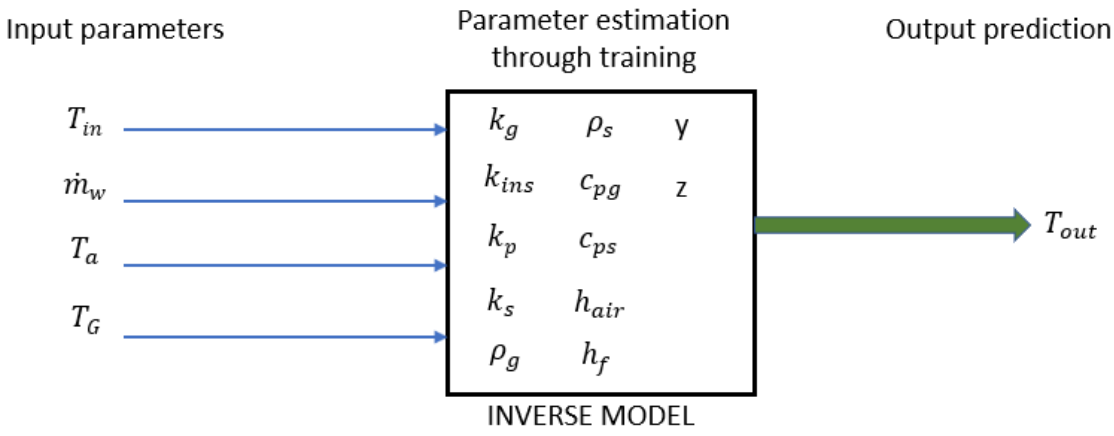

Figure 4.8: Relationship between the input parameters, driving parameters to estimate, and output parameter for calibration of the proposed model

4.1.4 Model Performance Index

The evaluation of the performance the developed the energy system model relies on statistical metrics like the coefficient of determination (R^2), root mean square error (RMSE), coefficient of variation of the mean square error (CVRMSE), and mean bias error (MBE) (Chakraborty and Elzarka, 2018). R^2 is significant for predicting system behavior through regression

analysis, while RMSE is widely preferred for its use of the sum of squared errors (SSE) between actual and predicted values to gauge accuracy (Chakraborty and Elzarka, 2018; Drucker et al., 2023; Hong et al., 2016; Pang et al., 2020). CVRMSE, which normalizes RMSE against the actual values' mean or range, adjusts for the scale of the data, with values below 20% generally being acceptable, though smaller values are preferable. Typically, the time-dependent objective function, J(t), is established for the SSE based on temperature variations, as indicated in equation (4.17). The objective function J(t) for calibrating the model, corresponding to the SSE, RMSE, and CVRMSE, is specified in equations (4.17), (4.18), and (4.19), respectively.

$$J = SSE = \sum_{i=1}^{N} (error\ (i))^2 = \sum_{i=1}^{N} \left(T_{out,\ sim}(i) - T_{out,\ exp}(i)\right)^2 \qquad i = 1, \dots, N \tag{4.17}$$

$$RMSE = \sqrt{\frac{\sum_{i=1}^{N} \left(T_{out,\ sim} - T_{out,\ exp}\right)^2}{N}} \tag{4.18}$$

Where N represents the number consecutive data points and i represents the present timestep.

The CVRMSE is then estimated using equation

$$CVRMSE = \left(\frac{RMSE}{\bar{T}_{out,\ exp}}\right) * 100 \tag{4.19}$$

Where $\bar{T}_{out,\ exp}$ represents the mean measured temperture over the simulation timestep.

4.2 Development of Simulation Models

4.2.1 Inter-seasonal power-to-heat and cool (P2HC)

Due to the existence of surplus energy generation from the solar PV installed in buildings, it has become inherent to develop a strategy for their utilization; hence the concept of the power-to-heat and cool (P2HC). This is simply the conversion of this excess electricity to hot or cold heat for utilization during the solar off-peak periods either for water heating, space heating or

cooling (Sukumaran et al., 2023; Wu et al., 2022). In this research, this concept is applied as shown in Figure 4.9. In general, electricity demand is usually high during winter and summer due to the high demand for heating and cooling, respectively. However, in the spring and autumn, when the weather is in its moderate conditions, less heating or cooling is required. This leads to the existence of surplus electricity generation from the installed solar PV or solar PVT on the building. However, during these periods, the study intends to apply the concept of P2H and P2C by using the UTES for their utilization. The system configuration, its operational strategy guided by simple control methods are explained explicitly in the following sections. Nonetheless, it is important to note that the dates for each season varies in different countries, however, this method is applicable globally by adjusting the dates in the control strategy.

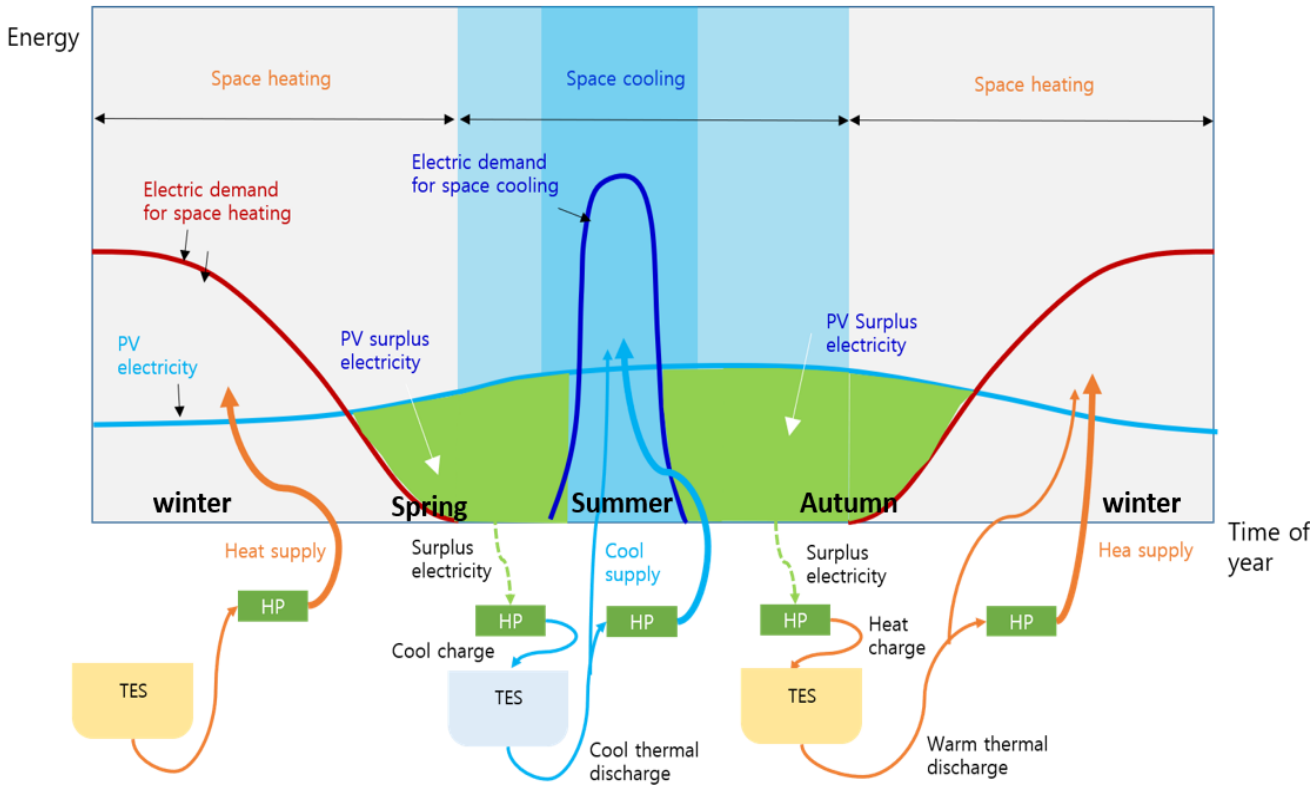

Figure 4.9: P2H and P2C concept in this research

4.2.2 System Configuration and Control Strategy

The system configuration for this study is such that the excess electricity generated from solar PV or PVT systems can be effectively utilized. To accomplish this, a novel self-consumption PV system combined with a dual-source heat pump, and seasonal underground thermal energy storage for enabling P2HC strategy is developed, with the configuration as shown in Figure

4.10b. The concept developed earlier depicts the energy demand flow as shown in Figure 4.10a, where for a given building, electricity generation from solar PV/PVT is used for meeting the domestic hot water demand, building space heating and cooling demands, and other electricity demands. However, since this demand varies with seasons, excess electricity generation are encountered. For proper utilization of this energy, the system in Figure 4.10b is developed. The operational strategy entails the utilization of the excess electricity to charge the UTES during non-heating and cooling seasons, which is then extracted during heating and cooling seasons for meeting the space conditioning demands. In this study four seasons – winter, spring, summer, and autumn are considered and the control strategy for the system are summarized thus:

- During spring and autumn, P2C and P2H operations take place, respectively, and no preheated or precooled ambient air is supplied to the heat pump. At this time, the pump, P2, is enabled, and the flow from HP to UTES is allowed through the valve, V1 and the control flow diverter (CFD), while the flow to the pump, P1 and from the flat-plat heat exchanger (HX) is completely prohibited. The excess electricity is used to charge the UTES with cold heat in spring (P2C operation) and with warm heat in autumn (P2H operation), lowering or raising the temperature of the ground accordingly.
- During the heating and cooling periods in winter and summer, respectively, the stored heat in the UTES is extracted for building space conditioning. The pump, P1, is enabled, and the working fluid from UTES is allowed to exchange heat with the ambient air in the HX. At this time, the valve, V1 and the CFD allow the flow to circulate within the UTES and the heat exchanger only, shutting off completely the flow from the heat pump (HP), and to the pump, P2. This action allows the ambient air that is passed through the heat exchanger to be preheated or precooled and then supplied to the source side of the heat pump for heating or cooling the building.
- The employed control strategy is extended such that the P2HC operation is only possible when surplus electricity generation from the solar PV/PVT system exists. This ensures self-consumption mode, implying that no electricity from the grid or any auxiliary energy supply is required to charge the UTES.

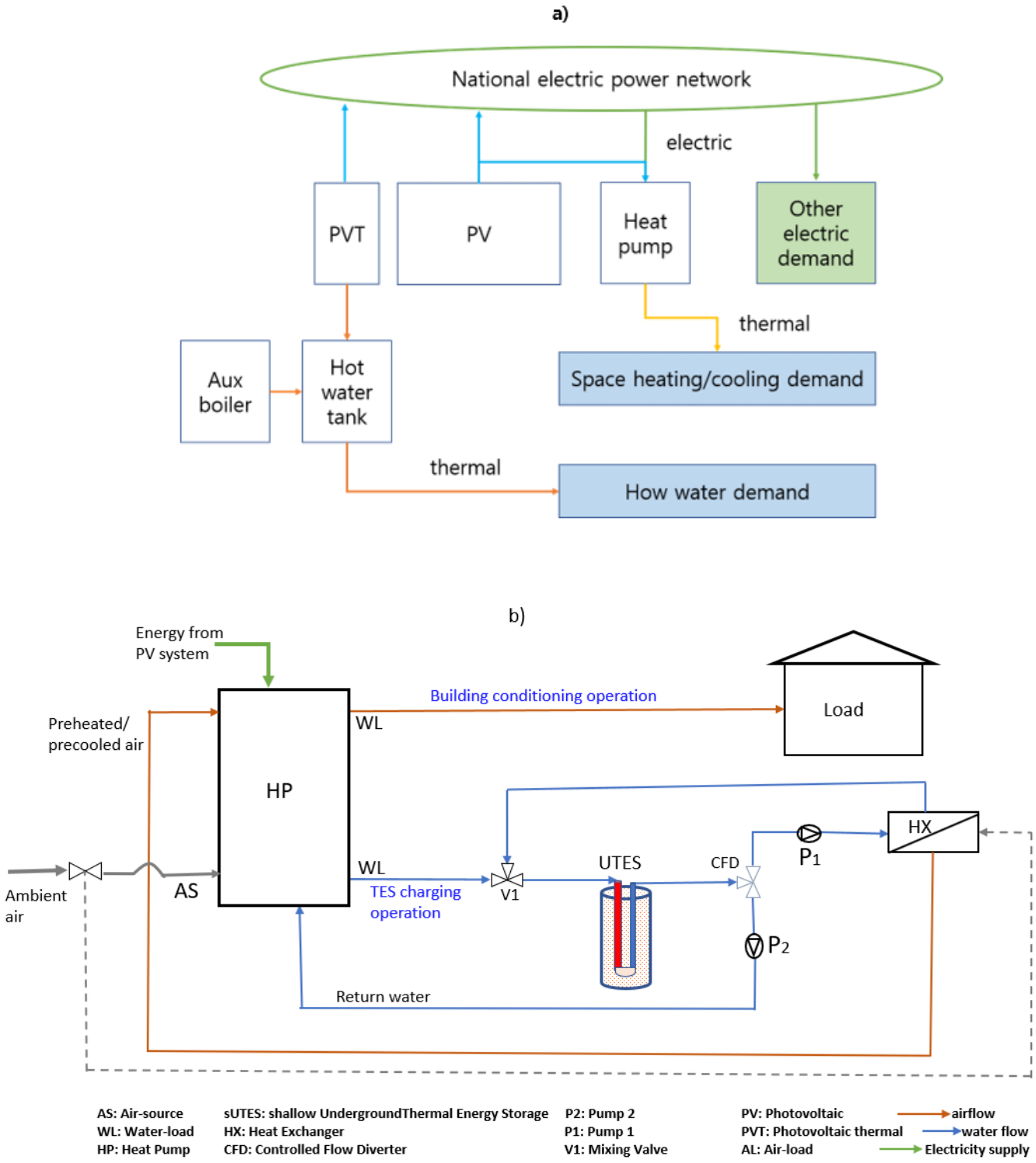

Figure 4.10: a) Energy demand flow for analysis b) Proposed system configuration

The control strategy in this research ensures that the starting and ending temperatures of the UTES remain roughly equal. This is crucial for preserving the yearly thermal equilibrium of the soil temperature within the UTES. This approach is especially beneficial in the test case of a ground-source water-load (GSWL) heat pump, where the heating and cooling requirements

are not aligned. Besides the previously mentioned control methods, the system incorporates heating and cooling dead bands. These dead bands, serving as control signals for heating and cooling, are intended to avoid the unnecessary and frequent activation or deactivation of the fluid and heat pumps. The heating dead band is maintained at a 4℃ range from 18℃ to 22℃, and the cooling dead band is kept at a 2℃ range from 24℃ to 26℃.

4.2.3 System Component description

4.2.3.1 Building Model

The developed model and its control strategy were tested on a typical public school building located in Jincheon City, South Korea. For simplicity, the building model was accomplished in TRNSYS using the Type88 lumped capacity model with details as shown in Table 4.1. The building is a four-story building with each floor having 1,312 m^2 total floor area from which thermal losses or gains occur. In the simulation study of this research, an assumption that each floor has its own heat pump was made. While the first floor contains the novel heat pump of interest, the second to fourth floors contain a conventional ASHP each with the same capacity and power consumption. In the actual building, the data for the power profile without the cooling systems proposed in this study was collected over a one-year period and matched with the installed PV capacity designed to meet the energy demand of the entire building, including the energy demand for the building space conditioning operations.

During the modeling of this building, factors such as the dry bulb temperature, humidity, infiltrating air flow, and latent heat gains were taken into consideration, as shown in the building energy balance in Figure 4.11, and mathematically expressed in equation (4.20). The parameters in the given equations are explained in the abbreviation section. Considering the Korean weather, the zone temperature is set to between 18 ^oC and 22 ^oC during the space heating period, accounting for a temperature deadband of 4 ^oC. Similarly, during the cooling season, the building zone temperature is set between 24 ^oC and 28 ^oC, accounting for a 2 ^oC temperature deadband. Furthermore, the building was assumed to be airtight; therefore, the $Q_{infiltration}$ was set to zero. The cooling and heating loads were calculated using equations (4.21) and (4.22), respectively.

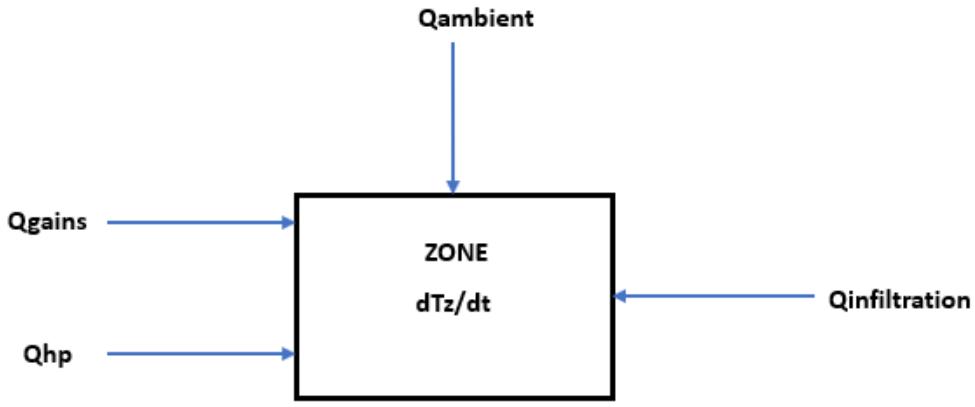

Figure 4.11: Energy balance of the building model

$$\frac{dT_z}{dt} \approx Q_{hp} + Q_{ambient} + Q_{infiltration} + \sum Q_{gains} \tag{4.20}$$

Where, $Q_{hp} = \frac{\dot{m}_{hp,air} c_{p,air}}{C}(T_{hp,out} - T_{z)}$

$$Q_{ambient} = \frac{UA}{C}(T_{ambient} - T_{z)}$$

$$Q_{infiltration} = \frac{\dot{m}_{inf} c_{p,air}}{C}(T_{inf} - T_{z)} = 0$$

$$Q_{cooling} = \int_{t_i}^{t_f} \left[\rho_{air} V_{zone} C_{p,air}\left(T_{zone} - T_{setpoint}\right) \times Occupancy\right] dt \tag{4.21}$$

$$Q_{heating} = \int_{t_i}^{t_f} \left[\rho_{air} V_{zone} C_{p,air}\left(T_{setpoint} - T_{zone}\right) \times Occupancy\right] dt \tag{4.22}$$

4.2.3.2 Solar PV Model

This particular component provides the energy required to meet the electrical and thermal loads of the case study building. This is shown in the energy demand flow of the building demonstrated in Figure 4.10. It provides the required energy for operating the heat pumps during the winter heating and summer cooling, as well as during the P2HC operations in spring and autumn. In addition, it provides other base electricity requirements, including the water pumps integrated into the system. In TRNSYS, this component was modeled using the Type50

with a sized area of 4000 m^2 to meet the required load. Detailed design parameters for this component is given in

Table 4.1. In the case of low energy generation from the PV, which happens in the winter, energy is tapped from the grid to completely meet the required demand.

4.2.3.3 Heat Pump Model

To evaluate the performance of the proposed system configuration and its control strategy, different types of heat pumps were modeled. Their designs are such that they must provide the required heating and cooling energy to meet the building's thermal loads. In this study, a conventional single-stage air-source air-load (ASAL) heat pump was modeled using the Type954 from the TRNSYS component library. This heat pump uses air on both the condenser and the evaporator parts and uses a reversible valve to operate in either cooling or heating modes. Usually, the ambient air is supplied to the source side loop while the outlet and return air on the load side loop are supplied to and from the building, respectively. Similarly, the air-source water-load (ASWL) heat pump was modeled using the single-stage Type941. This heat pump uses air on the source side to deliver energy to the liquid stream on the load side. Generally, the heat pumps use cooling and heating performance data obtained from the manufacturer, which are functions of the properties on the source side, such as the inlet air flow rates, inlet water flow rates, inlet air temperature, and the inlet water temperature and the properties on the load sides such as the inlet load temperatures and the inlet load flow rates. In this study, we utilized the cooling and heating performance data provided by the manufacturer. The specifications of the heat pump indicate capacities of 160 kW for both heating and cooling, with power consumption of 40 kW for cooling and 50 kW for heating. Moreover, the rated air flow rate is 10,000 L/s, and the liquid flow rate is 300,000 kg/h. These specifications were chosen to ensure sufficient heat supply to the building and effective charging of the thermal energy storage system.

4.2.3.4 Underground Thermal Energy Storage (UTES) Model

In this research, the detailed TRNSYS model for the shallow vertical UTES configuration developed and calibrated in section 4.2.3 was utilized with some adjustments made to the design parameters, such as the size. An 800 m^3 corresponding to 964 U-tube boreholes was designed based on the heat pump capacity and the building load through simulations while the depth remained at 1.5 m. The same insulation of 0.2 m at the top and sides of the system was

made available to prevent heat losses. To further evaluate the performance of the system configuration on the heat pump, a deep UTES of the same 800 m^3 in volume corresponding to 10 U-tube boreholes and a depth of 150 m was simulated. In general, the parameter specifications for these systems are given in

Table *4.1*. The UTES system is charged using the heat pump during the seasons when heating and cooling are not required (spring and autumn). The system's control strategy is designed to avoid overcharging and to ensure that the storage volume is not supplied with temperature below zero, by allowing the cooling and heating charge time to be adjusted. Equation (4.23) can be used to determine the size of the system, while equation (4.24) can be used to define the fluid-to-ground heat transfer rate during charging and discharging, as well as its performance indicator defined later in the study.

$$Volume = N * Depth * \pi * (0.525 * borehole\ spacing)^2 \tag{4.23}$$

$$Q_{charge/discharge} = \int_{t_i}^{t_f} \dot{m}_w C_{pw} (T_{in} - T_{out})\, dt \tag{4.24}$$

4.2.3.5 Heat Exchanger Model

In this study, it is noteworthy that the purpose of the UTES, except during the water-source air-load (WSAL) heat pump operation is to precool or preheat the inlet air entering the heat pump. For this purpose, a 4kW heat exchanger with air and water flow rates of 10,000 l/s and 300,000 kg/hr, respectively, was integrated into the system configuration to convert the thermal energy from the UTES to air, which is then supplied to the heat pump's source side. During summer cooling time, a Type 699 heat exchanger was used, which had constant effectiveness and could automatically bypass the liquid fluid hot side when needed to maintain the cold side air temperature set at 13°C. During the heating season, a Type 652 heat exchanger was used with constant effectiveness, and the hot-side water fluid was bypassed when needed to maintain the cold-side outlet air fluid temperature set at 25°C. These control strategies aim to regulate the air temperature preheated or precooled before its supply to the heat pump. The heat exchanger effectiveness value was set to 0.85, with the constant heat capacities of the air and liquid set as 1.02 kJ/kg·K and 4.19 kJ/kg·K, respectively.

4.3 Comparative Evaluation of Different Heat Pump Case Scenarios for Application

4.3.1 Case Studies for System Evaluation

To evaluate the proposed system configuration, along with its control techniques, different case studies were modeled, integrating the system components discussed in the last section with their corresponding baseline cases:

- **Case 1**: In this case, an ASAL heat pump with P2HC methodology using the shallow UTES developed in section 4.2.2 was modeled as shown in Figure 4.12 b) and simulated. In this model, the UTES is used to preheat and precool the ambient (sink) air temperature to the heat pump during heating and cooling periods, respectively, while the heat pump charges it during non-heating and non-cooling periods on the successful introduction of a heat exchanger as shown in Figure 4.13. This implies that the heat pump functions as a dual source and single load where both air and thermal energy from the UTES are used on the source side with a successful introduction of the heat exchanger, and air is supplied from and returned to the load side from the building. A conventional ASAL heat pump without P2HC was modeled and simulated for evaluation as shown in Figure 4.12 a).

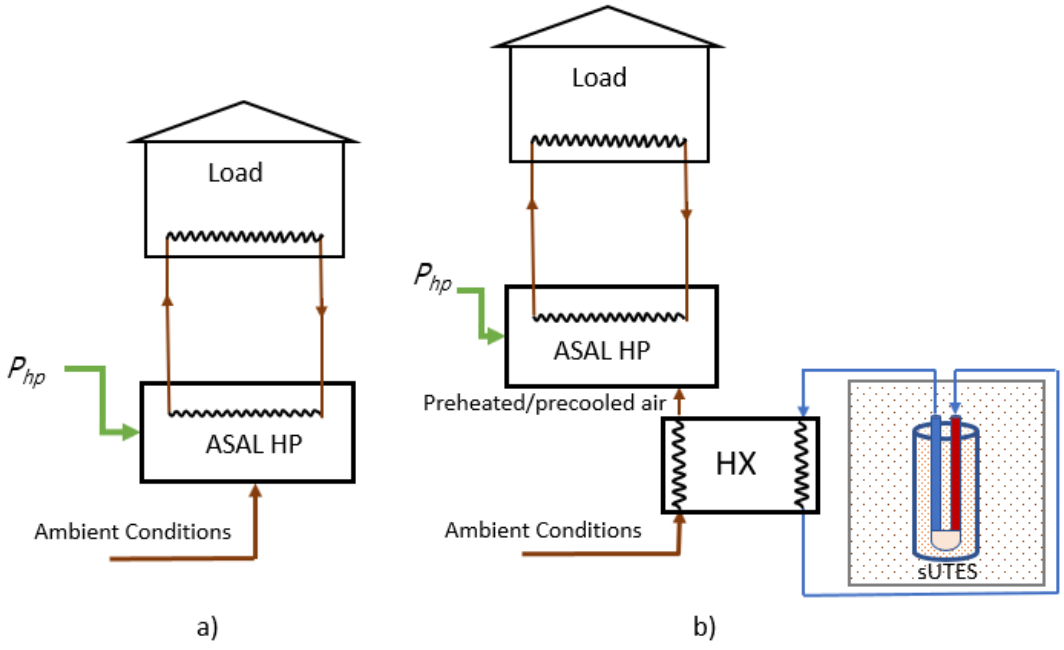

Figure 4.12: Study Case 1 for winter heating and summer cooling mode: a) Base Case with no P2HC operation and b) Test Case with P2HC operation

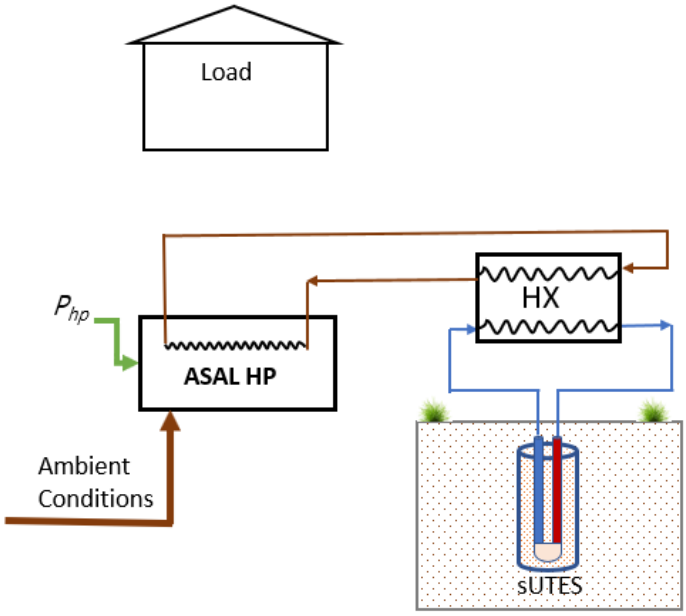

Figure 4.13: Study Case 1 in P2HC operation mode during the non-heating and non-cooling (spring and autumn) periods

- **Case 2**: In this case, an ASWL heat pump with P2HC methodology using the shallow UTES in section 4.2.2 was modeled as shown in Figure 4.14 b) and simulated. Similarly, the heat energy from UTES is used to condition the air supplied to the heat pump from the source side through the introduction of the heat exchanger. This heat pump also functions as a dual-source, single-load, where both air and liquid are supplied to the source side during UTES charging (Figure 4.15) and building conditioning, and only liquid is supplied to the load side. In this case, a buffer tank is introduced between the heat pump and the load such that the heat pump maintains its average temperature during cooling and heating seasons to a desired degree celcius. For simulation convenience, the heating and cooling loads obtained from case 1 were imposed on the heat pump liquid flow stream using the Type682 component. In this regard, the zone temperature is not of the greatest interest but the met load. Additionally, a base case of no P2HC methodology was modeled and simulated for performance evaluation as shown in Figure 4.14 a).

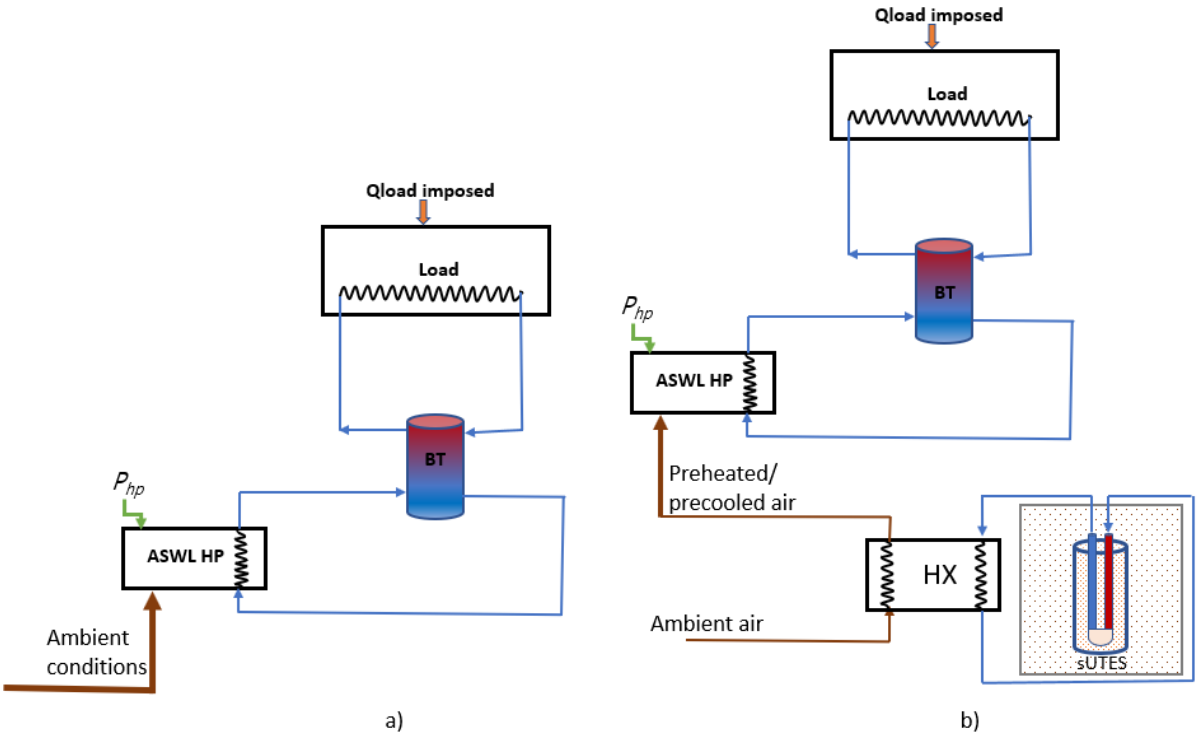

Figure 4.14: Study Case 2 for winter heating and summer cooling mode: a) Base Case with no P2HC operation and b) Test Case with P2HC operation

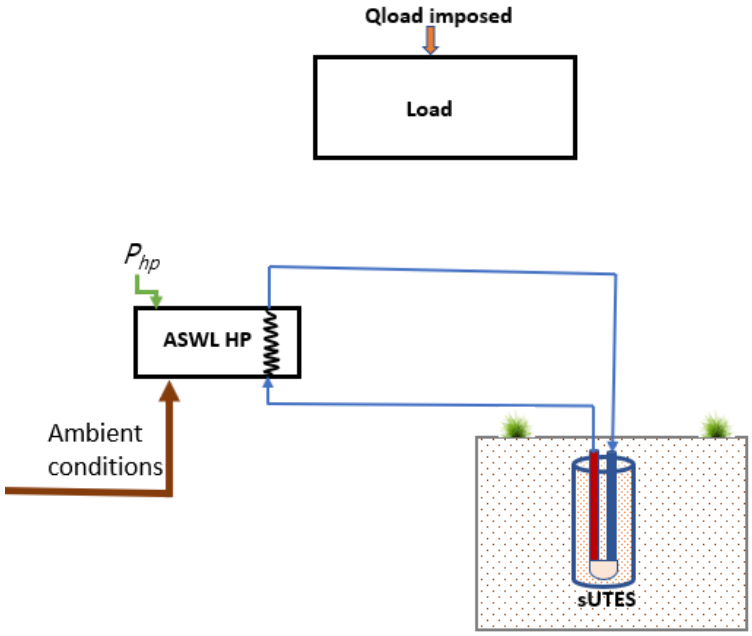

Figure 4.15: Study Case 2 in P2HC operation mode during the non-heating and non-cooling (spring and autumn) periods

- **Case 3**: This case features an ASWL heat pump with P2HC methodology as shown in Figure 4.14 b). However, in this case, the sUTES developed in section 4.2.2 was

replaced with the deep UTES Similarly, a base case of no P2HC methodology with deep UTES too was modeled and simulated for performance evaluation.

- **Case 4**: This case consists of a conceptualized dual-source dual-load heat pump with P2HC strategy that operates as an ASWL heat pump during spring P2C and autumn P2H operations, and as a WSAL heat pump during the winter and summer building space conditioning as shown in Figure 4.16. The heat pump is assumed to be capable of functioning effectively in both reversible order. The conventional case is the same as that of the case 1 for performance evaluation.

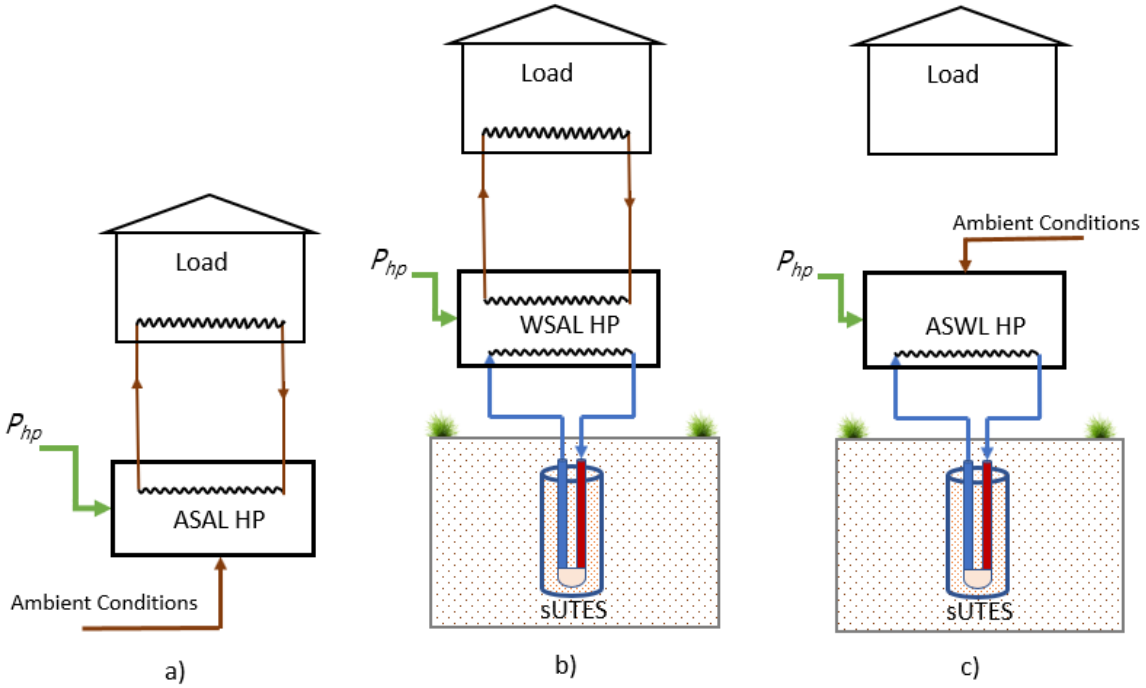

Figure 4.16: Study Case 4: a) Base Case with no P2HC operation, b) Test Case with P2HC operation in winter heating and summer cooling mode, and c) in P2HC operation mode during the non-heating and non-cooling (spring and autumn) periods.

4.3.2 System Performance Indicators

The proposed system configuration and the study cases were modeled and simulated over a typical year, maintaining stability and optimum performance. To evaluate the performance of these cases, six key performance indicators were defined as shown below:

1. **Self-consumption ratio (SCR):** Over the simulated year, solar PV system generates electricity, with the majority of the surplus occurring during the spring and autumn seasons when less or no heating and cooling is required. Therefore, SCR is defined as the ratio of the total PV electricity in kWh used for heating, cooling, P2HC operation, and other base electricity demand, including the water pumps integrated in the system per annum, $E_{PV,used}$ to the ratio of the net PV electricity that is generated by the PV system over the simulated year, $E_{PV,total}$. This is given mathematically as shown in equation (4.25). This performance indicator shows the percentage of the total generated PV electricity per annum that is consumed on-site without being sent to the grid.

$$SCR = \frac{E_{PV,used}}{E_{PV,total}} \times 100 \tag{4.25}$$

2. **Surplus Energy utilization Ratio (SEUR)**: This is a performance indicator to show the percentage of the surplus PV electricity that is consumed during the novel P2HC operation. It is defined as the ratio of the net PV electricity that is utilized for P2HC operation per year, $E_{PV,P2HC}$ to the net surplus electricity generated by the PV system per same year, $E_{PV,surplus}$. Mathematically, this is given in equation (4.26).

$$SEUR = \frac{E_{PV,P2HC}}{E_{PV,surplus}} \times 100 \tag{4.26}$$

$$Where\ E_{PV,surplus} = E_{PV,total} - E_{PV,used}$$

3. **P2HC Efficiency (η_{P2HC})**: This performance indicator examines the percentage of the PV power used for P2HC operation to the energy that is saved. It is defined as the ratio of the net energy saved by implementing P2HC per year, E_{saved} to the net energy used for P2HC operation per year, E_{P2HC}.

$$\eta_{P2HC} = \frac{E_{saved}}{\int_{t_i}^{t_f} E_{P2HC}\, dt} \times 100 \tag{4.27}$$

$$Where\ E_{saved} = \int_{t_i}^{t_f} E_{base}\, dt - \int_{t_i}^{t_f} E_{test}\, dt \tag{4.28}$$

Where E_{base} is the net energy consumed during heating and cooling periods in winter and summer for the base case and E_{test} is the net energy consumed during heating and cooling periods in winter and summer for the test case.

4. **Percentage Energy savings, $\boldsymbol{\beta}$**: This performance indicator explains the percentage of energy that is saved by implementing P2HC strategy in this study. It is defined mathematically as shown in equation (4.29).

$$\beta = \frac{E_{saved}}{\int_{t_i}^{t_f} E_{base}\, dt} \times 100 \tag{4.29}$$

5. **Seasonal Coefficient of Performance (SCOP)**: This indicator shows the seasonal performance of the heat pump. It is defined the ratio of the net heat transfer to the load by the heat pump per season, Q_{season} to the net power consumed by the heat pump per season, $E_{hp,season}$. It should be noted that power consumed by the heat pump includes the power consumption of the fan, E_{fan} and the compressor, E_{com}.

$$SCOP = \frac{Q_{season}}{E_{hp,season}} \times 100 \tag{4.30}$$

6. **UTES thermal Efficiency $\boldsymbol{\eta_{UTES}}$**: This is the thermall efficiency of the UTES over the operating period defined as the ratio of the net heat discharged (extracted) from the ground during heating and cooling, $Q_{extracted}$ to the net heat injected into the ground during the P2HC operation $Q_{injected}$. Mathematically, it is defined as given in equation (4.31).

$$\eta_{UTES} := \frac{\int_{t_i}^{t_f} Q_{extracted}\, dt}{\int_{t_i}^{t_f} Q_{injected}\, dt} \times 100 \tag{4.31}$$

Table 4.1: System component parameters

Parameters	**Value**	**Units**
Solar PV		
Module area	4,000	m^2
Collector efficiency factor	0.7	-

Fluid Thermal Capacitance	4.19	kJ/kg·K
Collector plate absorptance	0.9	-
Number of glass covers	1	-
Collector plate emittance	0.9	-
Loss coefficient for bottom and edge losses	20	kJ/hr·m^2·K
Collector slope	45	degrees
Extinction coefficient thickness product	0.03	-
Temperature coefficient of PV cell efficiency	-0.0003	1/K
Temperature for cell reference efficiency	20	C
Packing factor	0.5	-
Building Model/floor		
Building loss coefficient	6	kJ/hr·m^2·K
Building capacitance	783,125	kJ/K
Specific heat of building air	1.007	kJ/kg·K
Density of building air	1.2	kg/m^3
Building surface area	1312	m^2
Building volume	4500	m^3
Humidity ratio multiplier	10	-
Initial temperature	20	C
Initial humidity ratio	0.005	-
Latent heat of vaporization	2260	kJ/kg
Underground Thermal Energy Storage		
Storage Volume	800	m^3
Borehole Depth for shallow UTES Borehole Depth for deep UTES	1.5 150	m m
Header Depth	0.5	m
Number of Boreholes (shallow) Number of Boreholes (deep)	1386 14	
Borehole Radius	0.102	m
Storage Thermal Conductivity	15.975	kJ/hr·m·K
Storage Heat Capacity	5950.01	kJ/m^3/K
Outer Radius of U-Tube Pipe	0.016	m
Inner Radius of U-Tube Pipe	0.012	m
Center-to-Center Half Distance	0.05	m
Fill Thermal Conductivity	2.5	kJ/hr·m·K
Pipe Thermal Conductivity	11.149	kJ/hr·m·K
Reference Borehole Flowrate	3.0×10^5	kg/hr
Fluid Specific Heat	4.19	kJ/kg·K
Fluid Density	1000	kg/m^3

Insulation Thickness	0.2	m
Insulation Thermal Conductivity	0.2001	kJ/hr·m·K
Initial Surface Temperature of Storage Volume	17	^{o}C

4.4 Parametric Analysis

The parametric analysis in this study was done to identify how changes in the system parameters affect the overall system's performance. First, the essential parameters of the system were identified by carrying out 44 completed simulations, focusing on the design parameters. Consequently, an automation approach was employed by writing code on Excel VBA and linking it to the TRNSYS model, where changes in the identified parameters were tested to evaluate their impacts on the system performance.

4.5 Cost analysis of the system

To perform the economic analysis of the selected Case study system, various costs associated with the system components are sourced from literature and modeled based on economic criteria such as the levelized cost of heat (LCoH) as described. It is important to note that this section does not deal with the detailed economic analysis of the system, which requires careful and extended data collection. Since the study aims to examine the effects of integrating the UTES system for conversion of PV power to heat for assistance in improving the performance of the heating and cooling of the building space, this economic study focuses on determining the LcOH and the payback period of its cost. Figure 4.17 shows the boundary conditions in calculating the LCoH, giving rise to equations (4.32) and (4.33); however, equation (4.33) is the interest in this work and hence was coded in MATLAB for calculating the LCoH of the UTES. This economy has been used extensively in estimating the cost of heat of thermal systems, especially in the commercial and residential applications of underground seasonal thermal energy storage criteria (Kim et al., 2019; Li et al., 2023; Welsch et al., 2018; and Yang et al., 2021). It represents the ratio of the present value of all costs associated with the UTES system to the present value of all heat outputs over the lifetime of the system. It provides a way to compare the cost of heat produced by the UTES system over time.

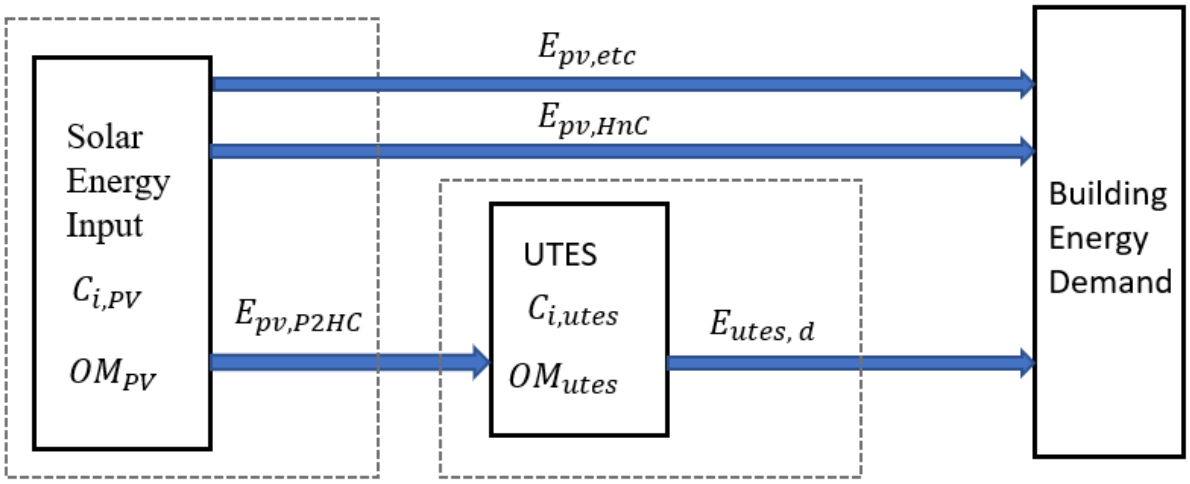

Figure 4.17: Cost Analysis using the levelized cost of heat (LCoH)

$$LCoH\ of\ solar\ PV\ input = \frac{C_{i,pv} + \sum_{t=1}^{N} \frac{(OM)_{pv}}{(1+r)^t}}{\sum_{t=1}^{N} \frac{E_{pv,P2HC} + E_{pv,HnC} + E_{pv,etc}}{(1+r)^t}} \quad (4.32)$$

$$LCoH\ of\ UTES\ input = \frac{C_{i,utes} + \sum_{t=1}^{N} \frac{(OM)_{utes}}{(1+r)^t}}{\sum_{t=1}^{N} \frac{E_{utes}}{(1+r)^t}} \quad (4.33)$$

Where *t* is the year number and other parameters defined as follows:

Initial Capital Cost, $C_{i,utes}$: This can vary greatly depending on the size and complexity of the UTES system and local factors such as geology and site conditions. In this study, the initial investment cost for the 800 m^3 was estimated based on the extrapolation of the cost of the shallow UTES installed at the test site as explained in section 0 and published paper for a study carried out in Korea by Kim et al., (2019). The cost was estimated to be USD 129.6/m^3, amounting to a total investment cost of USD 103680.00.

Annual operation and maintenance cost $(OM)_{utes}$: This includes routine maintenance, inspections, repairs, and any other ongoing expenses associated with operating the UTES system. Typically, this cost is a fraction of the initial capital cost and can range from 1% to 5% of the initial capital cost per year. In this study, 2% of the initial investment cost is used as the $(OM)_{utes}$.

Discount Rate (r): This represents the opportunity cost of capital or the rate of return that could be earned on alternative investments. In this study, a 5% discount rate used in Kim et al., (2019) was adopted. It should be noted that inflation rate is neglected as it has minimal effect in LCoH according to Welsch et al., (2018).

Annual heat output, E_{utes}: This depends on the heat demand of the building or process being served by the UTES system and the efficiency of the system itself. The annual heat extracted of 19064.48 kWh from the ground for heating and cooling purposes in Case 2 is used for this parameter as shown in Figure 4.17.

Lifetime of the project (N): This is the timeframe over which the costs and benefits of the UTES system are considered. It can vary depending on factors such as the expected lifespan of the system and the duration of financing arrangements. In this study, 25 years was chosen to correspond with the lifespan of the PV system before decommissioning.

CHAPTER 5: RESULTS AND DISCUSSION

5.1 Introduction

In this chapter, the findings of the present study are reported and discussed. The sole aim of this study is to model and simulate a dual-source heat pump that is assisted (powered) by the energy generated from solar PV systems while exploring the application of underground thermal energy storage (UTES), that seasonally stores the surplus electricity generated by the solar PV system through power-to-heat (P2H) and power-to-cool (P2C) operations in different seasons of the year. The system operates such that during the non-heating and cooling seasons, the electricity generated by the solar PV is injected into the ground through the heat pump in the form of heat, thereby charging the UTES system. In this operation, ambient conditions, specifically the ambient air, are supplied to the source side of the heat pump. During the heating and cooling seasons, the heat is extracted to heat or cool the building through the use of the heat pump. In this operation, the thermal energy extracted from the UTES is used to condition the air that is supplied to the heat pump through the successful application of a heat exchanger. This is the phenomenon that describes the dual-functionality of the heat pump. To accomplish this broad objective, some specific objectives were accomplished as described in the following sections.

5.2 Development and evaluation of inverse models for the UTES

5.2.1 Experimental study

The improved vertical and horizontal shallow UTES was accomplished experimentally by installing both systems with insulation at the top and sides of the systems. The field experiment was conducted between March to July 2023. Both system configurations received water at 35°C for an initial two-week period dedicated to heat storage. Subsequently, a one-week phase focused on heat release involved supplying water at 15°C to the systems. Over the following two weeks, the temperature was gradually raised to 45°C. This was followed by a seven-week period of natural heat dissipation, during which no additional heat was introduced to the ground, resulting in zero flow rates. Finally, two additional weeks were allocated for heat storage, with water supplied at 45°C. Water and ground temperatures were measured and recorded accordingly. It is important to emphasise that the sole purpose of this experiment is

to obtain the field experimental data for calibration of the developed inverse models. However, the results of the experimental outcome are shown in the following sections.

5.2.1.1 GTES water outlet temperatures

The water outlet temperature for both configurations behaved differently, as observed from Figure 5.1 a) although this is partly as a result of the variation in their flow rates. The horizontal configuration increased more rapidly at the start of each storage time and attained its peak at the 117, 102, and 78 hours in the first, second, and the third heat storage operation respectively. The higher the flow rates, the more rapid the outlet temperature attains stability. This can be observed from the fluid-to-ground (F2G) heat transfer from Figure 5.1 b). Similarly, the outlet temperature of the vertical configuration increased gradually in less rapid manner than its counterparts. This behavior is attributed to the dynamics in the flow rates which must have reduced the thermal mass of the system. The fluid-to-ground heat transfer rate decreases or increases sharply during the temperature rise or fall for both configurations and this is observed due to the instant increase or decrease of the flow rates during heat storage or release. At points of natural release, the flow rate is zero hence the F2G heat transfer rate tends to zero while the behavior of ground temperature was monitored. Moreover, since the temperature sensors were left at the supply and return lines of the UTES, temperature measurement were still taken as water left in the pipe loses its heat energy. The fluid remaining at the return line (Tout_v and Tout_h) loses heat faster than the fluid left in the supply pipe. This variation is as a result of the insulation variations at the locations.

5.2.1.2 GTES Ground Temperatures

Figure 5.2 shows the temperature of the ground for both vertical (a) and horizontal (b) systems during heat storage and heat release at the center of the storage volume, TV_C_i and TH_C_i where i is the sensor number moving downwards. Generally, during the heat storage phases, the ground temperature in both systems gradually increased, with the horizontal configuration reaching peak temperature faster than the vertical configuration. This suggests that the horizontal configuration can be more effective for charging under the investigated conditions. Although the depth and input parameters, such as the inlet temperatures, may be the same, the varying length of pipe in the two storage volumes may be attributed to these results. As the depth increases, the ground temperature decreases, resulting in earlier peak temperatures.

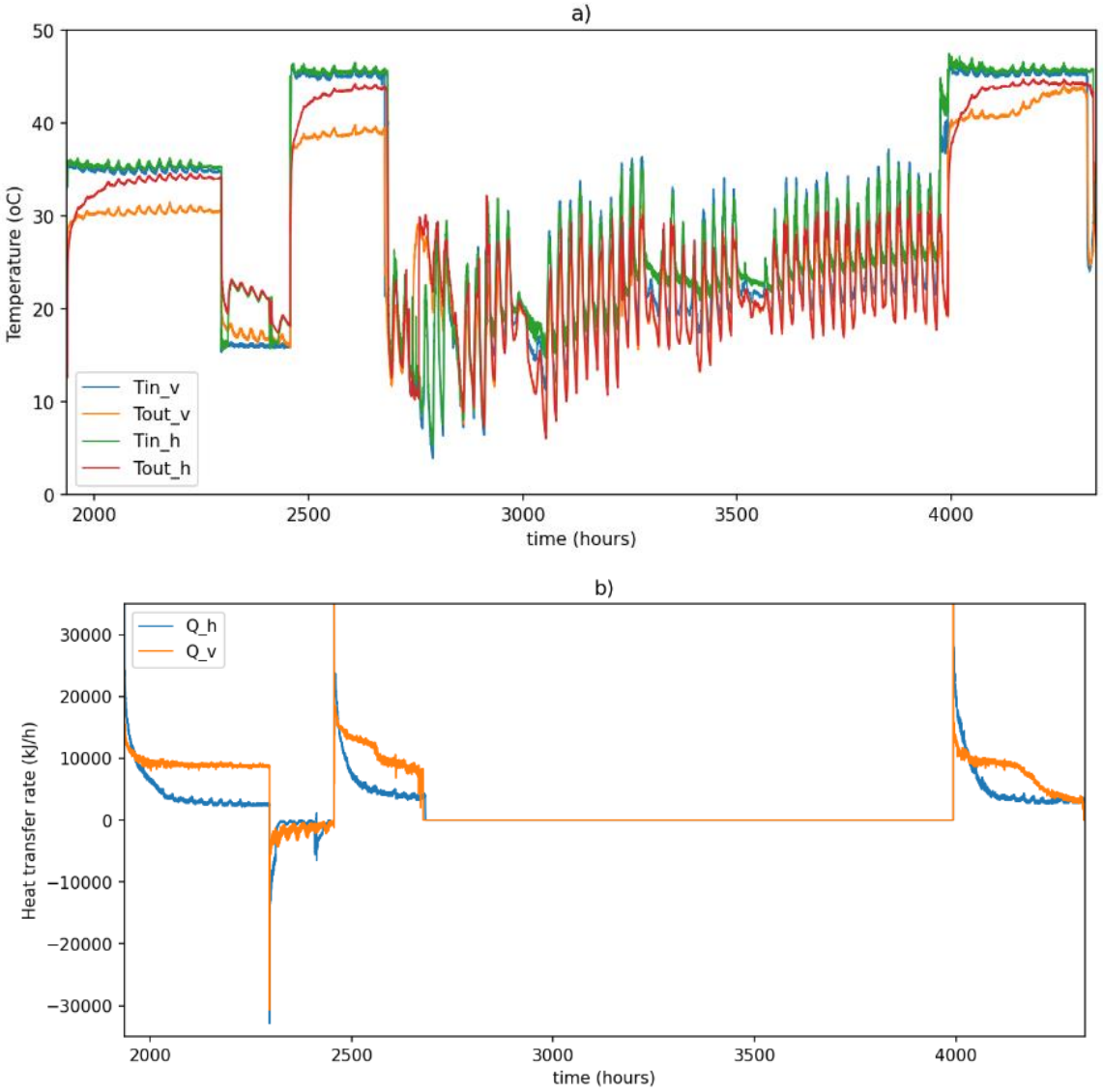

Figure 5.1: a) Water inlet and outlet temperature for both vertical and horizontal configuration, b) fluid-to-ground heat transfer rate

This behavior is observed chronologically in the vertical GTES system. However, the pattern differs for the horizontal GTES system, where the ground temperature decreases in the order of $TV\_C302, TV\_C304, TV\_C305, TV\_C303, TV\_C301$, and TV_C306 during the heat storage and TV_C301, TV_C302, TV_C304, TV_C303, TV_C305, and TV_C306 during heat dissipation. This result is as expected since the horizontal configuration has its pipes laid horizontally at the dept of 1.5m in a slinky pattern. Figure 5.3 presents a comparison of the average ground temperature, indicating that the horizontal GTES configuration outperforms the vertical configuration in terms of heat storage and release under slightly higher flow rates conditions. This is supported by the average charging and discharging rates of both systems,

as shown. The horizontal configuration charges and reaches peak temperature faster, while also discharging more slowly during heat release

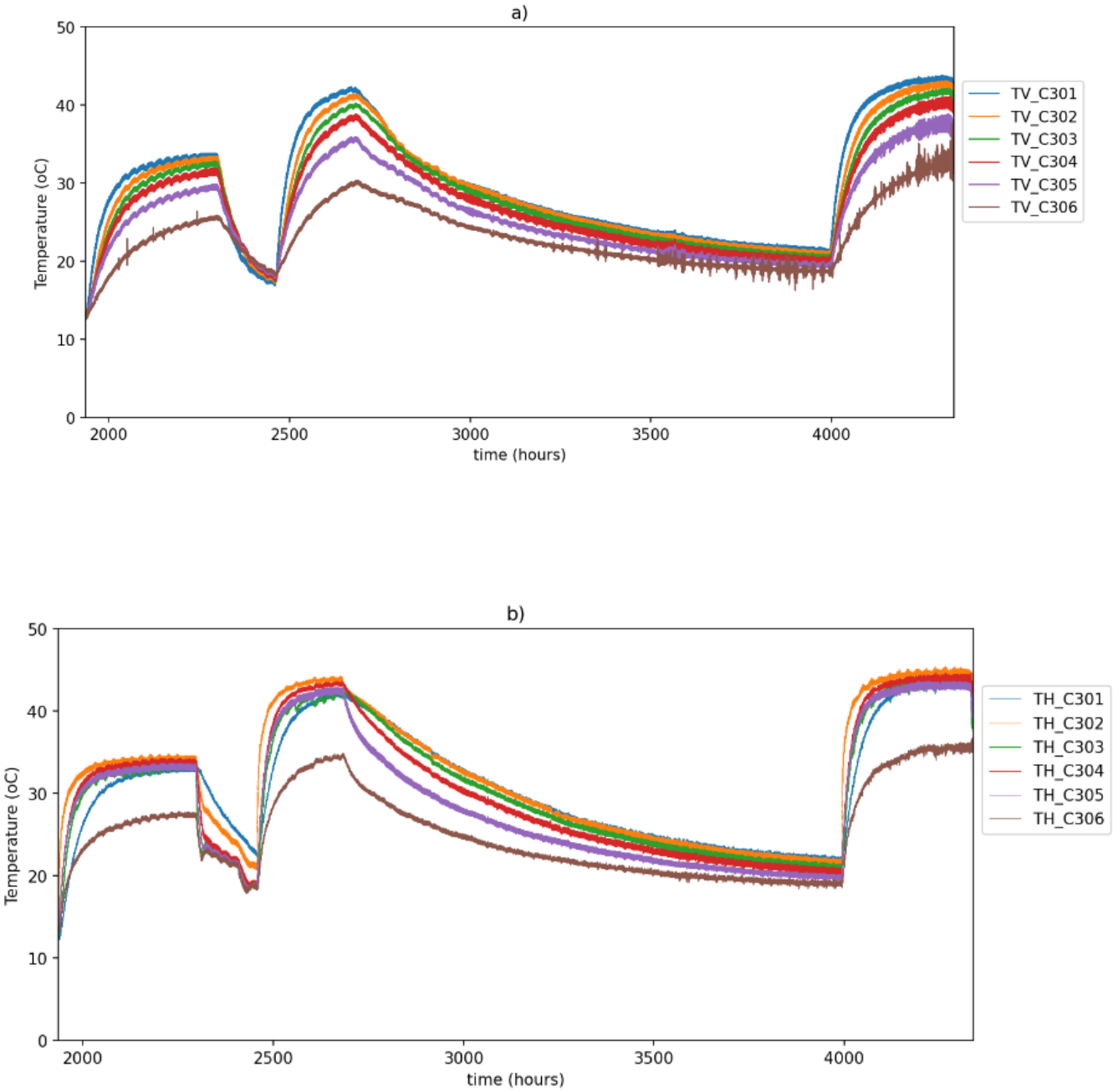

Figure 5.2: Measured ground temperatures: a) vertical and b) horizontal

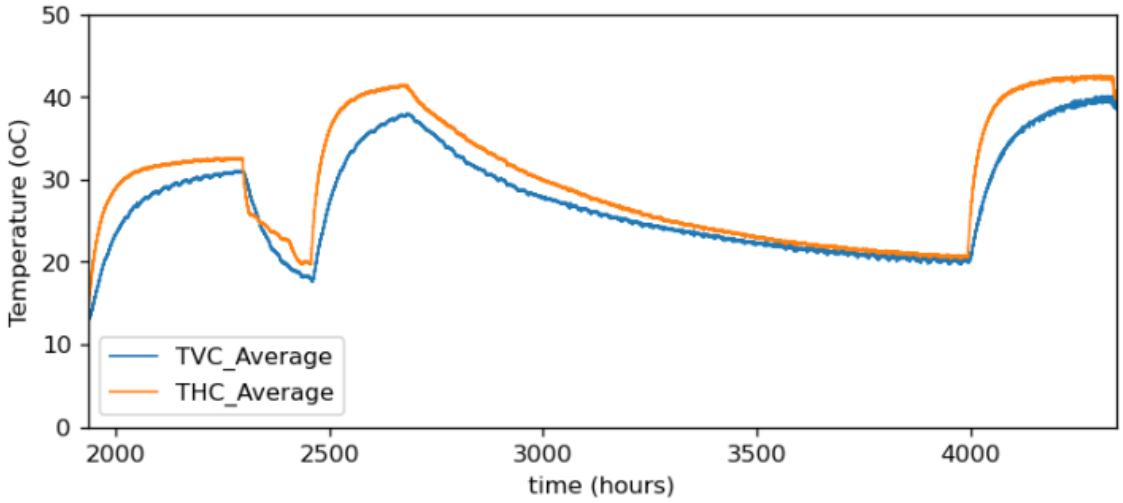

Figure 5.3: Average temperature at the center of the storage volume for horizontal and vertical configuration

5.2.1.3 External Ground Temperature

Sensors $TV_{o,i}$, $TH_{o,i}$, and $TC_{o,i}$ were installed vertically downward on the outer surface of the insulations to measure heat losses from the storage volumes, where i is the sensor number. Figure 5.4 illustrates the temperature variations observed. As the ground temperature inside the storage volumes increased during charging, both systems exhibited an increase in external temperature. Conversely, during discharging, the external temperature decreased in correlation with the decrease in the inside temperature of the storage volume. However, this temperature increment or decrement was more pronounced on the outer surface of the vertical GTES, specifically, at the topmost location, TV_o101. Similar observations were made at the center between the horizontal and vertical storage volumes but differs from the temperature variation immediately after the insulation installed for the horizontal GTES due to its piping configuration. Taking the average temperature variation by depth for the external temperature variations, the maximum temperature rises by 6, 4, and 5^{o}C for the first, second, and third heat storage phases respectively (Figure 5.5) for the insulation side of the vertical configuration. It then decreased by maximum values of 0.5 and 2^{o}C during the first and natural heat release phases respectively. It is worth noting that breakdown issues limited usable data to only four sensors for the horizontal system, as depicted in Figure 5.4 b). While heat loss from beneath the storage volume may contribute to this energy loss, it indicates the potential for employing more advanced insulating materials to mitigate significant heat losses.

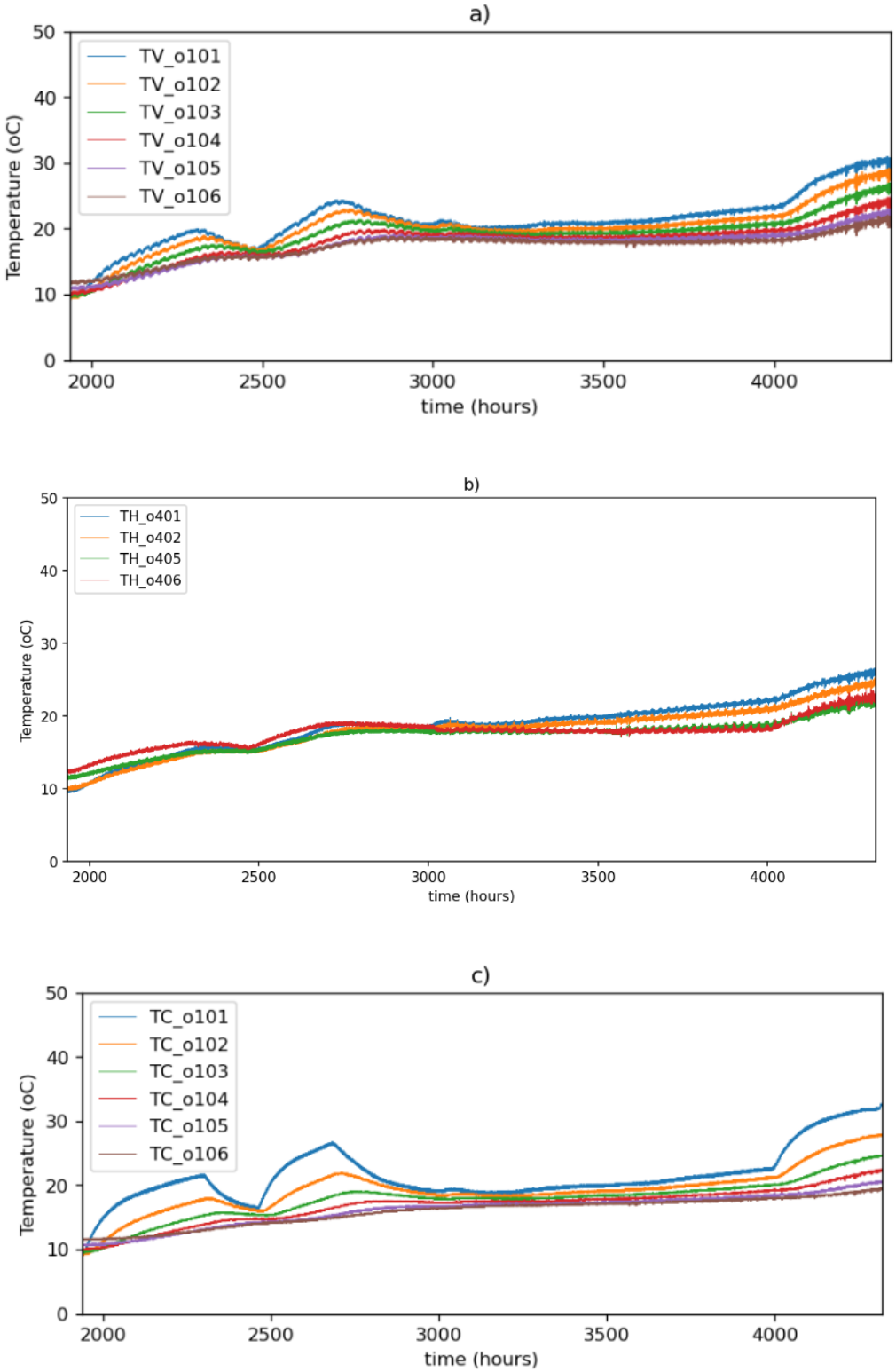

Figure 5.4: Temperature variation outside the insulated storage volume: a) vertical b) horizontal c) between vertical and horizontal

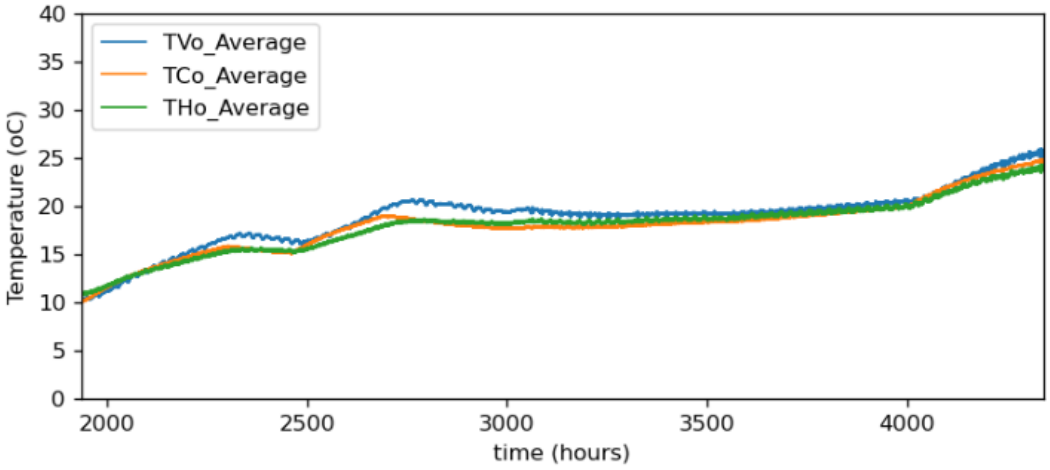

Figure 5.5: Average external ground temperature

5.2.2 Calibration of detailed TRNSYS model against the measured data

Measured data from the experimental study was utilized for calibrating the TRNSYS model. Data obtained from the experimental study performed between December 15 and December 31, 2021, was used for training. In this measured data, inlet fluid at a temperature 65 ^{o}C was supplied to the UTES for two weeks at varying flow rates. Similarly, the obtained data between April 2023 and March 2023 was used for model testing and evaluation. In the testing data, water at 35 ^{o}C was supplied to the ground for two weeks during heat storage, followed by one-week heat release, where water inlet temperature was supplied at 15 ^{o}C. For another two weeks, heat was stored with an inlet water temperature supplied at 45 ^{o}C. The training and testing results are demonstrated in Figure 5.6 and Table 5.1 shows the optimized parameters during training along with their lower and upper bounds with the initial guesses. The density component of soil for the vertical configuration is represented with the volumetric heat capacity of soil measured in kJ/m^3/K. Based on the opimising algorithm, the initial guesses continue to improve using iteration method until an optimal value is achieved. The developed model showed a good convergence with the measured data for the vertical and horizontal configuration. In the vertical configuration, the model converges gradually with the measured data during training as a result of the variation in the flow rates at the beginning of the experiment. Nonetheless, the training result indicated an RMSE of 0.87 ^{o}C with a corresponding CNRMSE of 1.38%. During the model performance evaluation (testing), the model exhibited an RMSE of 0.95 ^{o}C and a corresponding CVRMSE of 3.16%. In the horizontal configuration, a sharp peak was observed during the model testing before

convergence with the measured data. This is highly noticeable during the sharp bends in the flow lines where the flow is turbulent (fully developed). However, the RMSE of 0.49 ^{o}C corresponding to CVRMSE of 0.80% was calculated during the training process, and 0.99 ^{o}C corresponding to CVRMSE of 2.97% was obtained during the testing period. These results demonstrated that the detailed inverse grey-box (IGB) TRNSYS model for vertical and horizontal configurations developed in this study was successfully calibrated for application since a CVRMSE of below 20% is acceptable for application based on the ASHRAE standard according to Kim and Nam, (2020).

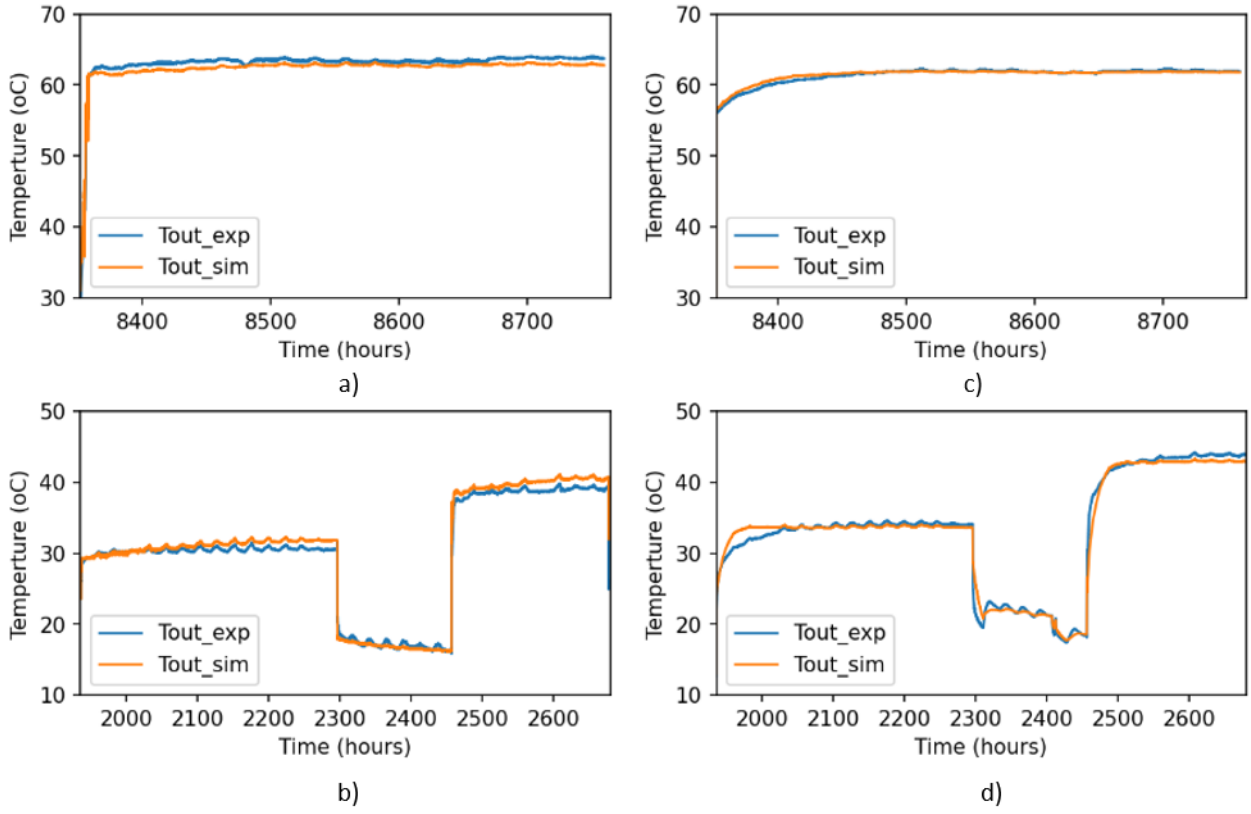

Figure 5.6: Training and testing data result for detailed TRNSYS model calibration a) vertical training, b) vertical testing, c) horizontal training, and d) horizontal testing.

Table 5.1: Optimised parameters showing the given lower and upper bounds as well as the initial guesses

Vertical				
Parameters	**Lower bound**	**Upper bound**	**Initial guess**	**Optimized value**
Pipe inside diameter (m)	-	-	0.024	0.024
Pipe outside diameter (m)	-	-	0.032	0.032
Total length of pipe (m)	-	-	56	56
Storage Volume (m^3)	-	-	22.17	22.17
Borehole depth (m)	-	-	2.5	2.5
Thermal Conductivity soil (kJ/hr·m·K)	4.6	20	4.8	15.975
Volumetric Heat Capacity of soil (kJ/m^3/K)	2000	6000	3600	5950.01
Thermal conductivity of grout (kJ/ hr·m·K)	2.5	12	4	2.5
Thermal conductivity of insulating material (kJ/ hr·m·K)	0.15	0.8	0.2	0.15
Thermal conductivity of pipe (kJ/ hr·m·K)	1.44	12	3.6	11.147
Horizontal				
Pipe inside diameter (m)	-	-	0.014	0.014
Pipe outside diameter (m)	-	-	0.018	0.018
Total length of pipe (m)	-	-	189	189
Borehole depth (m)	-	-	2.5	2.5
Thermal conductivity of pipe (kJ/ hr·m·K)	0.8	2.4	1.36	0.849
Specific heat of soil layer (kJ/kg·K)	0.4	32	0.84	23.6
Density of soil (kg/m^3)	1200	6000	2100	4616.18
Thermal conductivity of soil (kJ/ hr·m·K)	1.4	7.5	4.68	4.675
R-value of insulating material (h·m^2·K/kJ)	2.3148	2.3148	2.32	2.3148

5.2.3 Calibration of the IGB model against the measured data

Solving equations (4.1) to (4.4), the following inverse models, as given in equations (5.1) and (5.2) were developed, which are capable of predicting the UTES output. The terms y and z were added to account for some unmodeled dynamics in the system. Derivation of these equations are explained explicity in the appendix section of Eze et al., (2024b), a published paper from this work. It is important to note that all the parameters are well defined in the symbols and abbreviation section of the preliminary page, with the detailed derivation of the model given in the appendix section.

$$C_g \frac{dT_{out}}{dt} = \left(\frac{1}{R_{wg} + 2R_{wg}^2 \dot{m}_w c_{pw}} - \frac{0.5 - R_{wg}\dot{m}_w c_{pw}}{0.5R_{wg} + R_{wg}^2 \dot{m}_w c_{pw}} - \frac{0.5 - R_{wg}\dot{m}_w c_{pw}}{0.5R_{gs} + R_{gs}R_{wg}\dot{m}_w c_{pw}}\right) T_{in} + \left(\frac{1}{R_{wg} + 2R_{wg}^2 \dot{m}_w c_{pw}} - \frac{1}{R_{wg}} - \frac{1}{R_{gs}}\right) T_{out} + \left(\frac{1}{0.5R_{gs} + R_{gs}R_{wg}\dot{m}_w c_{pw}}\right) T_{soil} - C_{grout}\left(\frac{0.5 - R_{wg}\dot{m}_w c_{pw}}{0.5 + R_{wg}\dot{m}_w c_{pw}}\right)\frac{dT_{in}}{dt} \pm z \quad (5.1)$$

$$C_{soil} \frac{dT_{soil}}{dt} = \left(\frac{0.5 - R_{wg}\dot{m}_w c_{pw}}{R_{gs}}\right) T_{in} + \left(\frac{0.5 + R_{wg}\dot{m}_w c_{pw}}{R_{gs}}\right) T_{out} - \left(\frac{R_{as}R_{sG} + R_{gs}R_{sG} + R_{gs}R_{as}}{R_{gs}R_{as}R_{sG}}\right) T_{soil} + \left(\frac{1}{R_{as}}\right) T_a + \left(\frac{1}{R_{sG}}\right) T_G \pm y \quad (5.2)$$

The simplified inverse grey-box model, modeled in MATLAB as discussed in section 4.1.3, was calibrated against the measured data using the same training and testing data as in the previous section. The result obtained from the study is demonstrated in Figure 5.7, and the estimated parameters are shown in Table 5.2. In general, the IGB model exhibited a good convergence with the measured data during both training and evaluation periods of both configurations, but with some discrepancies. In the vertical configuration, little divergence was recorded during training, giving an RMSE of 0.45 ^{o}C that yielded a CVRMSE of 0.72%. In contrast, the horizontal configuration indicated higher divergence with the measured data during training, producing an RMSE of 0.67 ^{o}C, which corresponds to the CVRMSE of 1.09%.

The results of the training and testing errors for both configurations are summarized in Figure 5.9. For the vertical configuration, the CVRMSE increased from 0.72% during training to 7.91% during testing. This result indicates a poor performance where the model was unable to learn completely from the training data. It may also be attributed to the nature of the testing data compared with the training data, which ideally should follow a similar trend and be simulated under the same pulse. For the horizontal configuration, the CVRMSE increased from

1.1% during training to 3.17% during testing indicating a better performance than the vertical configuration.

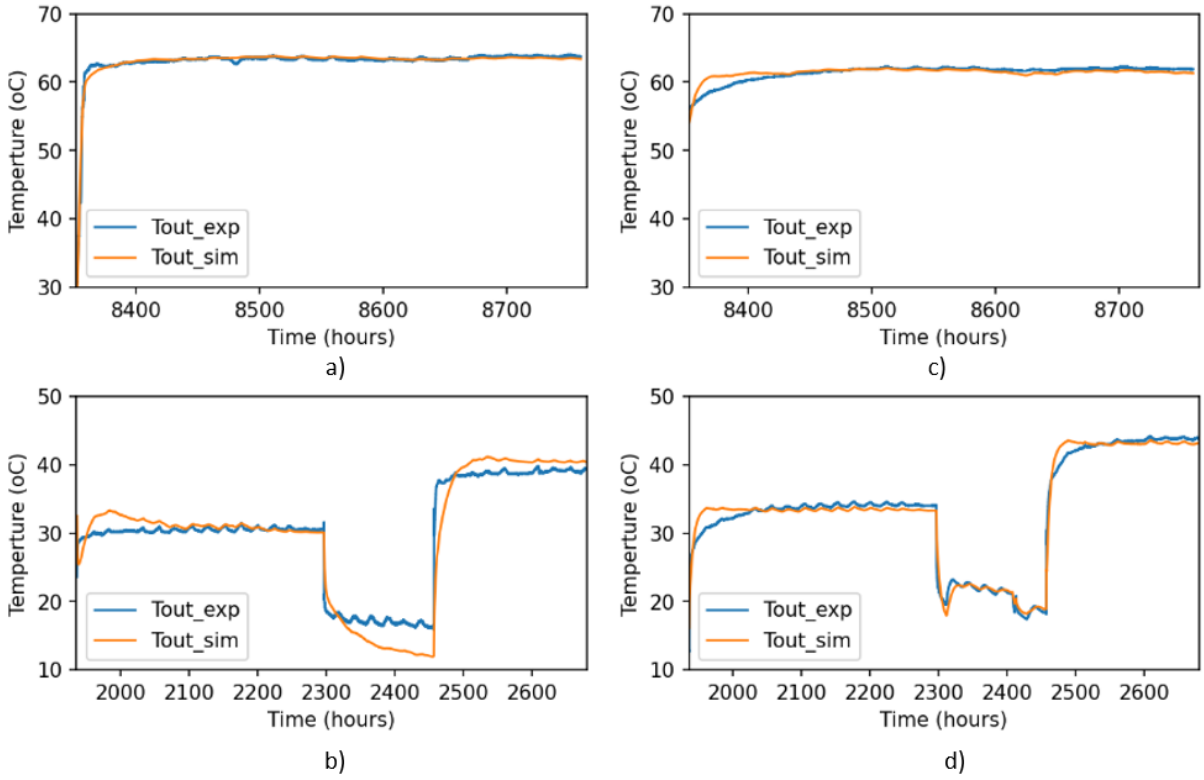

Figure 5.7: Training and testing data result for IGB model calibration a) vertical training, b) vertical testing, c) horizontal training, and d) horizontal testing.

5.2.4 Calibration of the IGB model with generated data from the detailed TRNSYS model

After the training and performance evaluation of the detailed TRNSYS model with measured data, the trained results were used to train the IGB model, while its testing result was utilized for its performance evaluation. As expected, the IGB model showcased similar results to the previous models, as shown in Figure 5.8. In general, the results indicated a CVRSME of 1.4% and 5.42 during training and testing, respectively, for the vertical configuration and a CVRMSE of 0.86% and 4.42% during training and testing, respectively, for the horizontal configuration.

Table 5.2: Optimised parameters showing the given lower and upper bounds as well as the initial guesses

Vertical Configuration				
Parameters	**initial value**	**final value**	**Initial guess**	**Estimated value**
Thermal conductivity of grout (kJ/hr·m·K)	2.5	12	4.6	2.515
Thermal conductivity of insulating material (kJ/ hr·m·K)	0.2	0.8	0.4	0.1501
Thermal conductivity of pipe (kJ/hr·m·K)	1.44	12	2.5	11.443
Thermal Conductivity soil (kJ/hr·m·K)	4.6	16	4.6	15.6
Density of grout (kg/m^3)	2000	10000	2500	7865
Density of soil (kg/m^3)	2000	10000	2500	7368.8
heat capacity grout (kJ/kg·K)	3.5	300	8.6	115.34
heat capacity soil (kJ/kg·K)	3.5	300	8.6	66.565
heat transfer coefficient of air (kJ/hr· m^2·K)	9	90	24.00	36
heat transfer coefficient of fluid (kJ/hr·m^2·K)	14700	32000	14000.00	19209
y	-inf	inf	0	0.0055975
z	-inf	inf	0	-0.0003351
Horizontal Configuration				
Thermal conductivity of grout (kJ/hr·m·K)	2.5	12	4.6	2.515
Thermal conductivity of insulating material (kJ/hr·m·K)	0.2	0.8	0.4	0.15
Thermal conductivity of pipe (kJ/hr·m·K)	1.44	12	2.5	11.44
Thermal Conductivity soil (kJ/hr·m·K)	4.6	16	4.6	15.6
Density of grout (kg/m^3)	2000	10000	2500	7944.6
Density of soil (kg/m^3)	2000	10000	2500	4283.3
heat capacity grout (kJ/kg·K)	3.5	300	8.6	102.62
heat capacity soil (kJ/kg·K)	3.5	300	8.6	76.449
heat transfer coefficient of air (kJ/hr·m^2·K)	9	90	24	36
heat transfer coefficient of fluid (kJ/ hr·m^2·K)	14700	32000	14000.00	19209
y	-inf	inf	0	0.0083306
z	-inf	inf	0	-0.002206

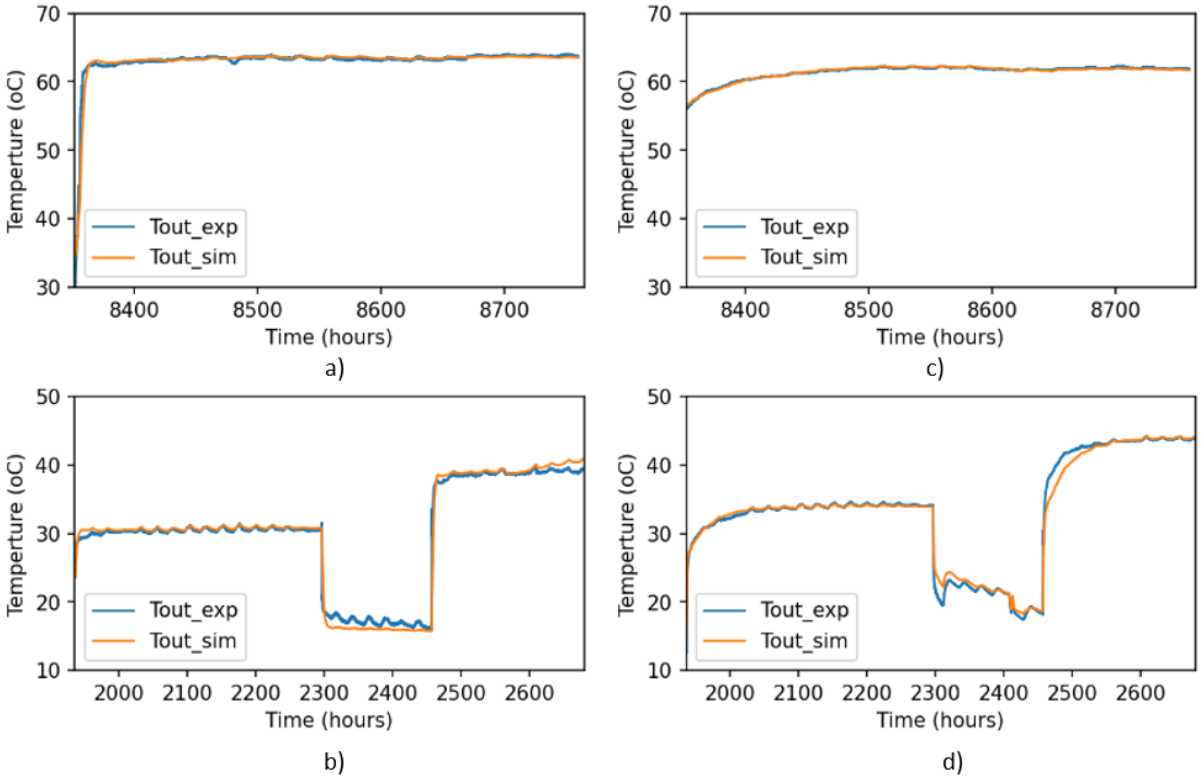

Figure 5.8: Training and testing data result for IGB model calibration with TRNSYS model a) vertical training, b) vertical testing, c) horizontal training, and d) horizontal testing

5.2.5 Performance comparison of all model training and testing

In this study, a detailed TRNSYS model of shallow UTES and an inverse grey-box model were developed. The detailed TRNSYS model was trained and tested with measured data from the conducted experiment. Similarly, the IGB model was trained and tested with the same measured data. In addition, the training and testing results from the detailed TRNSYS model calibrated with measured data were used to train and test the IGB model for performance evaluation. This section provides a comparison of these three calibration processes.

The CVRMSE of the three calibration processes is shown in Figure 5.9 for the vertical and horizontal configuration. In the vertical configuration, during the training process, the IGB model trained with experimental data outperformed the other, having a CVRMSE of 0.72%. seconded by the detailed TRNSYS model trained with the experimental data, which yielded a CVRMSE of 1.38%, and then the IGB model trained with the calibrated TRNSYS results, which yielded a CVMSE of 1.40%. These performances indicate that the inverse model learned from the experimental data at a rate faster than the rest. However, the reverse of this

performance is the case during testing, where its performance was lower than the rest, with the TRNYS model calibrated with the measured data outperforming its counterparts.

The evaluation of the horizontal configuration exhibited similar dynamics. However, in this case, with CVRMSE of 0.80% during training, followed by the inverse model trained with the results from the calibrated detailed TRNSYS model with CVRMSE of 0.86%, then the inverse model trained with the experimental data, with CVRMSE of 1.10%. During testing, the TRNSYS model calibrated with the experimental data yielded the best result with CVRMSE of 2.97%, followed by the inverse model trained with the experimental data, with CVRMSE of 3.17%, then the inverse model trained with the results from the calibrated detailed TRNSYS model with CVRMSE of 4.42%. Overall, these results suggest that while the detailed TRNSYS model performs well during training, the inverse model trained with experimental data performs better during testing, indicating the importance of using experimental data directly for model calibration and validation.

5.2.6 Performance analysis on the training and testing intervals

One of the limitations of the inverse black-box models such as the ANN is that its performance is limited due to the large range of data required for their training. In this section of the study, the impacts of training and testing intervals are tested to observe the performance of the model. To accomplish this, the calibrated TRNSYS model was used to generate data at given intervals and pulse. While about 12 weeks of data were generated for model training during a given period of the year, unseen data under the same pulse but at different times of the year was generated for testing purposes. Overall, 24 weeks of data were generated between January 1 and June 18 and were split into 12 weeks each for the training duration test (January 1 – March 25, 2023) and testing duration test (March 26 – June 18, 2023), as shown in Figure 5.10. The 12-week training data comprises three heat storage operations, each lasting for two weeks and followed immediately by two weeks of heat release. During the heat storage, inlet temperatures of 35 ^{o}C, 45 ^{o}C, and 55 ^{o}C were used for the first, second, and third heat storage operations, respectively as shown in Figure 5.10 a), while a constant temperature of 15 ^{o}C was supplied to the UTES during each heat release operation. The 12-week training data was divided into four training datasets (Training 1, 2, 3, and 4) as shown in Figure 5.10 a) for training during which the 12-week data for testing as shown in Figure 5.10 b) was fixed. Similarly, the 12-week testing data contains three heat storage operations, each lasting for two weeks and followed

immediately by two weeks of heat release. During the heat storage, inlet temperatures of 40 ^{o}C, 50 ^{o}C, and 60 ^{o}C were used for the first, second, and third heat storage operations, respectively as shown in Figure 5.10 b), while a constant temperature of 15 ^{o}C was supplied to the UTES during each heat release operation. The 12-week testing data was divided into four testing datasets (Testing 1, 2, 3, and 4) as shown in Figure 5.10 b) for testing during which the model was trained with the total of 12-week training data (fixed trained dataset) as shown in Figure 5.10 a). In general, the flow rates of 420 kg/h and 200 kg/h were used during the heat storage and heat release, respectively.

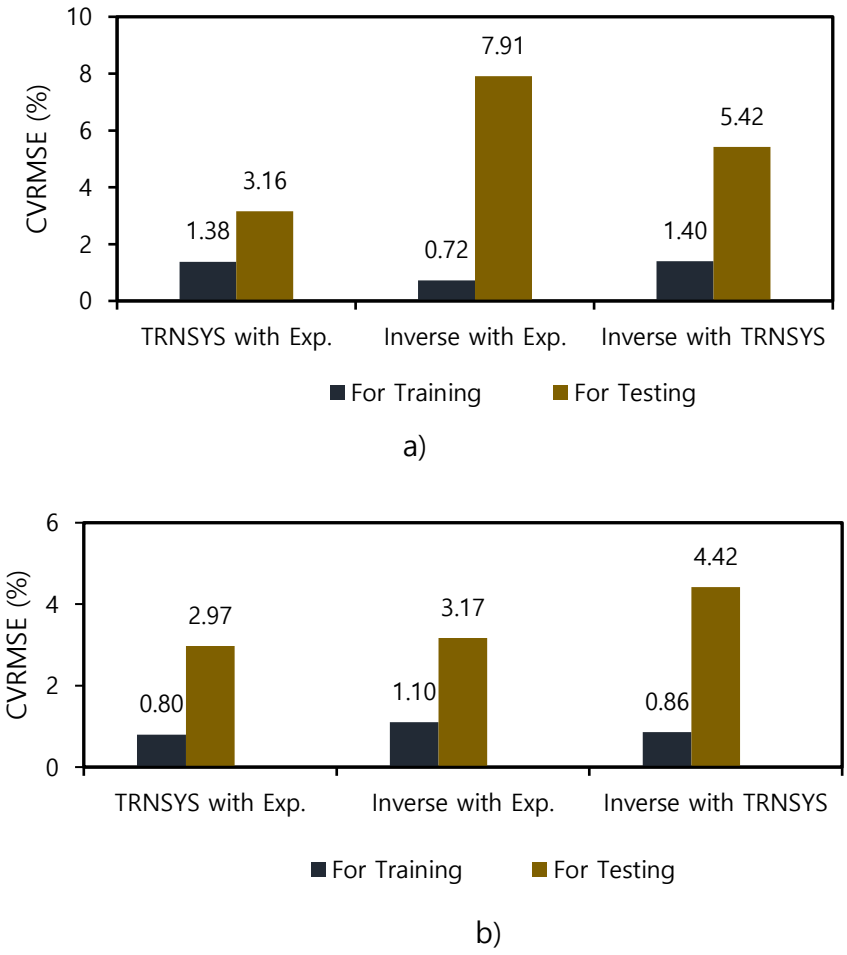

Figure 5.9: Comparison of the CVRMSE for training and testing results a) vertical and b) horizontal.

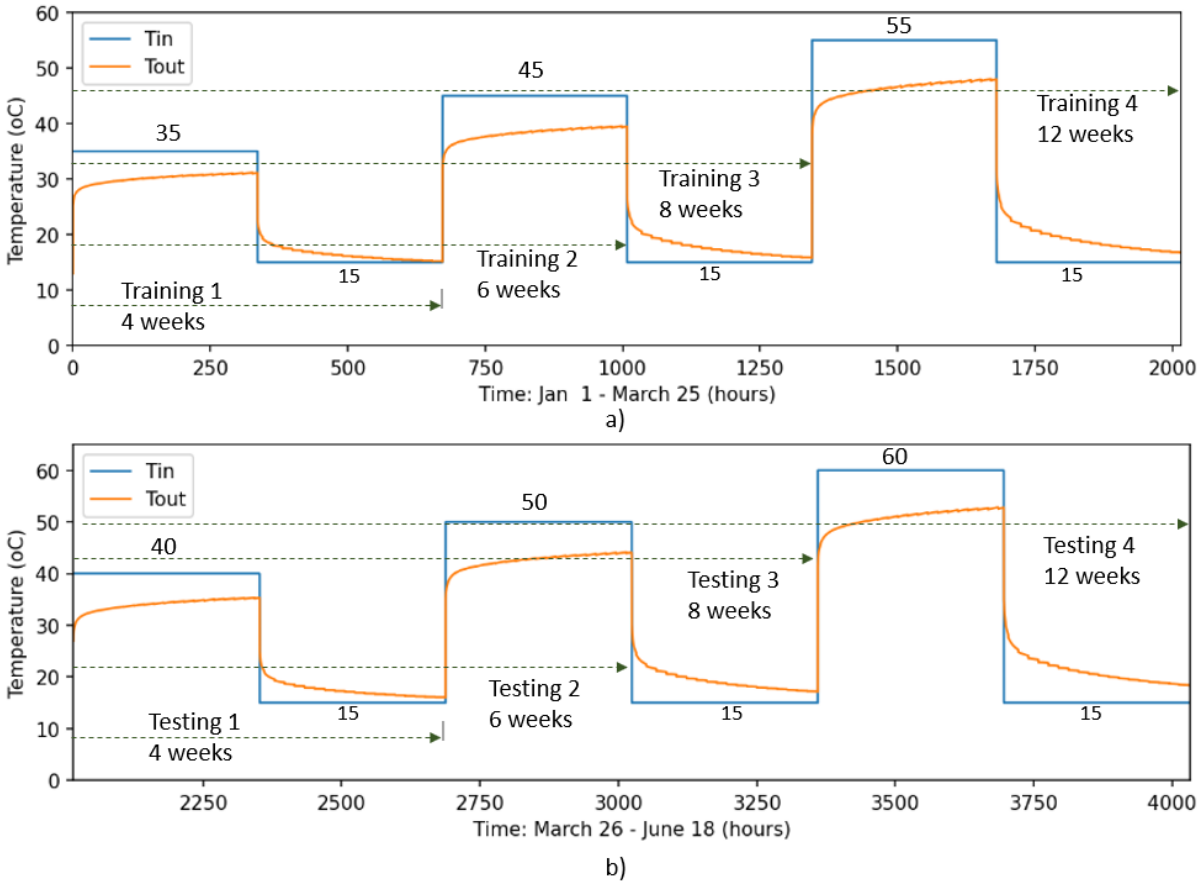

Figure 5.10: Generated data training and testing effects a) training data b) testing data.

5.2.6.1 Impacts of Training Duration

As shown in Figure 5.11, during the training duration test, the error increases linearly with the as the duration increases. For a clearer visualization, the CVRMSE for each training duration test was plotted as shown in Figure 5.12. Training the model with the 4 weeks, 6 weeks, 8 weeks, and 12 weeks datasets and testing with the 12-week fixed testing dataset yielded a CVRMSE of 7.0%, 5.5%, 4.8%, and 4.0%, respectively. As the training duration increases, the training error increases, whereas, for testing, the error decreases. It can be noticed in Figure 5.12 that the training and testing errors recorded approach convergence, meaning that if this training period is extended to some point, convergence might be attained. This will be explored further during the long-term performance test.

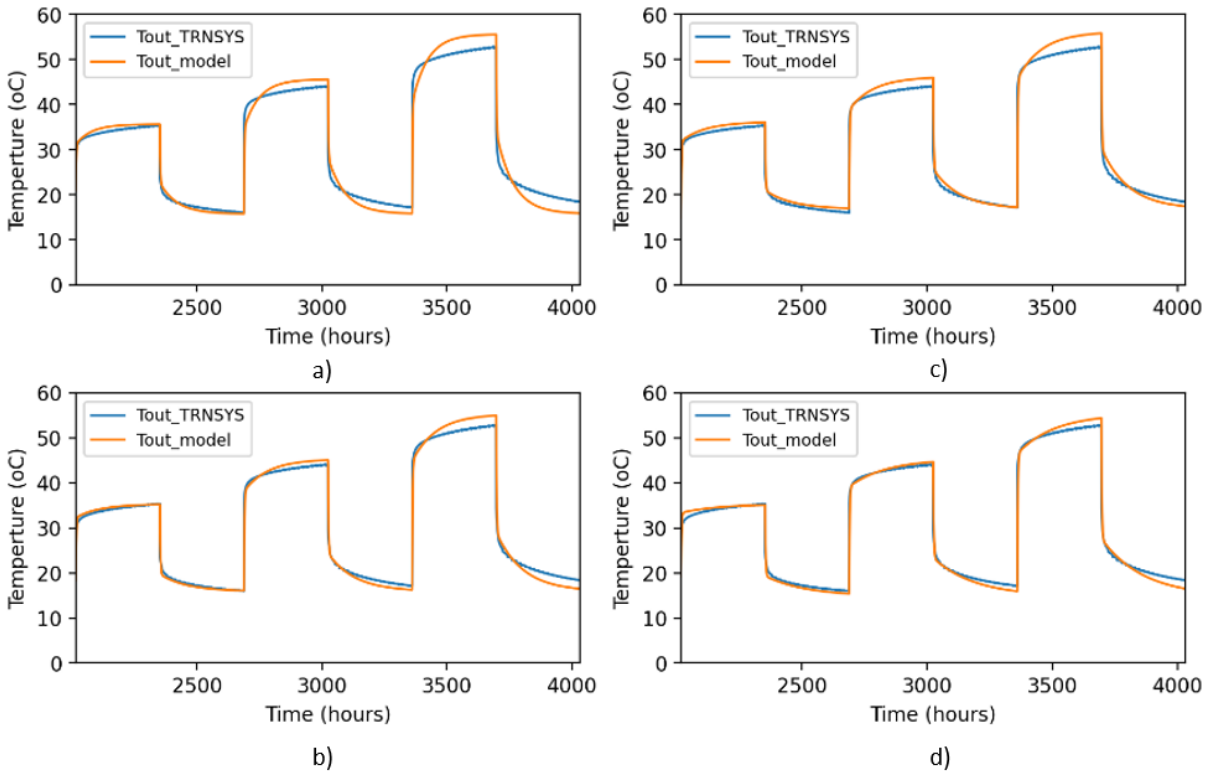

Figure 5.11: Impact of training duration on the performance of the IGB model.

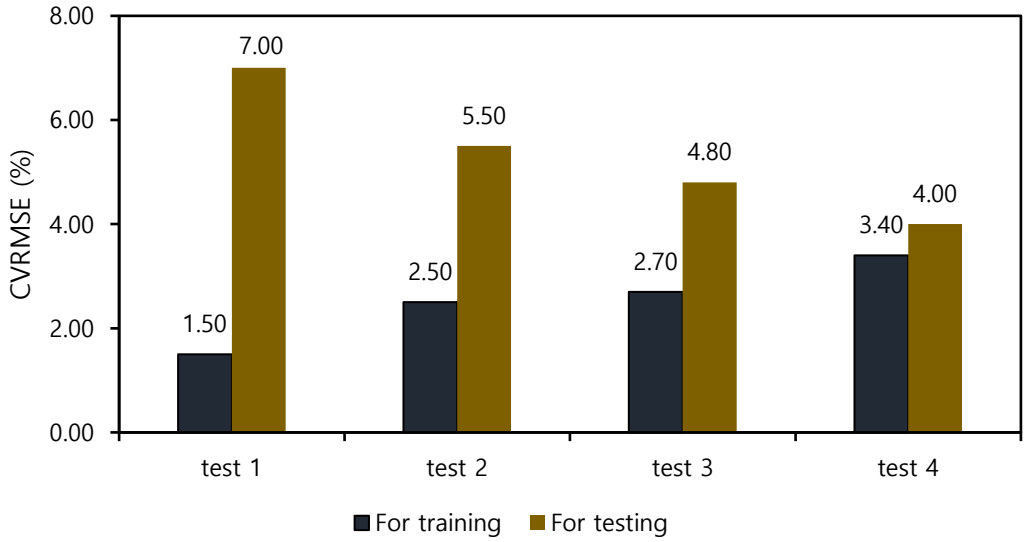

Figure 5.12: CVRMSE variation during the training duration test.

5.2.6.2 Impacts of Testing Duration

The testing duration test results are shown in Figure 5.13 and Figure 5.14. Similarly, the tests 1 to 4 performed yielded a CVRMSE of 3.1%, 3.0%, 4.4%, and 4.0%, respectively. In comparison with the training error of 3.4% which remained constant since the training duration was fixed throughout the testing periods that were changing. The result shows that the model is also sensitive to testing duration and implies that the model performs better when the training duration is large enough and possibly higher than the testing data. However, this is not a recommended approach since using a large range of data for short-term performance prediction results in an imbalance between the computational resources and performance prediction.

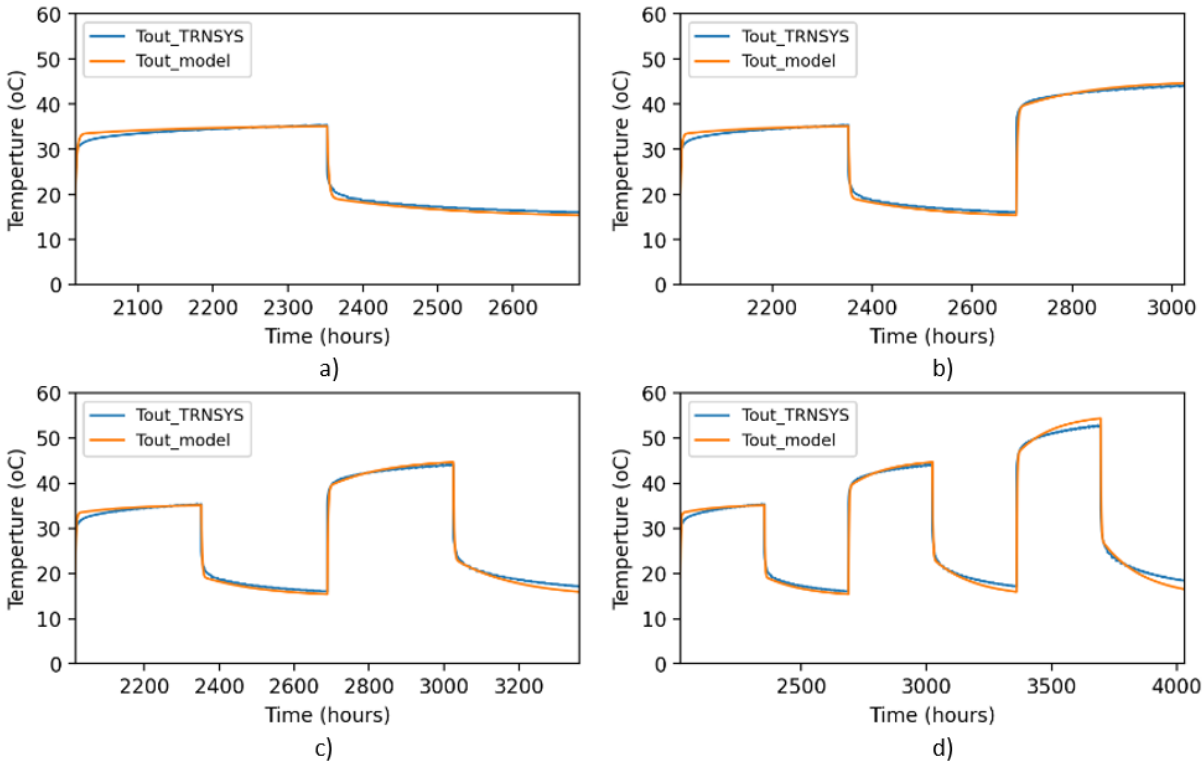

Figure 5.13: Impact of testing duration on the performance of the IGB model.

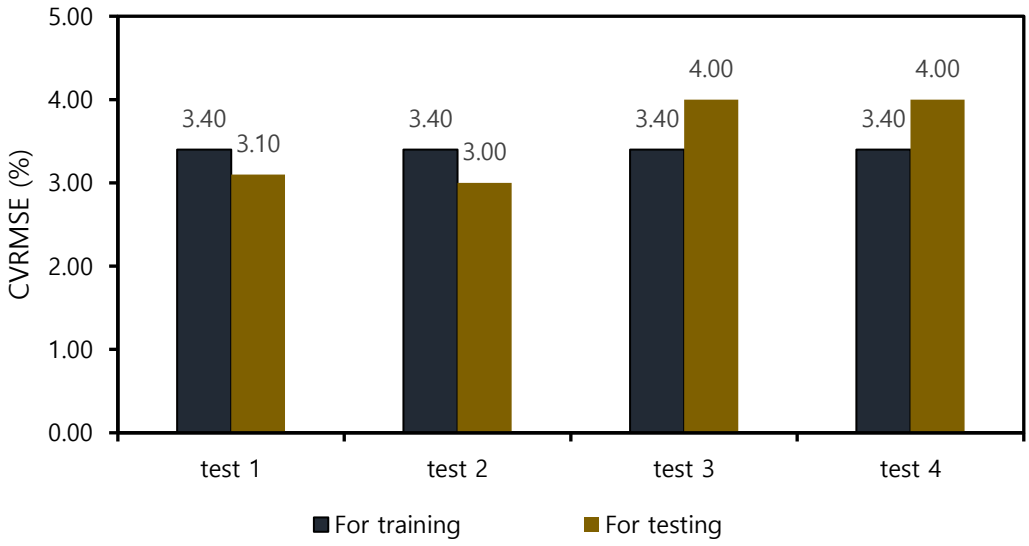

Figure 5.14: Figure 5.12: CVRMSE variation during the testing duration test.

5.2.7 Long-term Performance Evaluation of the IGB Model

To evaluate the model's performance over a long period, the 12-week training data was used to train the model, and performance evaluation was done for 10 years using TRNSYS-generated data over an hourly timestep. The data comprises 24 weeks with variations in the inlet temperature chosen to simulate more dynamic or unsteady state in the system behaviour which the test model must mimic for validation. In the first 12 weeks, inlet temperatures of 40, 50, and 60 ^{o}C were used for the first, second, and third heat storage, respectively, which were each performed over two weeks, followed each by a two-week heat release where 15 ^{o}C temperature was supplied to the model. The last 12 weeks comprise inlet temperatures of 35, 45, and 55 ^{o}C, each with corresponding two weeks heat release with inlet temperature of 15 ^{o}C. To maintain consistency, flow rates of 420 kg/h and 200 kg/h was used during each heat storage and heat release, respectively. On the completion of the simulation over the 24 weeks, the cycle repeats until 10 years are completed over an hour timestep.

In Figure 5.15 the result of this long-term performance evaluation was shown. The evaluation indicated a good agreement with the long-term test, producing a CVMSE of 5.2%, which is within the acceptable accuracy. Additionally, the 24-week training data was generated from the calibrated TRNSYS model. This data was split into 4, 8, 12, 16, 20, and 24 weeks for training while testing with the 10 years generated data. The essence of this performance evaluation is to identify the maximum training duration that would yield the optimum

performance over the long term, and the result is shown in Figure 5.16. As expected, during the training, the error increases with increased training duration. However, during testing over the 10 years, the error decreased as the training duration increased, indicating an improved performance, although, even with the reduced training duration, the error remained within acceptable accuracy. An important observation on the error convergence was made after 20 weeks of training and testing over a long period. This indicated a point of convergence where further increment in the training duration does not improve the system performance significantly, as shown in Figure 5.16. This observation breaks the limitation that other machine learning models have in requiring a large range of training data for making an accurate performance prediction over a long period of time, thereby balancing computational resources and performance requirements. Although the long-term predictive performance obtained in this study is within the acceptable accuracy, updating the model's learning outcomes with recent data at appropriate intervals may also be applicable, which could address cases where long-term prediction performance accuracy is low.

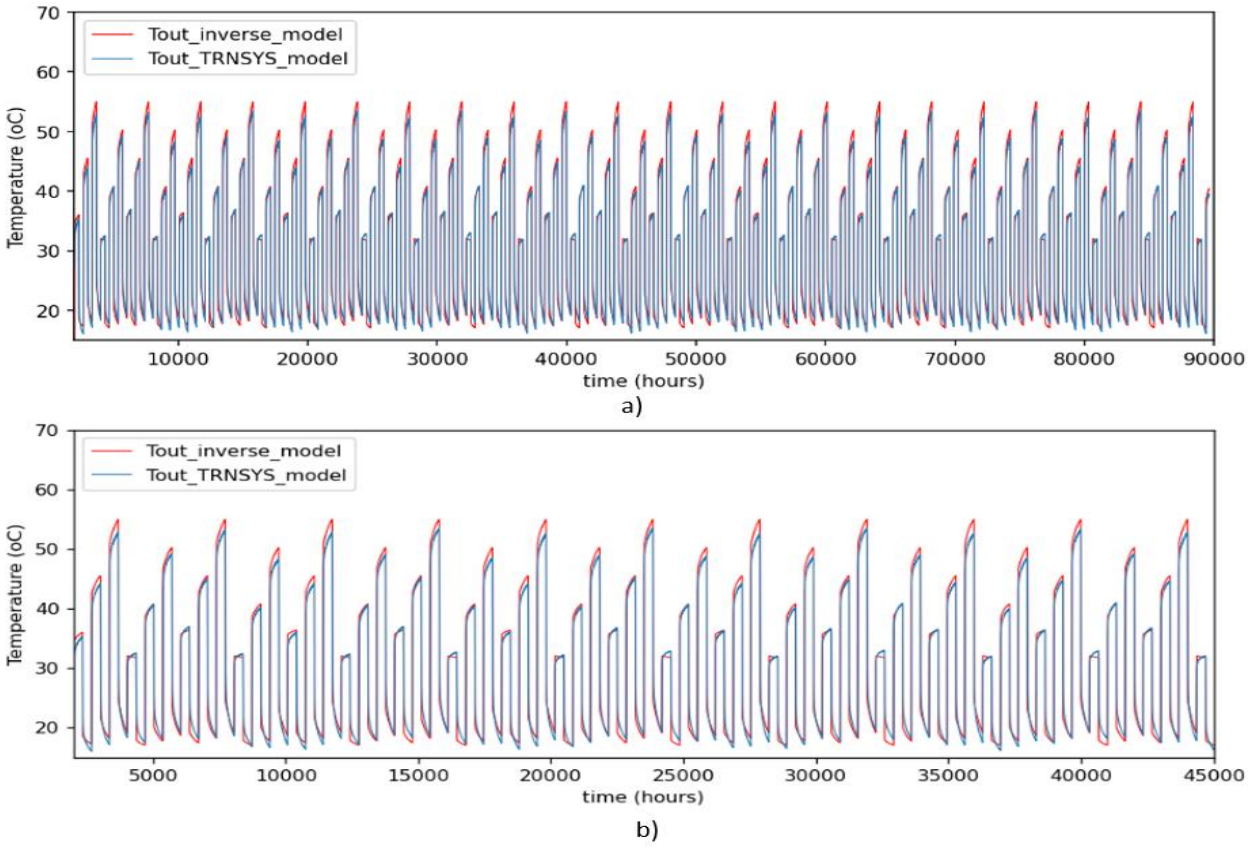

Figure 5.15: Long-term Performance evaluation of the IGB model a) 10 years comparison b) 5 years zoomed result.

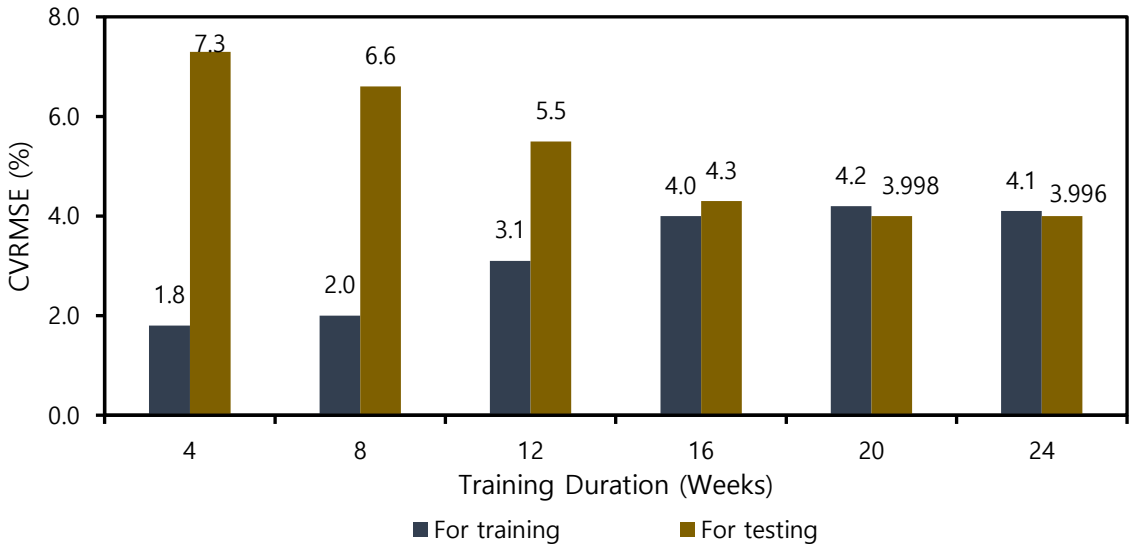

Figure 5.16: Effects of training duration on long-term performance.

5.2.8 Comparison with Other Models in Literature

The developed IGB model was compared with other models in previous studies, as demonstrated in Table 5.3 (Başer and McCartney, 2020; Lamarche, 2019; Maestre et al., 2015, 2013; Najib et al., 2019; Nam et al., 2008; Naranjo-Mendoza et al., 2018). It was observed that several factors for validating the models are missing in previous works. For instance, most of the previous studies utilized data from white-box models such as the FEFLOW, ANSYS, COMSOL, etc., for validation of the models instead of the data from the actual field experiment. Similarly, an insulation around the system's storage volume was missing, which implies a significant amount of heat loss from the systems. The limitation of using a large range of data for long-term model performance prediction has been a limitation in the wide application of AI models such as the ANN. However, in previous works sensitivity analysis of the training duration for making long-term performance prediction was lacking. These issues were solved in the present, where an experiment on the actual shallow UTES systems was conducted, and the data was data used to train and validate the developed models. Additionally, in developing the IGB models, an insulation on the top and side of the storage volume was considered which has not been done so far in previous studies. Finally based on the sensitivity anlysis that was carried out in the present work, a convergence point of 20 weeks was obtained for making acceptable prediction over a long period of time.

Table 5.3: Recap of selected models in previous studies for comparison

Authors	Model Type	Method of evaluation	RMSE (°C)	CVRMSE (%)
Present Study (Vertical Configuration)	Inverse grey-box Model	Calibration against measured data from field experiment	Detailed TRNSYS = 0.95 IGB Model = 1.33	3.16 7.91
Present Study (Horizontal Configuration)	Inverse grey-box Model	Calibration against measured data from field experiment	Detailed TRNSYS = 0.99 IGB Model = 0.45	2.97 3.17
Kim and Nam, (2020b)	Numerical Model	Calibration against FEFFLOW model	0.13	1.33
Maestre et al., (2013b)	R-C model	Calibrated against ANSYS model	0.41	Not calculated
Maestre et al., 2015	R_C model	Calibrated against ANSYS model	0.41	Not calculated
Naranjo-Mendoza et. al., (2018)	Analytical and Numerical models	Compared with experimental data	Range: 0.1 – 11.56	NRMSE: Range 1.82 – 163.68
Baser and McCarthy, (2020a)	Numerical Modeling	Calibration and validation with experimental data	Graphical comparison	Graphical comparison
Lamarche, (2019)	Modified finite line source	Analytical vs COMSOL model	Graphical comparison	Graphical comparison
Najib et. al., (2019)	Capacitance Resistance Model (CaRM) vs CFD	Calibrated with ANSYS CFD model	0.29	Not calculated
Miao et al, (2017)	Grey-box and white box model	Calibrated with field data	Grey-box = 0.96 White-box = 0.78	Not calculated

5.3 System Modeling and Simulation Results

In this study, the P2HC concept described in Figure 4.9 was applied and a novel system configuration demonstrated in Figure 4.10 b) was modeled and simulated. The successful application of excess solar power generated by the installed solar PV for the inter-seasonal operation of a dual-source heat pump was targeted. This novel configuration and its control strategy were evaluated using different case studies as described in section 4.2.3, and the case study building is a typical public school building described in section 4.2.3.1.

The power profile of the case study building in kW measured over a one-year period is shown in Figure 5.17. During the winter season, the load demand is very high due to the high heating demand, and the PV power tends to be low as a result of the low availability of solar energy. During this season, the grid is utilized to meet the remaining energy requirement of the building. Similarly, in the summer season, the energy demand is high due to the high cooling

demand. However, the PV power tends to be sufficient for meeting the load demand due to the adequate availability of solar energy. In spring and autumn, the opposite is the case. During these seasons, little or no heating and cooling load is required, and sufficient solar energy exists. This led to the existence of surplus power generated from the PV system, as demonstrated in Figure 5.17. Therefore, a P2HC strategy is required for the utilization of this excess electricity. In general, the energy flow in the building is demonstrated in Figure 5.18. The total PV power generated per year is utilized for the operation of the heat pumps for heating and cooling purposes as well as performing the P2HC operation. Additionally, other basic electricity demands are also met by solar PV power, as depicted. In the following sections, the performance of each study case is evaluated and described.

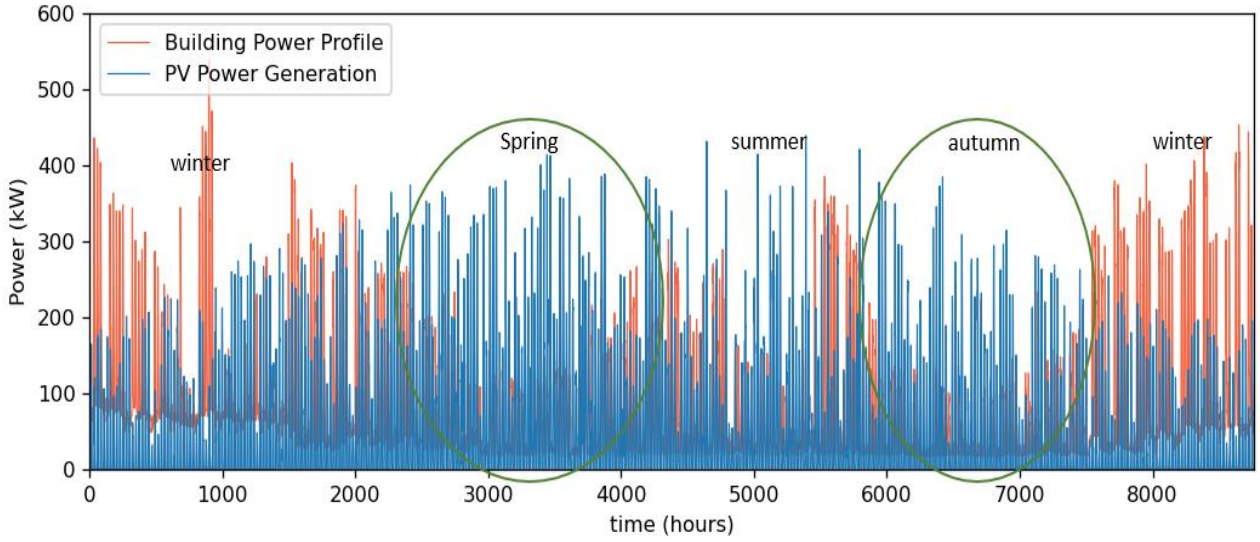

Figure 5.17: PV power generation versus building power profile over a year period.

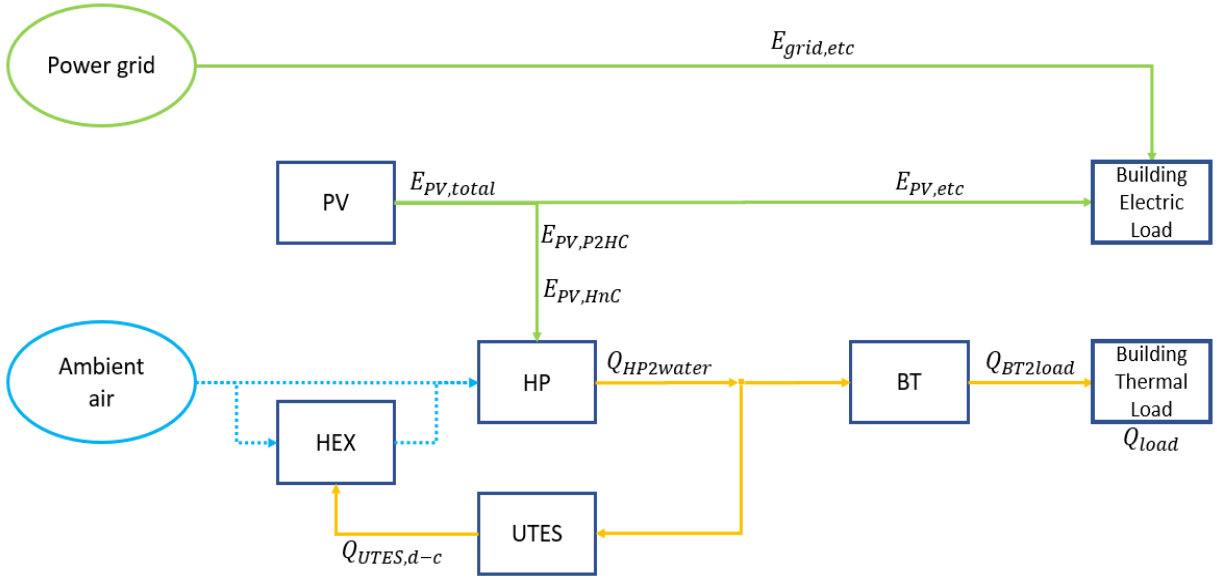

Figure 5.18: Demonstration of energy flow for the building energy requirement.

5.3.1 Performance Evaluation of Case 1

5.3.1.1 Performance evaluation of shallow UTES for Case 1

This work utilized a simple control method to develop a dual heat pump where air and water are utilized on the heat pump source side. It is developed in such a way that the heat pump is used for the provision of heating and cooling requirements of the intended building as well as for charging and discharging the installed UTES system. In general, the heat pump is operated with the excess electricity generated by solar PV hence the term solar-assisted heat pump (SAHP). In Figure 5.19, the temperature variations of the installed UTES for study case 1 are shown. During the heating and cooling seasons in winter and summer, the stored heat in the UTES is extracted and utilized for space conditioning. As can be observed in Figure 5.19 a), the difference between the inlet and outlet temperature is small due to high flow rates. During the spring season, the excess electricity was used to operate the heat pump, which in turn produces thermal energy at a low temperature of about 2℃ through the water-load side. The low temperature working fluid (water) was injected into the ground, thereby charging the ground to a lowered temperature. In the autumn season, the heat pump injects water at a temperature of about 50℃ into the ground, raising the ground temperature. Consequently, the ground temperature is raised from lowered to about 5℃ from about 17℃ in the spring season and was raised to a temperature of about 34℃ from approximately 17℃ during the autumn

season, as shown in Figure 5.19 b). In Figure 5.19 b), the average temperature variation of the ground storage volume is shown. Additionally, the average temperature at the center and edge of the storage volume was demonstrated. It shows that the average temperature of the entire storage volume was charged to a temperature of about 7℃ during the spring and 25℃ during the autumn P2H operation. The average temperature at the center and edge of the storage volume demonstrated the same pattern with little deviation, as depicted in Figure 5.19 b). In this case study scenario, the UTES thermal efficiency, η_{UTES} of 24% was obtained using equation (4.31).

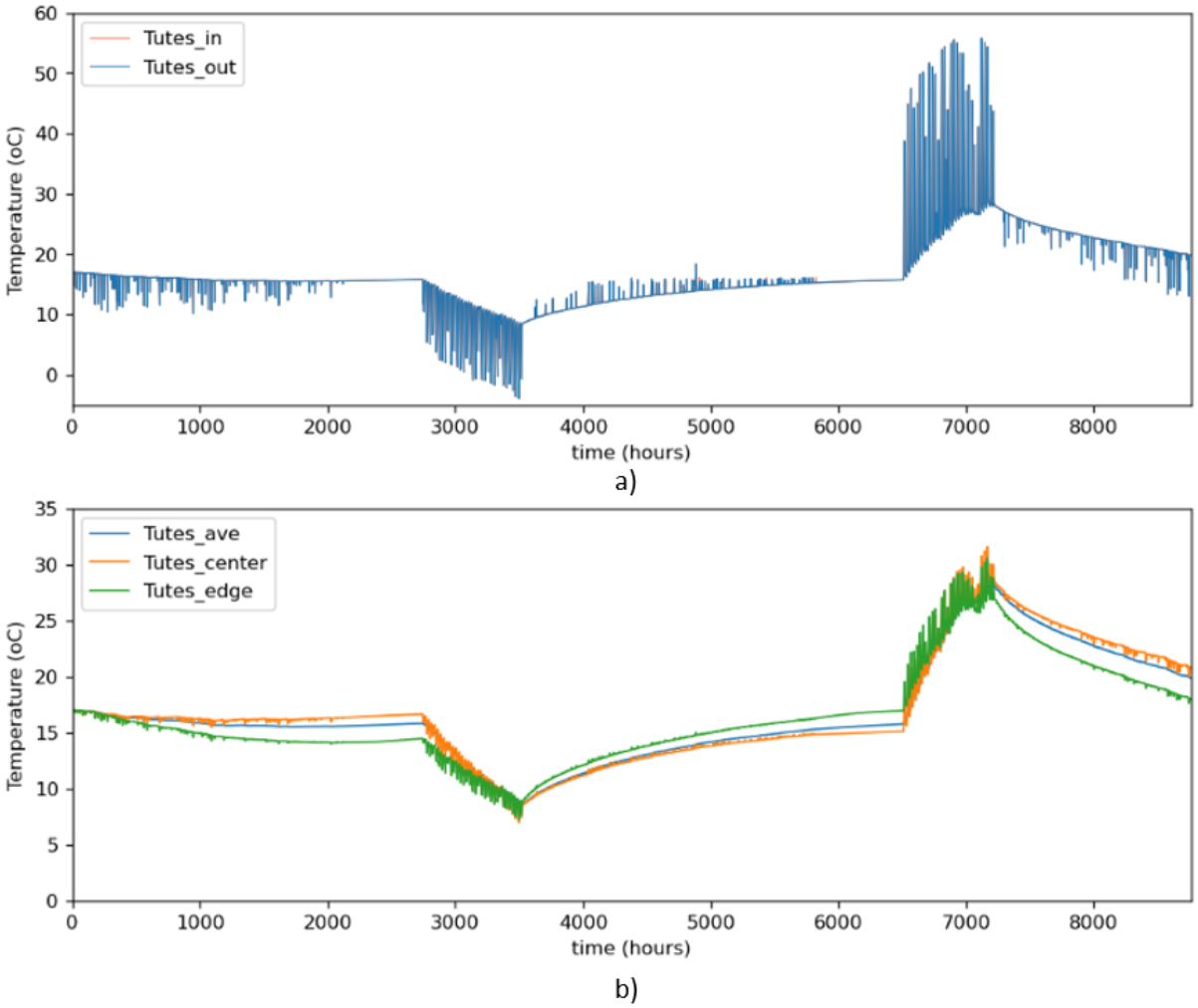

Figure 5.19: Temperature variation sUTES for CASE 1 a) Inlet and outlet temperatures b) Ground temperatures.

5.3.1.2 Evaluation of Heat Pump Performance for Case 1

The research utilized the air-source HP dual functions, which are the air-load function for heating and cooling and the water-load function for charging the shallow UTES with excess energy from the PV subsystem. In the normal operation of an ASAL heat pump, the ambient air conditions are supplied to the heat pump source side. This limits the performance of the heat pump, especially in severe climate conditions such as in Korea. When the heat pump operates in its default condition, air as low as -15℃ is supplied to the heat pump during the winter season, as shown in Figure 5.20 a). Similarly, air temperature of up to 35℃ is supplied to the heat pump source side during summer cooling. However, in the test case, the temperature of the air supplied to the heat pump was raised from -15℃ to about 17℃ in winter and lowered from 35℃ to about 13℃ during summer, thanks to the configuration and its control technique to successfully implement the P2HC strategy. In Figure 5.21, one week simulation each during preheating and precooling is shown for a clearer visualization. As a result of this enhancement, the outlet temperature of the heat pump which is supplied to the building was improved in the test case, particularly during the winter season as shown in Figure 5.20 b).

5.3.1.2.1 Building Zone Temperature Variation

As a result of the zone temperature control, the zome was maintained at a temperature between 18℃ and 22℃ during the heating and cooling seasons, as shown in Figure 5.22. In comparison with the ambient temperature, the conventional case and test case maintained the zone temperature as required, raising and lowering the temperature of the zone during winter heating and summer cooling periods, respectively. This zone temperature is returned to the heat pump load side return temperature to complete the load side loop.

5.3.1.2.2 Monthly Electricity Consumption of Heat Pump for Case 1

The improvement in the heat pump performance due to the P2HC strategy employed in the study is partly as a result of the electricity consumption which was improved significantly over the months of the year as demonstrated in Figure 5.23. Throughout the months of winter (November to March), the monthly energy consumption of the heat pump was higher in the conventional case than in the test case. This is similar in the months of summer (June to August). Additionally, significant surplus electricity was utilized during P2C operation in the months of spring (April and May) and in the months of autumn (September and October). This

result demonstrates the successful implementation of the P2HC strategy for inter-seasonal consumption of solar energy in the case study building.

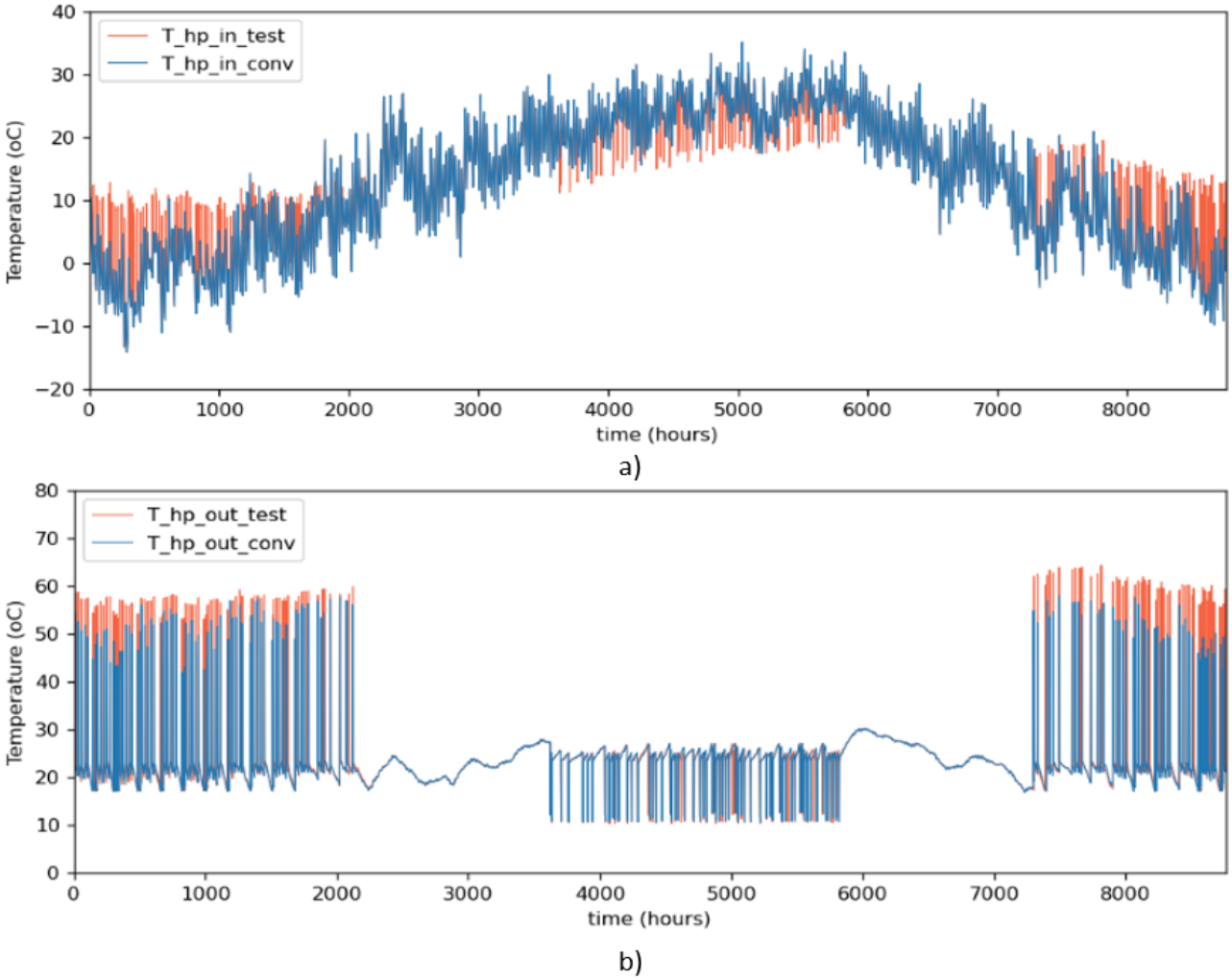

Figure 5.20: Heat pump temperature comparison of conventional and test cases for Case 1 a) inlet temperatures for case 1 b) outlet temperatures.

5.3.1.2.3 Seasonal Coefficient of Performance (SCOP) of Case 1

The configuration in the study, along with its control strategy, contributed to a significant improvement in the heat pump performance apart from utilizing the surplus electricity generated from the solar PV system. The seasonal coefficient of performance (SCOP) was improved from 5.0 in the conventional case to 6.5 in the test case during the winter heating season, increasing the SCOP by 23%. These results are demonstrated in Figure 5.24. Similarly, during the summer cooling, the SCOP of 4.2 was obtained from the test case, contrary to the

conventional case, where an SCOP of 3.8 was obtained, indicating an increase in the SCOP by 10%.

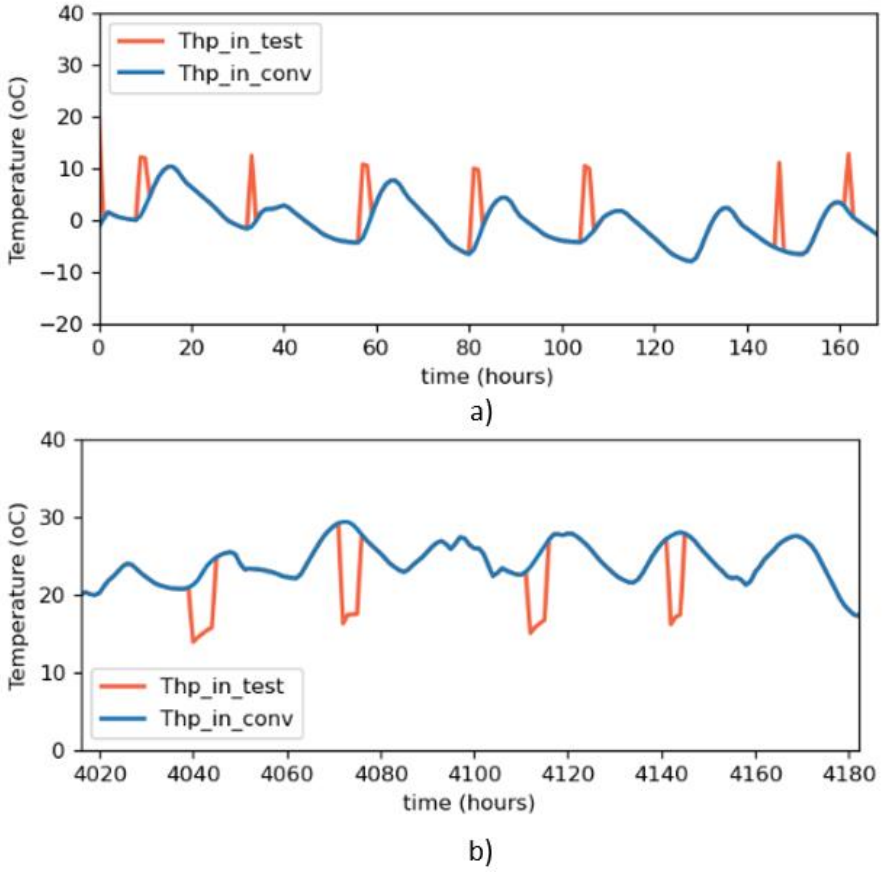

Figure 5.21: one-week view of inlet air temperature to the source side of heat pump for conventional and test cases a) preheating operation in space heating mode and b) precooling operation in space cooling model.

5.3.1.2.4 P2HC Efficiency, Percentage of Energy Savings, SCR, and SEUR for Case 1

Equations (4.27) and (4.29) were used to obtain the P2HC efficiency and the percentage energy saving of 16.3% and 18%, respectively, for the test case scenario. Additionally, the SCR of 73% was obtained for the test case using equation (4.25), in contrast to 64% obtained in the conventional case. Furthermore, a SEUR of 31% was obtained for the test case using equations (4.26). This result indicates that about 73% of the power generated by the solar PV system per annually was consumed on-site while 31% of the excess electricity generated per year was successfully converted to heat (P2HC operation) during spring and autumn seasons and

extracted for heating and cooling operation during winter and summer seasons. In general, the summary result for the Case 1 is shown in Table 5.4

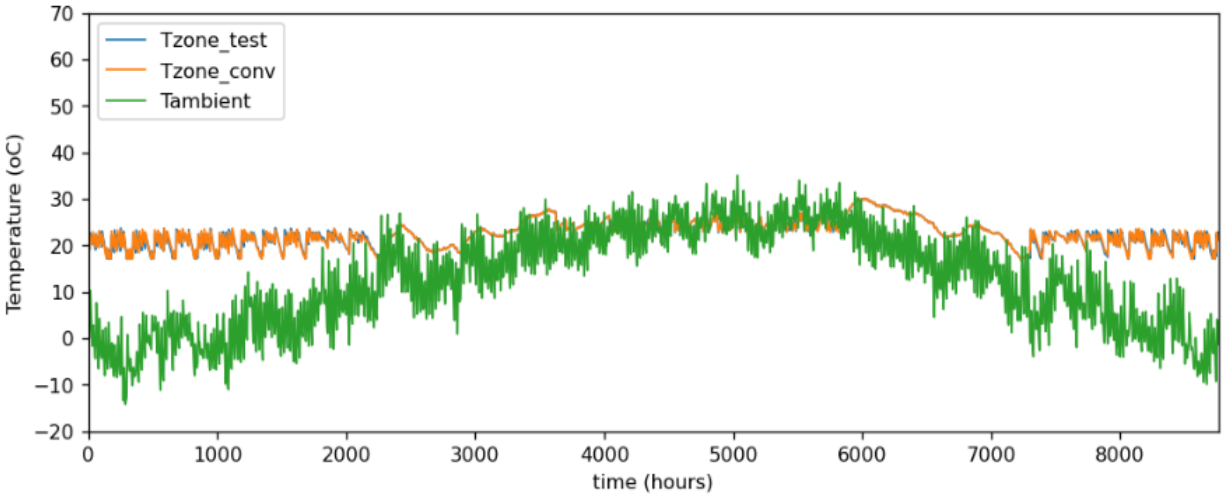

Figure 5.22: a) Building zone temperature variation with the ambient air for Case 1

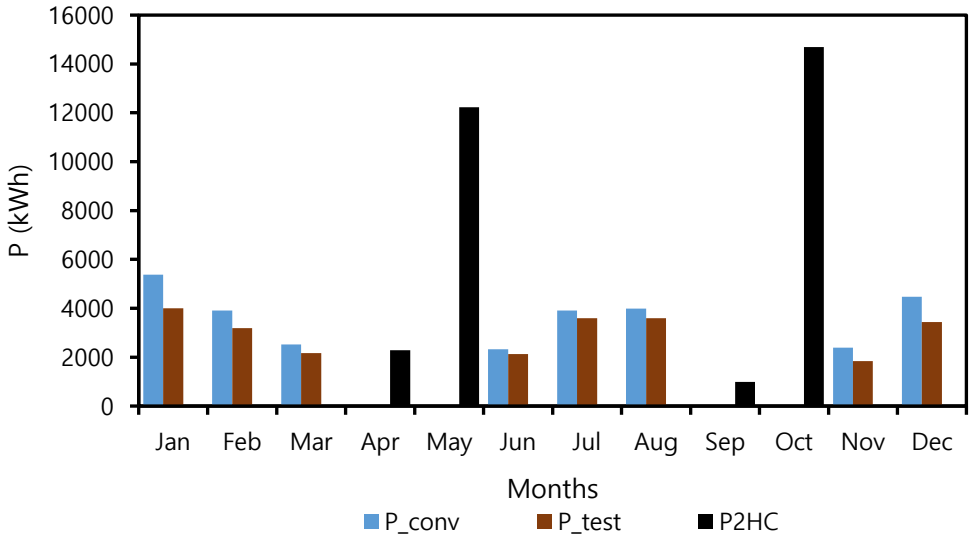

Figure 5.23: Monthly electricity consumption for Case 1

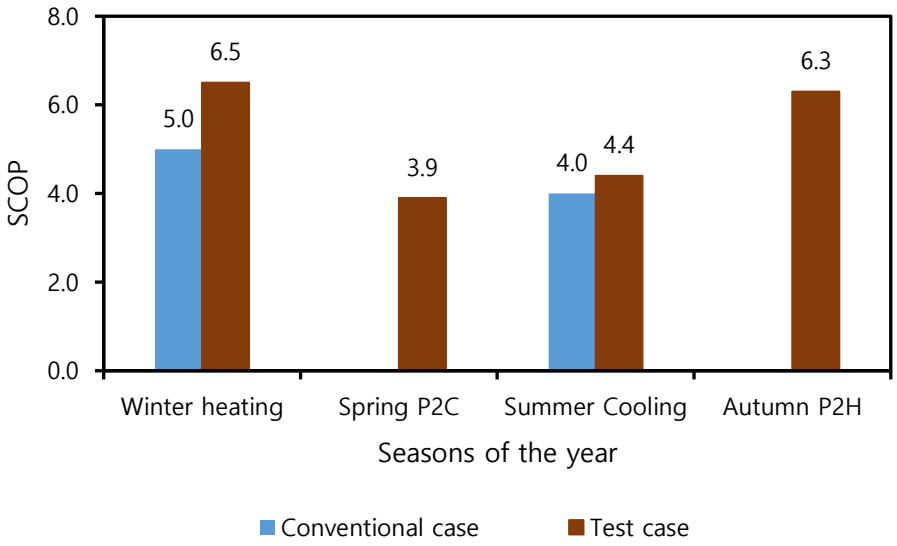

Figure 5.24: SCOP comparison for Case 2

5.3.2 Performance Evaluation of Case 2

In this case study, an ASWL heat pump with P2HC methodology using the shallow UTES developed and calibrated in section 5.2.2 was modeled as shown in Figure 4.14 b) and simulated. This model uses air on the source side for water on the load side. It maintains dual functionality by utilizing the thermal energy stored in the UTES during spring to precool the source air during summer cooling and utilizes this stored energy in autumn for preheating the source air during winter heating. In other words, during the spring and autumn seasons, the air is used on the source side, while during the winter and summer seasons, the thermal energy is effectively used in heating and cooling operations. As mentioned, a conventional (baseline) system without P2HC operation in spring and autumn was modeled for system performance evaluation.

5.3.2.1 Performance evaluation of shallow UTES for Case 2

5.3.2.1.1 Inlet and outlet temperature variation of the UTES for study case 2

In this case, the inlet and outlet temperature variation of the UTES system over the simulation year is shown in Figure 5.25. This figure demonstrates that as P1 is turned on, the flow between the UTES and the installed heat exchanger becomes activated. This flow loop is maintained and due to the high flow rates based on the rated flow of the heat pump, the temperature difference between the inlet and outlet temperatures are low.

Table 5.4: Summary Result Table for Case 1

Case 1										
	Base Case					Test Case				
	Winter	Spring	Summer	Autumn	Total per year	Winter	Spring	Summer	Autumn	Total per year
Q_{Load} (kWh)	91931.61	0.00	40181.17	0.00	-	91931.61		40181.17		-
$Q_{cool/heat}$ (kWh)	93856.20	0.00	40820.14	0.00	-	94901.10	56576.77	41002.76	102568.60	-
$Q_{UTES,c-d}$ (kWh)	0.00	0.00	0.00	0.00	-	5771.08	13175.91	2593.50	21797.75	-
$E_{pv,total}$ (kWh)	108423.37	85612.99	107580.46	60824.94	362441.76	108423.40	85612.98	107580.45	60824.92	362441.75
E_{pv_HnC} (kWh)	18661.22	0.00	10212.24	0.00	28873.46	14618.46	0.00	9320.07	0.00	23938.53
$E_{pv,P2HC}$	0.00	0.00	0.00	0.00	0.00	0.00	14525.15	0.00	15678.75	30203.91
$E_{pv,etc}$	89762.15	24585.79	71401.62	19464.93	205214.49	93804.94	25112.10	72185.30	19719.34	210821.68
$E_{pv,used}$ (kWh)	108423.37	25112.10	81613.85	19719.34	234868.67	108423.40	39637.26	81505.37	35398.09	264964.12
$E_{pv,surplus}$ (kWh)	0.00	60500.89	25966.61	41105.60	127573.09	0.00	45975.73	26075.08	25426.83	97477.63

The outlet fluid from the UTES transfers its energy to the ambient air during winter between 0 and 2160 hours and from 7296 to 8760 hours and similarly in summer, particularly between 3624 and 5832 hours. This analysis delves into the operational dynamics of an air-source water-load (ASWL) heat pump in conjunction with a photovoltaic (PV) system, focusing on its impact on charging the sUTES system. The spring phase of charging (P2C) commenced on April 26, at the 2776th hour of the year, concluding on May 31. Similarly, the autumn phase (P2H) began on September 28, at the 6481st hour, and ended on October 31. These periods were chosen to provide adequate heat for warming or cooling the ground to desired temperatures, aiming to prevent supplying the ground with fluid at freezing temperatures, particularly in the absence of sufficient control methods. The heat transfer fluid entering the sUTES is charged during P2C operation mode. Conversely, in the autumn P2H operation mode, the heat pump provides the sUTES with a temperature of approximately 50°C to efficiently charge the storage volume. The temperature contrast between the inlet and outlet of the UTES demonstrates a substantial heat transfer from the fluid to the ground.

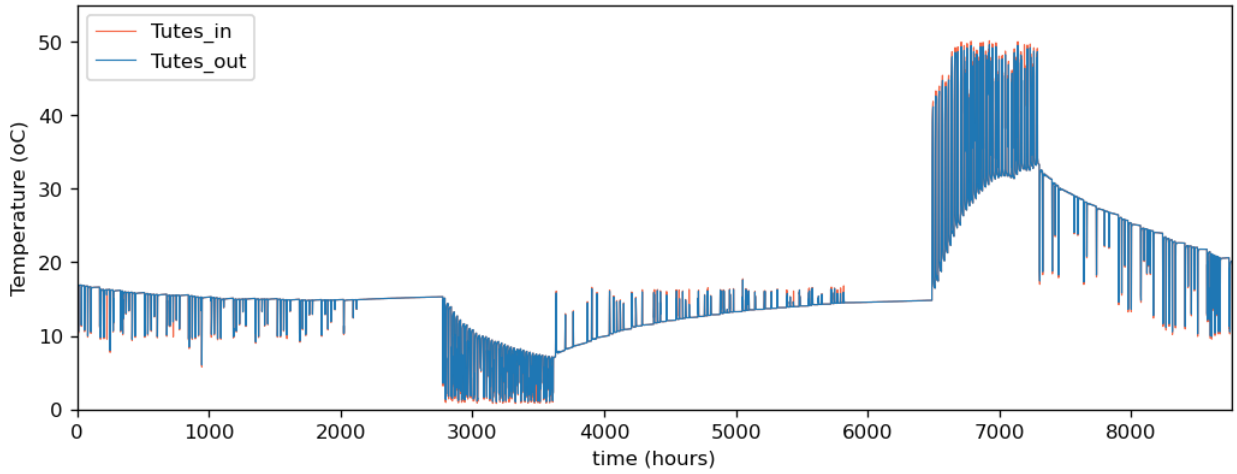

Figure 5.25: Inlet and outlet temperature variation of the UTES for study case 2

5.3.2.1.2 Temperature variation of the ground for Case 2

The mean temperature of the sUTES, referred to as Tutes_ave, is visually depicted in Figure 5.26. During the spring P2C operation, it shows a charging temperature of approximately 7℃, rising from around 16℃, and during the autumn P2H operation, it increases to about 34℃ from the same starting temperature of 16℃. This temperature trend is mirrored in both the center (Tutes_center) and edge (Tutes_edge) temperatures of the UTES, with spring charging

temperatures at around 6°C from the initial 16℃ and autumn temperatures reaching nearly 35℃ from the same starting point. Notably, during winter and summer, there's a noticeable heat exchange between the fluid in the sUTES and the surrounding air within the heat exchanger. This preheated or precooled air is directed to the heat pump's source side. Similar heat exchange processes occur in spring, with heat transferring from the ground to the working fluid, and in autumn, where the opposite happens. The sUTES thermal efficiency was quantitatively assessed using equation (4.31), resulting in an efficiency rate of 34%.

5.3.2.2 Evaluation of Heat Pump Performance for Case 2

This research utilized the dual functions of a heat pump: combining air and water from the sUTES for winter heating and summer cooling while relying solely on air during the spring P2C and autumn P2H operations. Just as in the previous case, the water load serves multiple purposes, providing heating and cooling during winter and summer, respectively, and fulfilling the charging needs of the shallow UTES with surplus energy from the PV system in spring and autumn. Traditionally, ambient air temperature serves as the default source temperature for heat pump operations. Figure 5.27 presents a comparative examination of air inlet temperatures for both conventional and test configurations. Test Case 1 involves precooling and preheating the heat pump's source side through the shallow UTES. In conventional operation, during harsh winter conditions, the heat pump encounters air as cold as -15℃ for heating, while in summer, it faces temperatures up to 35℃ for cooling. However, the test case reveals significant alterations in these temperature ranges due to the integration of air preheating and precooling through sUTES P2HC operation during respective heating and cooling periods. Specifically, for heating, the source side's inlet temperature increased from -15℃ to nearly 20℃ at certain points, while for cooling, it decreased from 35℃ to approximately 13℃. This is clearly illustrated in Figure 5.28, which shows a one-week period of air temperature preheating and precooling.

5.3.2.2.1 Monthly Electricity Consumption of Heat Pump

Consequently, to the improvement of the heat pump performance, as described in the last section, a notable enhancement in the heat pump's power consumption was observed, as depicted in Figure 5.29. Power consumption was higher during the conventional case's heating period (November to March) and cooling period (June to August). Additionally, power

consumption during the spring P2C operation (April and May) and autumn P2H operation (September and October) was also detailed.

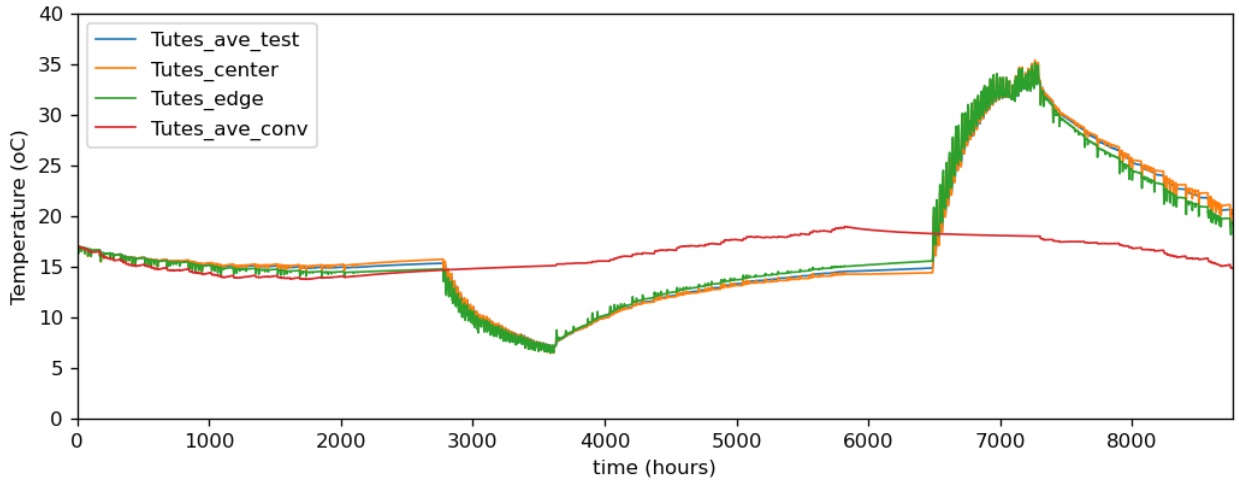

Figure 5.26: Temperature variation of the ground

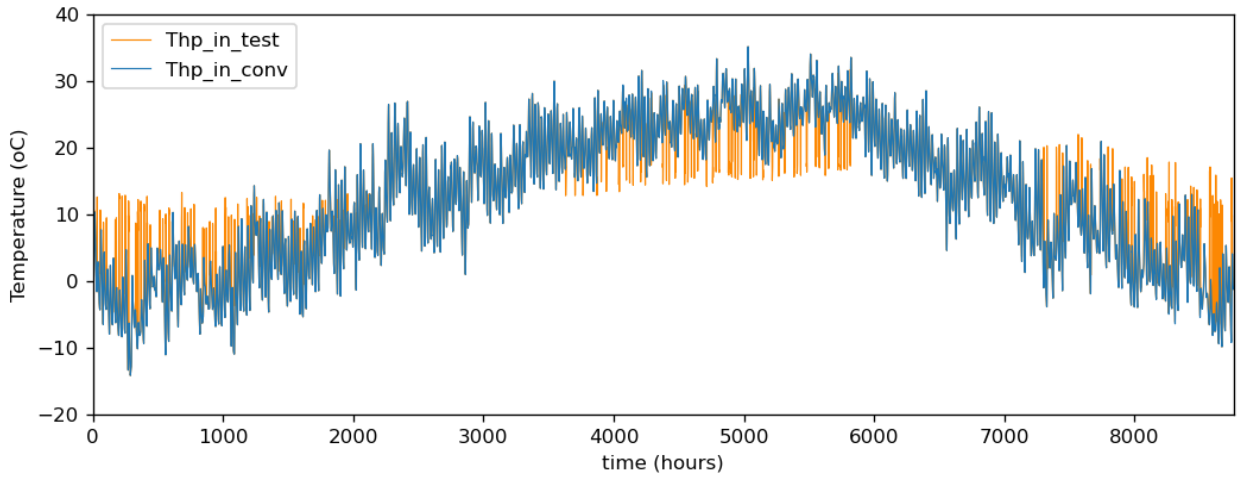

Figure 5.27: Source side inlet temperature to the heat pump for study Case 2

5.3.2.2.2 Seasonal Coefficient of Performance (SCOP) of Case 2

During summer, there was a notable enhancement in the SCOP, with the test case achieving an average COP of 6.1, compared to the conventional case's SCOP of 4.6, as illustrated in Figure 5.30. Similarly, in winter, the test case achieved a SCOP of 4.0 compared to the conventional case's 3.5. Overall, there was a 10% and 26% increase in SCOP for winter heating and summer cooling, respectively, in the test case compared to the conventional case.

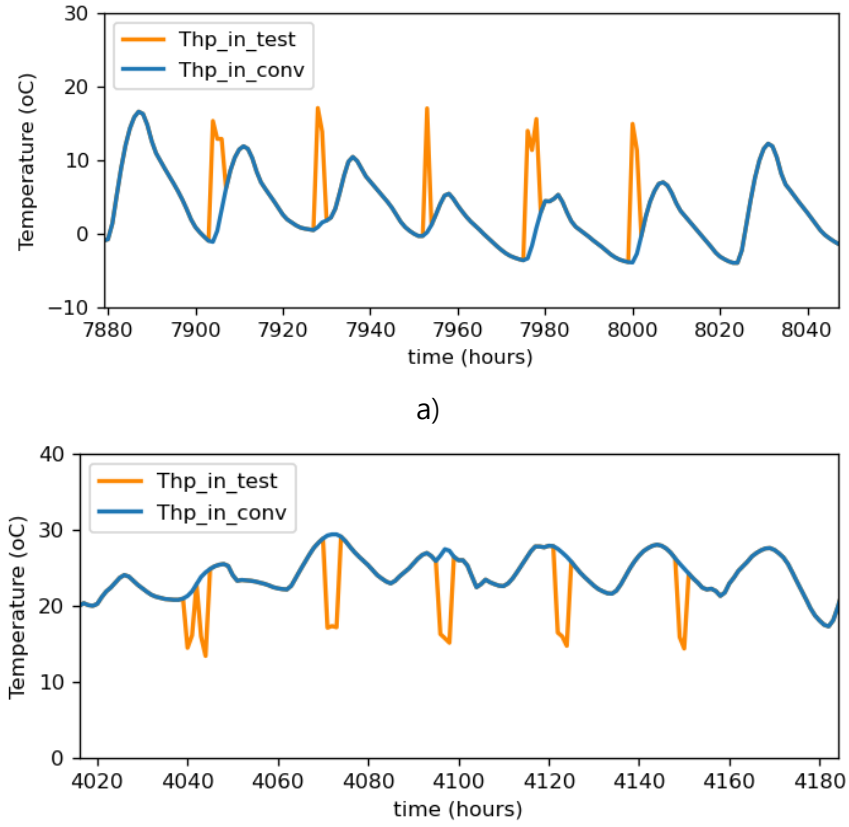

Figure 5.28: one-week view of inlet air temperature to the source side of heat pump for conventional and test cases a) preheating operation in space heating mode and b) precooling operation in space cooling model

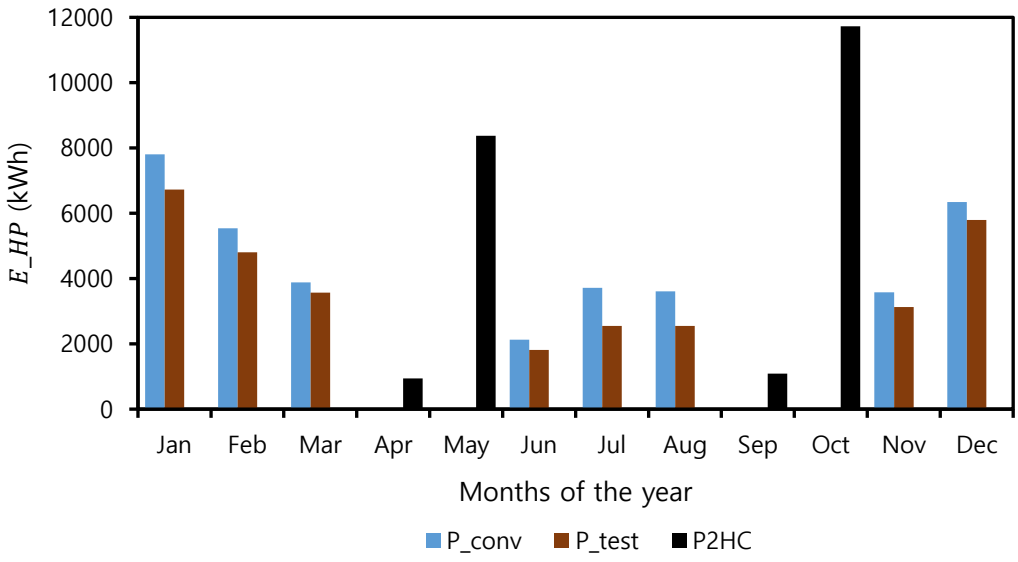

Figure 5.29: Monthly electricity consumption of heat pump for Case 2

Detailed values of essential parameters (defined in the abbreviation section) for both conventional and test cases are provided in Table 5.5, including the thermal and electricity loads shown in Figure 5.18. Minor deviations may be attributed to losses in the flow lines. It's worth noting that surplus PV electricity wasn't available during winter for both cases, indicating that all PV power generated during winter was used on-site, with any additional power drawn from the national grid. Conversely, surplus electricity was generated by solar PV systems during spring, summer, and autumn, necessitating P2HC operation.

5.3.2.2.3 P2HC Efficiency, Percentage Energy savings, SCR, and SEUR for Case 2

These enhancements have played a crucial role in regulating the air source temperature supplied to the heat pump, subsequently boosting its operational efficiency. This improvement is quantitatively demonstrated by analyzing the electrical efficiency and energy savings of the integrated power-to-heat system. Through equations (4.27) and (4.29), the study determined that for Case 1, the P2HC efficiency and energy savings were approximately 26% and 16%, respectively. Additionally, the SCR of 71% was obtained from the test case using equation (4.25) in contrast to the 65% obtained from the conventional case. Furthermore, a SEUR of 21% was obtained using equations (4.26). This result indicates that about 71% of the power generated by the solar PV system per annually was consumed on-site while 21% of the excess electricity generated per year was successfully converted to heat (P2HC operation) during spring and autumn seasons and extracted for heating and cooling operation during winter and summer seasons. In overall, the summary result table for case 2 is shown in Table 5.5.

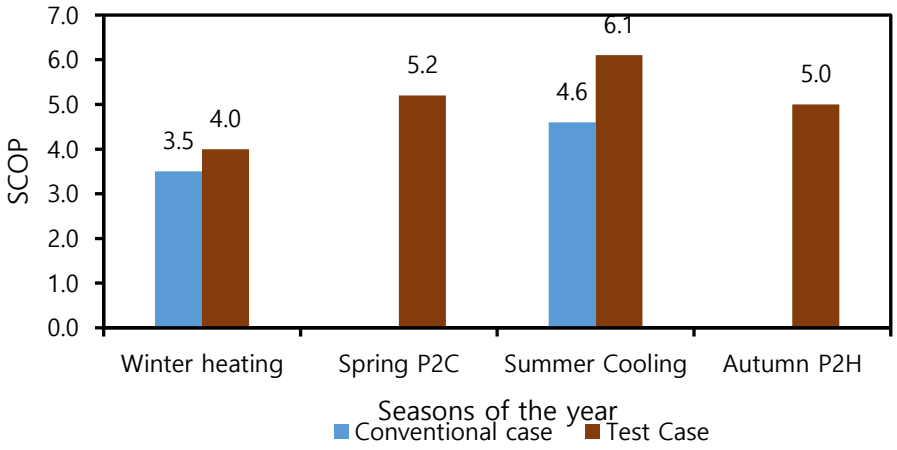

Figure 5.30: SCOP comparison for Case 2

5.3.3 Performance Evaluation of Case 3

In this study case, an ASWL heat pump with P2HC methodology, as shown in Figure 4.14 b) was modeled and simulated. However, in this case, the sUTES was replaced with the deep UTES 150 m as described in section 4.3.1. Similarly, a base case of no P2HC methodology with deep UTES was also modeled and simulated for performance evaluation.

5.3.3.1 Evaluation of 150 m depth UTES in Case 3

5.3.3.1.1 Inlet and outlet temperature variation of the UTES for study case 3

In this case scenario, a 150-meter-deep UTES, paired with the same air source water loop (ASWL) heat pump, was considered. This setup was intended for P2HC utilization during the months when little or no heating or cooling is required, as well as for heating and cooling purposes during relevant seasons. Overall, the analysis of scenario 2 demonstrated performance analogous to Case 2, effectively managing UTES charging and discharging while fulfilling the building's heating and cooling needs. Additionally, the outlet temperature of the HP injected into the ground was constrained to 2℃ during P2C operation in spring and to 50℃ during P2H operation in autumn, as depicted in Figure 5.31. Due to the preheating and precooling of source air into the heat pump, the outlet water temperature during winter decreased to about 10℃ from 17℃ and increased to approximately 16℃ in summer from approximately 9℃.

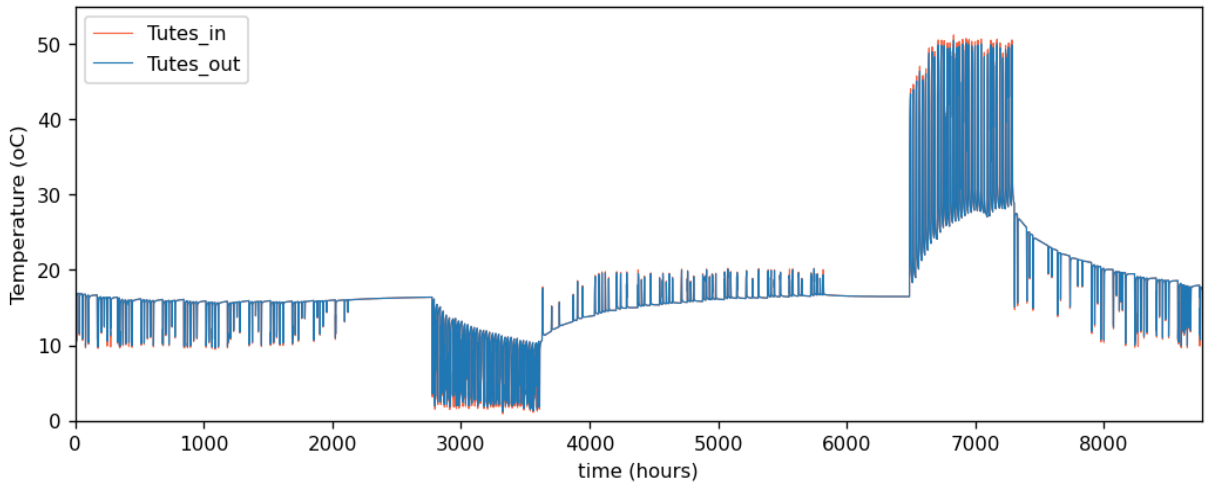

Figure 5.31: Inlet and outlet temperature variation of the UTES for study case 3

Table 5.5: Summary Result Table for Case 2

Case 2										
	Base Case				Total per year	Test Case				Total per year
Parameters	Winter	Spring	Summer	Autumn		Winter	Spring	Summer	Autumn	
Q_{Load} (kWh)	91931.61	0.00	40181.17	0.00	-	91931.61	0.00	40181.17	0.00	-
$Q_{BT2load}$ (kWh)	91416.77	0.00	40181.67	0.00	-	91741.36	0.00	40181.22	0.00	-
$Q_{HP2water}$ (kWh)	94901.10	0.00	43358.55	0.00	-	95835.75	48153.71	42766.93	63474.27	-
$Q_{UTES,c-d}$ (kWh)	0.00	0.00	0.00	0.00	-	14746.65	17538.20	4317.83	38155.51	-
$E_{PV,total}$ (kWh)	108423.37	85612.99	107580.46	60824.94	362441.76	108423.40	85612.94	107580.44	60824.92	362441.70
E_{pv_HnC} (kWh)	27143.19	0.00	9446.88	0.00	36590.06	24009.46	0.00	6900.94	0.00	30910.40
$E_{pv,P2HC}$	0.00	0.00	0.00	0.00	0.00	0.00	9308.74	0.00	12811.65	22120.39
$E_{pv,etc}$	81280.19	24585.79	75549.81	19464.93	200880.72	84413.95	24839.28	75752.66	19655.05	204660.93
$E_{pv,used}$ (kWh)	108423.37	24585.79	84996.69	19464.93	237470.79	108423.40	34148.01	82653.60	32466.71	257691.72
$E_{PV,surplus}$ (kWh)	0.00	61027.20	22583.77	41360.00	124970.98	0.00	51464.93	24926.84	28358.21	104749.98

5.3.3.1.2 Temperature variation of the ground for Case 3

Similar to the prior scenario, this one also illustrates the ground temperature fluctuations, as displayed in Figure 5.32. Here, the average ground temperature decreased to 10℃ from approximately 17℃ during spring P2C operation and rose to 28℃ during autumn P2H operation. Likewise, the temperature at both the edge and center of the 150-meter deep UTES declined to 6℃ during spring P2C operation and ascended to 36℃ during P2H operation. These enhancements, resulting from P2HC operations, led to a notable improvement comparable to scenario 1, achieving a 28% UTES thermal efficiency, quantitatively assessed using Equation (4.31).

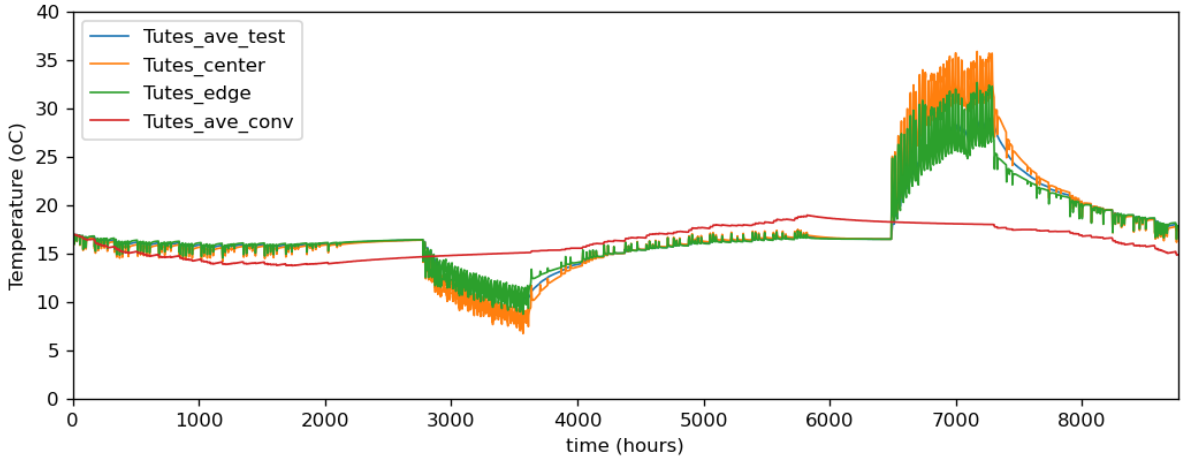

Figure 5.32: Temperature variation of the ground

3.3.3.2 Evaluation of Heat Pump Performance for Case 3

The combination of ASWL and the 150 m deep UTES demonstrated similar heat pump (HP) performance. In the conventional setup, the inlet temperature ranged from approximately -15℃ in winter to about 35℃ in summer. However, in the test case, winter air temperature was raised from around -15℃ to nearly 16℃, while summer temperatures dropped from about 35℃ to a range of 13 to 19℃, as illustrated in Figure 5.33. Despite these improvements leading to better heat pump performance, the achieved efficiency still fell notably short compared to Case 2.

However, these enhancements did result in better monthly power consumption when compared to the conventional setup, as depicted in Figure 5.34, resulting in an increased Seasonal Coefficient of Performance (SCOP) of 3.9 during winter, compared to the conventional SCOP

of 3.5, as shown in Figure 5.35. Similarly, during summer cooling, the SCOP increased to 6.0, contrasting with the conventional SCOP of 4.6. Overall, this refined method yielded an 8% improvement in SCOP during winter and a 24% enhancement during summer cooling compared to the conventional approach.

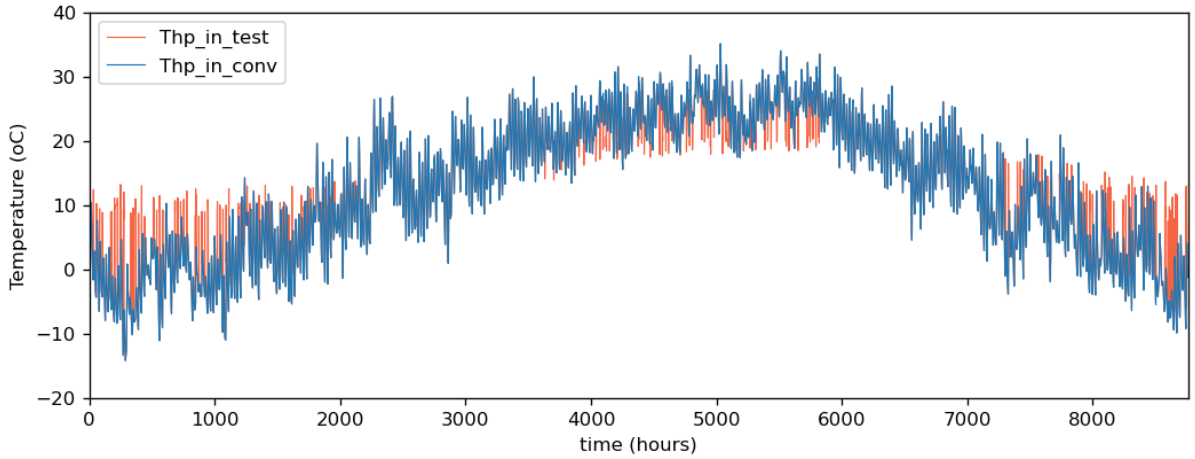

Figure 5.33: Source side inlet temperature to the heat pump for study Case 3

It's important to highlight that while the same air is supplied to the heat pump in both case 1 and case 2 during the spring and autumn seasons, the load supply differs due to varying UTES configurations. Since the efficiency of this type of heat pump relies on factors like the inlet liquid temperature on the load side and flow rates, different SCOP values are possible. This discrepancy in SCOP for spring and autumn between both case 2 and case 3 can be attributed to this reason.

3.3.3.2.1 P2HC Efficiency, Percentage Energy savings, SCR, and SEUR for Case 3

These enhancements have played a crucial role in regulating the air source temperature supplied to the heat pump, subsequently boosting its operational efficiency. This improvement is quantitatively demonstrated by analyzing the electrical efficiency and energy savings of the integrated power-to-heat system. Further examination of case 3 revealed a 22% P2HC efficiency and 13% energy savings. This performance indicated a 4% decrease in P2HC efficiency and a 3% reduction in energy savings compared to case 2, as depicted in Figure 5.36, suggesting superior performance for the shallow UTES with a depth of 1.5 meters and insulation on the top and sides of the storage volume.

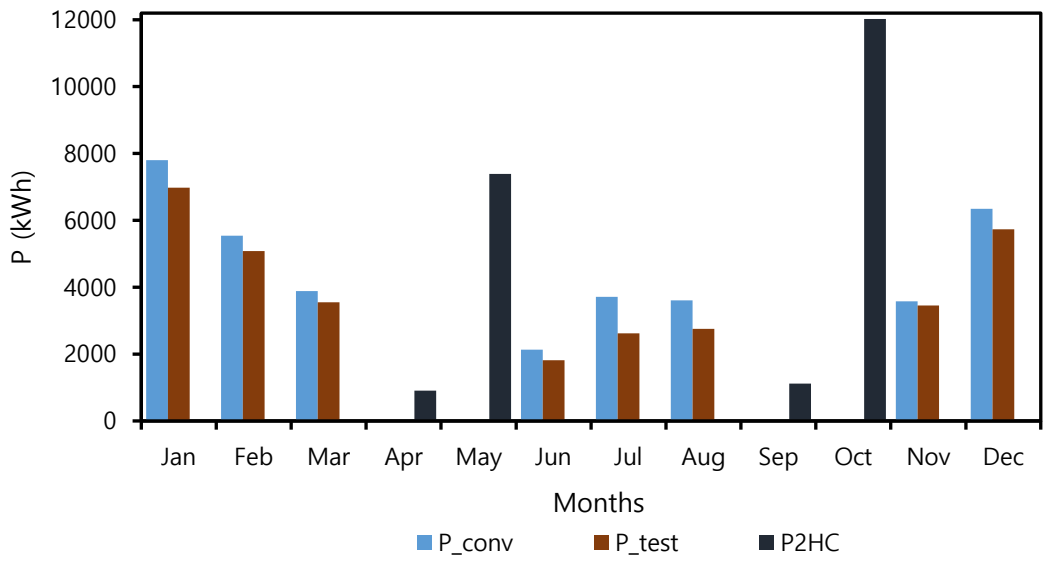

Figure 5.34: Monthly electricity consumption of heat pump for Case 3

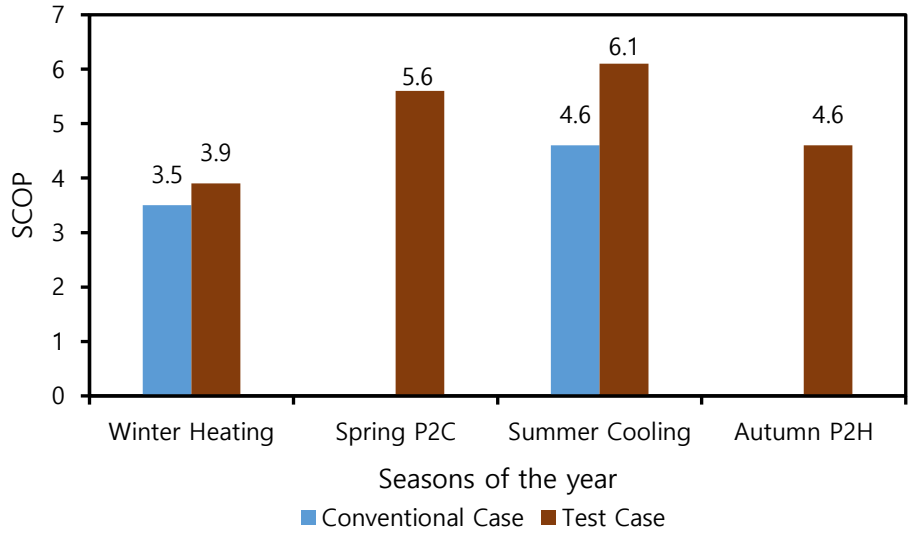

Figure 5.35: SCOP comparison for Case 3

Additionally, the SCR of 71% was obtained from the test case using equation (4.25) in contrast to the 65% obtained from the conventional case. Furthermore, a SEUR of 21% was obtained using equations (4.26). This result indicates that about 71% of the power generated by the solar PV system annually was consumed on-site, while 21% of the excess electricity generated per year was successfully converted to heat (P2HC operation) during the spring and autumn seasons and extracted for heating and cooling operations during the winter and summer

seasons. The summary result for case 3 is shown in Table 5.6 with the result for its conventional case shown in Table 5.5.

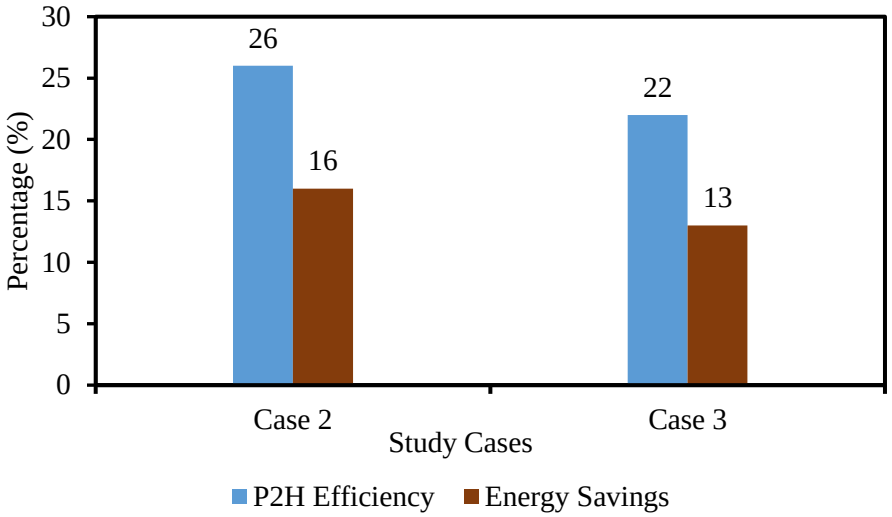

Figure 5.36: Comparison of the P2HC Efficiency and Energy Savings of Case 2 and Case 3

Table 5.6: Summary Result Table for Case 3

Parameters	Test Case				Total per year
	Winter	Spring	Summer	Autumn	
Q_{Load} (kWh)	91931.61	0.00	40181.17	0.00	-
$Q_{BT2load}$ (kWh)	91730.16	0.00	40181.40	0.00	-
$Q_{HP2water}$ (kWh)	96234.15	46557.33	43487.14	59807.31	-
$Q_{UTES,c-d}$ (kWh)	8107.23	14766.99	33814.45	6345.81	-
$E_{PV,total}$ (kWh)	108423.41	85612.73	107580.44	60824.91	362441.49
E_{pv_HnC} (kWh)	24786.50	0.00	7191.61	0.00	31978.11
$E_{pv,P2HC}$	0.00	8297.08	0.00	13138.47	22120.39
$E_{pv,etc}$	83636.91	24812.44	75848.59	18477.5598	202775.49
$E_{pv,used}$ (kWh)	108423.41	33109.52	83040.20	31616.03	256189.15
$E_{pv,surplus}$ (kWh)	0.00	52503.22	24540.24	29208.88	106252.34

5.3.4 Performance Evaluation of Case 4

In this study case, a dual-source dual-load heat pump is conceptualized, modeled, and simulated. It consists of a P2HC strategy that uses 150 m deep UTES. The heat pump uses air on the source side and water on the load side during the non-heating and non-cooling seasons

(spring and autumn). During this time, the heat pump is used for P2HC (charging of the UTES) operation. Additionally, the heat pump uses water on the source side and air supplied directly to the load during the heating and cooling seasons (winter and summer). This conceptualized heat pump was compared with the conventional ASHP shown in Figure 4.12 b) without P2HC strategy.

5.3.4.1 Evaluation of 150 m depth UTES in Case 4

5.3.4.1.1 Inlet and outlet temperature variation of the UTES for study case 4

This study case showcased the outlet temperature of the deep UTES, similar to the previous case, as shown in Figure 5.37. However, the temperature of the working fluid injected into the ground from the heat pump was restricted to a temperature not below 2℃ to avoid supplying a temperature below zero into the ground. During the winter heating period when the outlet water temperature is supplied directly to the heat pump, the temperature decreases to a lower temperature than other cases but sufficient enough to remain within the inlet fluid temperature of the heat pump. The same observation was made during the summer cooling season when the water temperature supplied increased linearly over the cooling time period. In spring P2C, the inlet fluid injected was as low as 2℃ and as high as 40℃ during the autumn P2H, providing sufficient heat for cooling and heating charge, respectively.

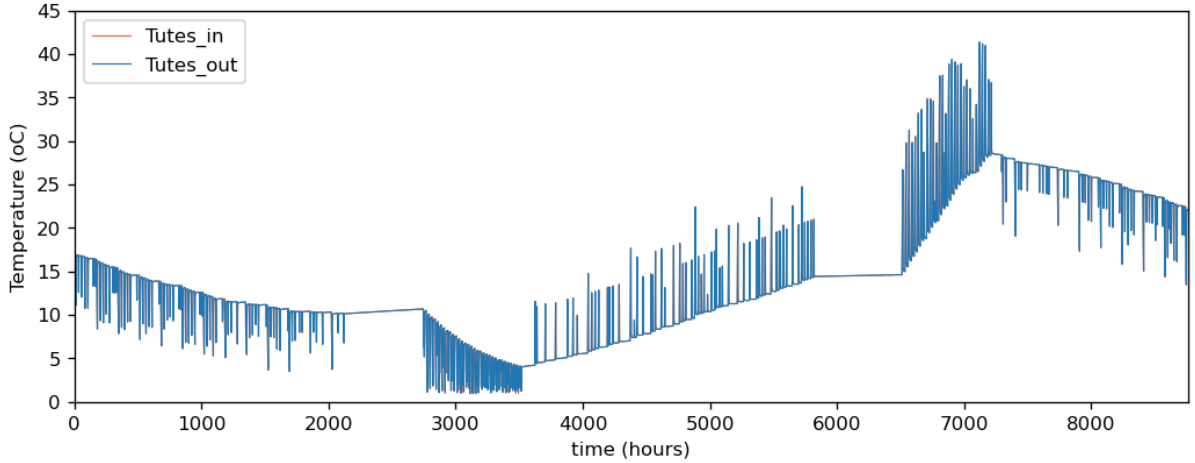

Figure 5.37: Inlet and outlet temperature variation of the UTES for study case 3

5.3.4.1.2 Temperature variation of the ground for Case 4

The ground was adequately charged during the P2HC operation, as observed in Figure 5.38. During the spring P2C, the overall average ground temperature, the mean temperature at the

center and edge of the UTES storage volume, was lowered to a temperature of approximately 4℃ and raised to a temperature of approximately 30℃ during the autumn P2H. This result indicated similar attributes to other study cases; however, the charging was sufficiently better than the previous cases. The heat was extracted during winter for heating and during summer for cooling as described in the following sections.

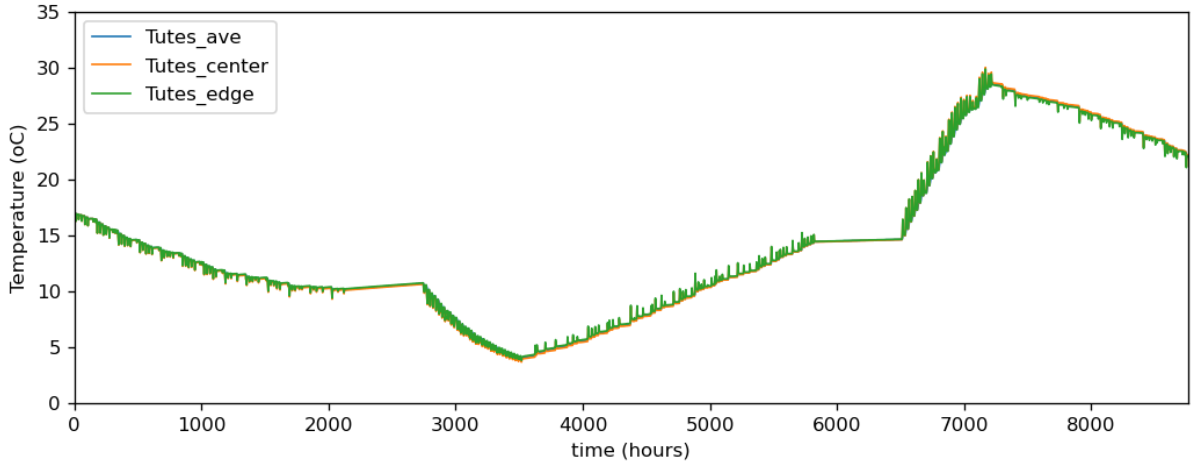

Figure 5.38: Temperature variation of the ground for Case 4

5.3.4.2 Evaluation of Heat Pump Performance for Case 3

The heat pump performed excellently in providing the heating and cooling needs of the case study building. Figure 5.39 demonstrates the outlet temperature of the heat pump. It is observed that an average of 40℃ temperature was supplied to the building during the heating seasons to adequately provide the necessary temperature required by the occupants. This temperature was scaled down to the zone set point temperature, thanks to the control method. This result indicates that the possibility of reversing the source to load and vice versa of the heat pump exists and can provide the necessary heating and cooling loads.

The zone temperature of the conventional case versus the test case is demonstrated in Figure 5.40. The control strategy allows the temperature of the zone to fluctuate between 18 and 22℃ during the heating season and 24 to 26℃ during the cooling season. This is to allow for 4℃ heating deadband and 2℃ cooling deadband to minimize the abrupt on and off of the heat pump during these seasons. Overall, the zone temperature was adequately maintained between the conventional and test cases with an RMSE of 0.5℃ over the simulation year, indicating an excellent performance of the test case scenario.

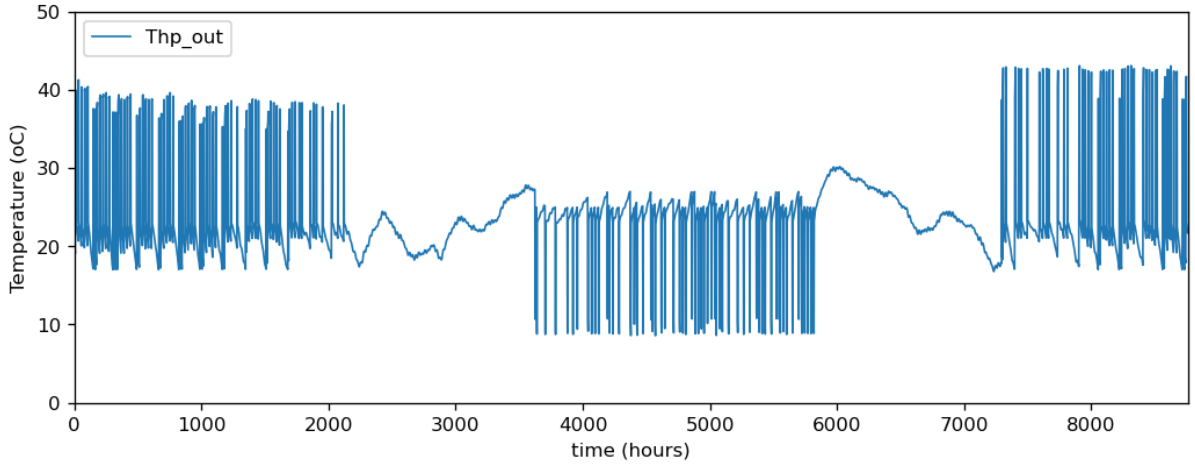

Figure 5.39: Outlet air temperature of the heat pump delivered to the load for Case 4

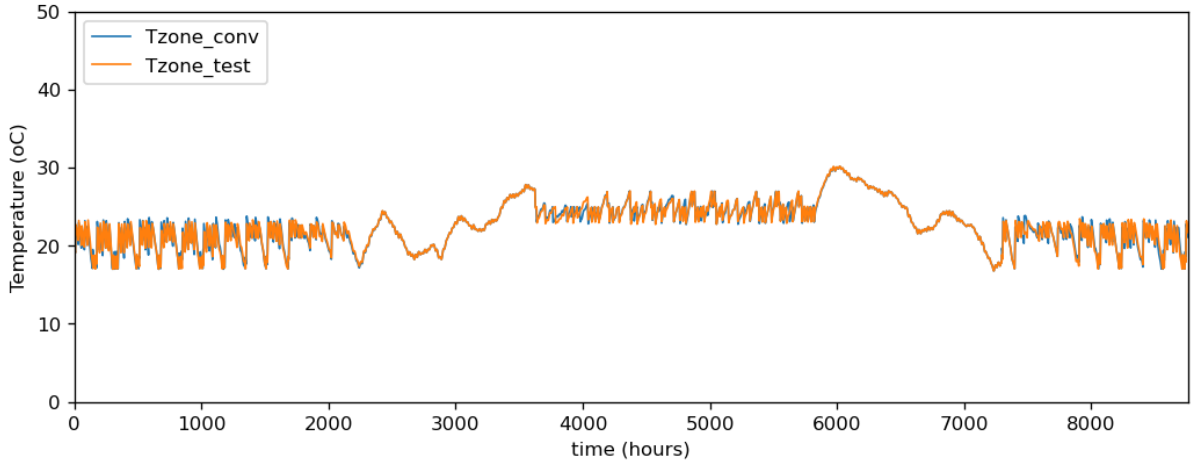

Figure 5.40: Building zone temperature for Case 4

5.3.4.2.1 Monthly Electricity Consumption and SCOP of the heat pump for Case 4

The improvement in the heat pump performance due to the P2HC strategy employed in the study is partly as a result of the electricity consumption which was improved significantly over the months of the year as demonstrated in Figure 5.41. Throughout the months of winter (November to March), the monthly energy consumption of the heat pump was higher in the conventional case than in the test case. This is similar in the months of summer (June to August). Additionally, significant surplus electricity was utilized during P2C operation in the months of spring (April and May) and in the months of autumn (September and October). This result demonstrates the successful implementation of the P2HC strategy for inter-seasonal consumption of solar energy in the case study building.

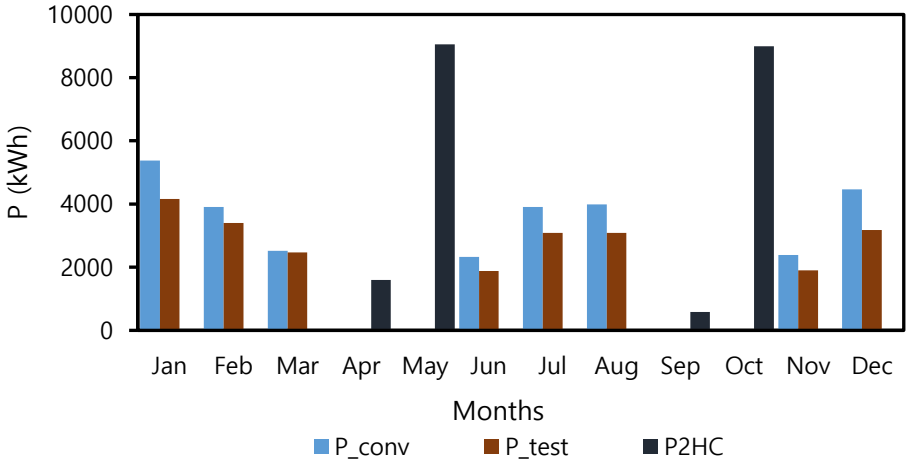

Figure 5.41: Monthly electricity consumption for Case 4

The configuration in the study, along with its control strategy, contributed to a significant improvement in the heat pump performance apart from utilizing the surplus electricity generated from the solar PV system. The seasonal coefficient of performance (SCOP) was improved from 5.0 in the conventional case to 6.2 in the test case during the winter heating season, increasing the SCOP by 19%. These results are demonstrated in Figure 5.42. Similarly, during the summer cooling, the SCOP of 6.1 was obtained from the test case, contrary to the conventional case, where an SCOP of 4.0 was obtained, indicating an increase in the SCOP by 34%. The SCOP for spring P2C and autumn P2H were obtained as 5.4 and 5.2, respectively as shown in Figure 5.42.

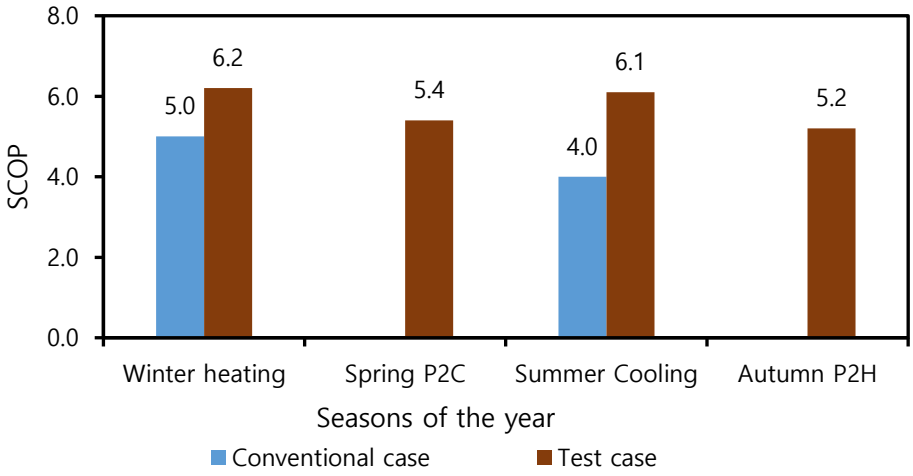

Figure 5.42: SCOP for Case 4

5.3.4.2.2 P2HC Efficiency, Percentage Energy Savings, SCR, and SEUR for Case 4

Equations (4.27) and (4.29) were used to obtain the P2HC efficiency and the percentage energy saving of 28% and 20%, respectively, for the test case scenario. Additionally, the SCR of 70% was obtained for the test case using equation (4.25), in contrast to 64% obtained in the conventional case. Furthermore, a SEUR of 19% was obtained for the test case using equations (4.26). This result indicates that about 70% of the power generated by the solar PV system per annually was consumed on-site while 19% of the excess electricity generated per year was successfully converted to heat (P2HC operation) during spring and autumn seasons and extracted for heating and cooling operation during winter and summer seasons. Overall, the summary result of the case 4 is provided in Table 5.7 with its conventional case same as the one presented for case 1 in Table 5.4.

Table 5.7: Summary Result Table for Case 4

Parameters	Test Case				Total per year
	Winter	Spring	Summer	Autumn	
Q_{Load} (kWh)	91931.61	0.00	40181.17	0.00	-
$Q_{cool/heat}$ (kWh)	94140.06	57232.60	49863.89	49561.25	-
$Q_{UTES,c-d}$ (kWh)	15507.09	9601.11	9591.32	17849.41	-
$E_{PV,total}$ (kWh)	108423.40	85612.98	107580.45	60824.92	362441.75
E_{pv_HnC} (kWh)	15102.56	0.00	8057.62	0.00	23160.18
$E_{pv,P2HC}$	0.00	10658.86	0.00	9578.17	20237.03
$E_{pv,etc}$	93320.84	26023.05	68928.35	20590.14	208862.39
$E_{pv,used}$ (kWh)	108423.40	36681.92	76985.97	30168.31	252259.60
$E_{pv,surplus}$ (kWh)	0.00	48931.07	30594.48	30656.61	110182.16

5.3.5 General Comparison of all Study Cases (Case 1 – 4)

Overall, the performance of the study cases is summarized in Figure 5.43. Regarding SCR, Case 1 exhibited the highest value, consuming about 73% of the solar PV generated per year on-site. This was followed by Cases 2 and 3 and then by Case 4, which recorded yearly on-site PV consumption of approximately 71%, 71%, and 70%. The conventional Case for all cases indicated an SCR of approximately 64% except for Case 2 and Case 3, as observed in Figure 5.43 a). In terms of P2HC efficiency and percentage of the energy saved, as shown in Figure 5.43 b), Case 4 outperformed other cases, achieving a P2HC efficiency of 28%, followed by

Case 2, Cae 3, and Case 1 with P2HC efficiencies of 26%, 22%, and 16%, respectively. For the energy savings, Case 1 achieved the best energy savings with 20%, followed by Cases 1, 2, and 3 with percentage energy savings of 18%, 16%, and 13%, respectively. Furthermore, the SEUR was higher in case 1, with about 34% of yearly surplus energy from the solar PV system consumed successfully, followed by Cases 2, 3, and 4 with SEUR of 21%, 21%, and 19%, respectively, as shown in Figure 5.43 c). Finally, the UTES thermal efficiency shown in Figure 5.43 d) indicates that case 4 achieved the highest UTES thermal efficiency compared to other cases, and this was followed by Cases 2, 3, and 1 with UTES thermal efficiencies of 34%, 28%, and 22%, respectively.

The SCOP for all cases improved with the integration of the UTES for P2HC operation, as shown in Figure 5.44. However, during the heating season, Case 4 outperformed its counterparts, improving the SCOP by 19%, followed by Case 1, 2, and 3, which improved the SCOP during winter heating by 15%, 12%, and 10%, respectively. Similarly, during the summer cooling, Case 4 performed best, enhancing the SCOP by 34%, followed by Case 2, 3, and 1, which enhanced the SCOP by 26%, 25%, and 10%, respectively.

5.4 Model Parametric Analysis

Various parameters influence performance in a complex system configuration such as the study presented in this report. It is important to examine and identify which parameters and how they influence the overall performance of the system; therefore, in this section, sensitivity analysis was performed on the model to ascertain its dynamics to changes in various parameters using Case Study 2. This Case study was selected since its performance in terms of stability and control is higher than in other system scenarios studied in this work. Factors such as the size of the PV, size of the UTES, P2C charging duration, and P2H charging duration were examined. This examination not only provides valuable guidance on the best sizing practices for a unified energy system but also highlights how its different parts interact to produce certain outcomes.

5.4.1 Effects of PV Area

It is evident that adjusting any parameter within the system can potentially improve heat pump performance but may also negatively impact either the self-consumption ratio or thermal energy storage efficiency. This is illustrated in Figure 5.45, where increasing the size of solar PV panels results in decreased efficiency of UTES and P2HC despite a slight uptick in energy

savings. As PV area increases, P2HC and UTES efficiencies decrease sharply but tend to converge at the area 3600 m^2, suggesting that beyond a certain point, further scaling doesn't significantly affect these efficiencies but instead leads to a consistent value. However, this can slightly boost the percentage of energy saved. Exploring these dynamics reveals that the decline in UTES and P2HC efficiencies could stem from increased surplus energy generated with larger PV sizes, particularly during seasons like spring and autumn when P2HC operations occur.

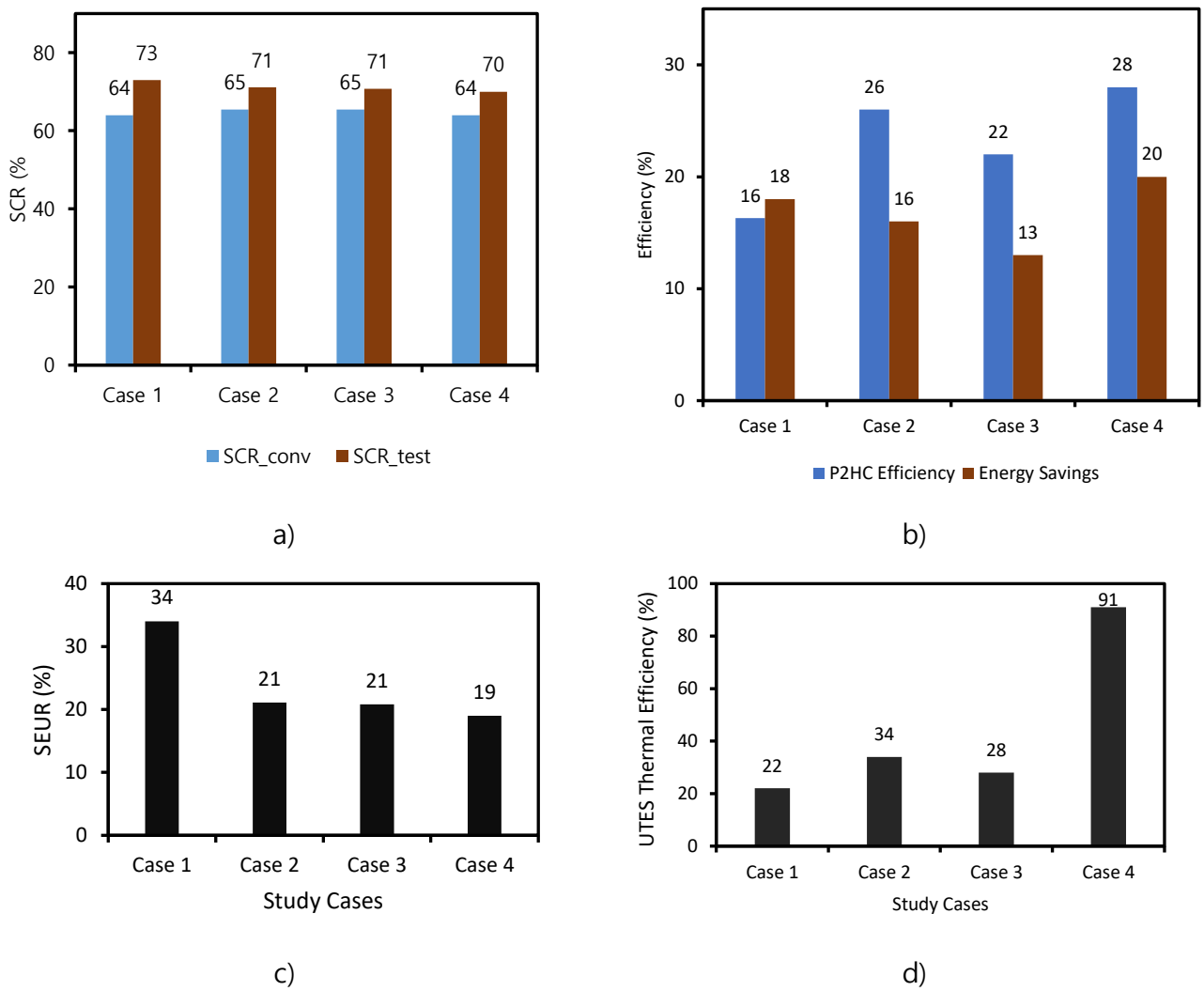

Figure 5.43: General performance evaluation of the study cases based on the key performance indicators defined. a) Comparison of the SCR between the conventional and test cases, b) Comparison of P2HC efficiency and percentage energy savings, c) Comparison of the SEUR, and d) Comparison of the UTES thermal efficiency

Consequently, more heat pump energy is directed into the ground due to the control strategy linking P2HC operations to surplus energy from the PV system during these seasons,

resulting in a notable rise in electricity consumption during P2HC operations. Detailed calculated result during this investigation is presented in Table A- 1 in the appendix section.

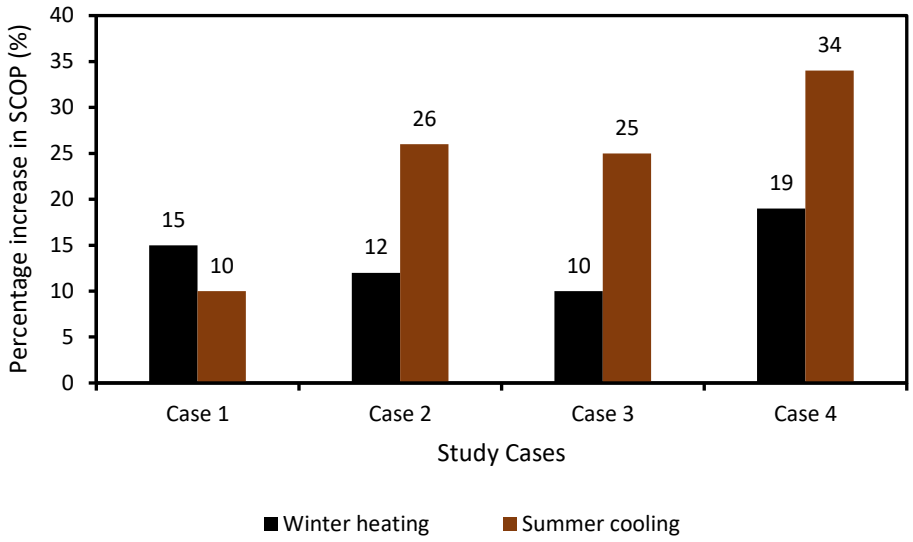

Figure 5.44: Percentage increase in the SCOP during heating and cooling seasons for all cases

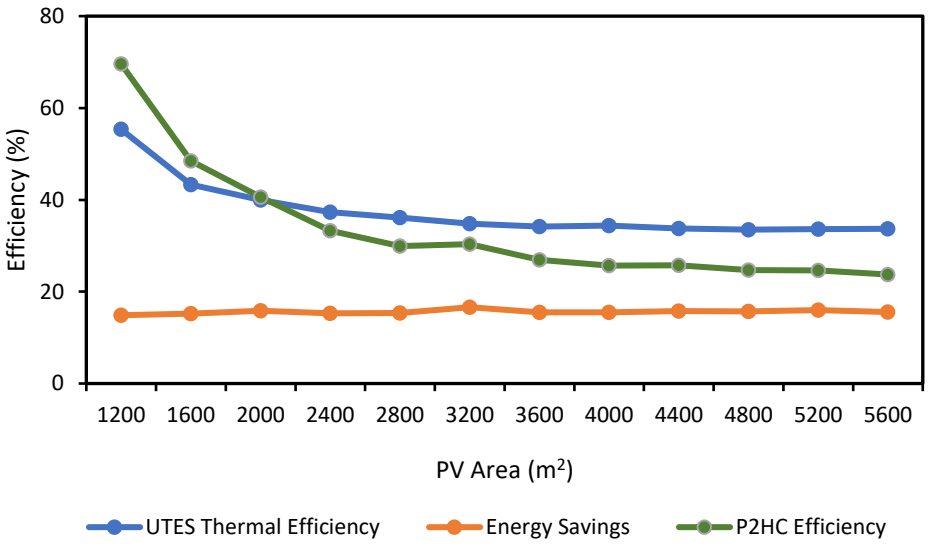

Figure 5.45: Effects of PV area on the system performance

Furthermore, the increase in the area of solar PV installed in the system lowers proportionally the SCR and the SEUR, as demonstrated in Figure 5.46. An observation of the improvement in the SCR for the test case over the conventional case can be made wherein about 7% improvement was achieved. The decrease in the SCR and SEUR as the solar PV area increases

can be attributed to the fact that the higher the PV installation, the higher the power it generates. If the size decreases continuously, the power generation will decrease continuously along with it, and a point will reach where the energy generation would be low, and 100% of it will be consumed on-site, implying a 100% SCR. Similarly, as the PV area increases, the SEUR decreases due to the increased surplus energy per annum. At a lower PV size, zero surplus energy will exist, and this will result in the non-existence of SEUR. Detailed calculated result during this investigation is presented in Table A- 2 in the appendix section.

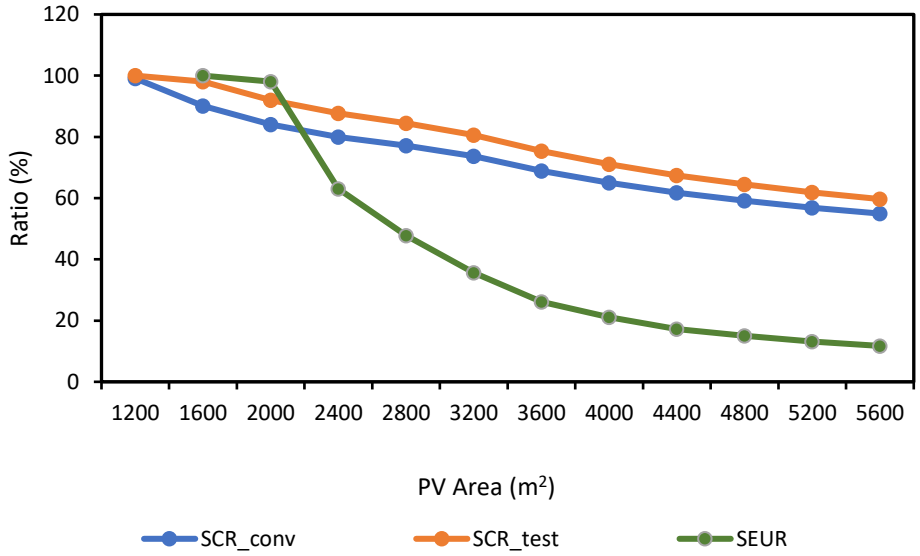

Figure 5.46: Effects of PV area on the SCR and SEUR

5.4.2 Effects of UTES Size

In this section, the impacts of the change in the volume of the UTES are discussed as shown in Figure 5.47. Alterations in the storage volume of the UTES directly impact system performance, as anticipated. With an increase in UTES size, the thermal energy discharged during heating and cooling gradually rises compared to the energy needed for charging. The notable uptick in thermal energy during P2HC operations due to changes in UTES size leads to a decrease in thermal efficiency. However, P2HC efficiency slightly increases from 23% at a UTES volume of 100 m^3 to approximately 29% at 1,420 m^3, mirroring the slight rise in energy savings from 13% at 100 m^3 to about 17% at 1,420 m^3. This shift is attributed to reduced power consumption of the heat pump during heating and cooling seasons, thanks to energy supplementation from P2HC operations. More detailed insights into this trend are outlined in Table A- 3 in the appendix section.

5.4.3 Effects of change in the duration of Spring P2C operation

The timing of both P2C and P2H operations plays a critical role, as delays can result in undercharging or overcharging, negatively impacting overall system performance. Additionally, it's crucial to avoid introducing temperatures below zero into the ground to prevent the working fluid from freezing. These considerations are illustrated in Figure 5.48. Postponing the charging time reduces the energy utilized for charging and the subsequent thermal energy needed to lower the ground temperature.

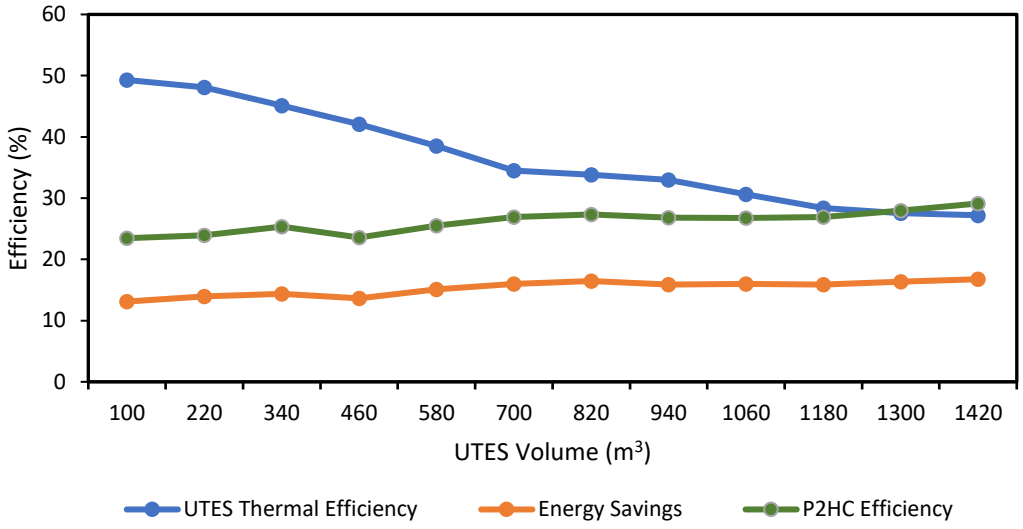

Figure 5.47: Effects of UTES volume on the UTES thermal efficiency, Energy savings, and P2HC efficiency

This is evident in the case of P2C operation in Spring, depicted in Figure 5.48 a). A 3-day (72-hour) delay starting from April 1st resulted in a notable increase in UTES thermal efficiency and P2HC efficiency. UTES thermal efficiency rose from 31% at 2160 hours to 35%, while P2HC efficiency increased from 21% at 2160 hours to 28% at 2952 hours. However, energy savings showed slight fluctuations between 14% and 16%. This shift in P2C timing also marginally decreased the Self-Consumption Ratio (SCR) and the Solar Energy Utilization Ratio (SEUR), as shown in Figure 5.48 b). The surplus energy from the solar PV system utilized during P2C operation decreased, leading to reduced electricity usage from the surplus generated, thereby lowering the SEUR by 8% when postponed from 2160 hours to 2952 hours. This observation aligns with the slight decrease in SCR, as energy consumption from the total solar PV-generated energy slightly decreased. More detailed calculations regarding this trend are provided in Table A- 4 in the appendix section.

5.4.4 Effects of change in the duration of Spring P2H operation

Delaying the timing of P2H operations in Autumn, much like adjusting P2C timing, proves highly advantageous. As shown in Figure 5.49 a), there's a clear correlation: the longer the delay in P2H operation, the more pronounced the improvement in UTES thermal efficiency and P2HC efficiency, accompanied by a slight increase in energy savings. This trend mirrors what we observed with P2C operation, indicating a common underlying principle. However, the reasoning behind this effect varies slightly.

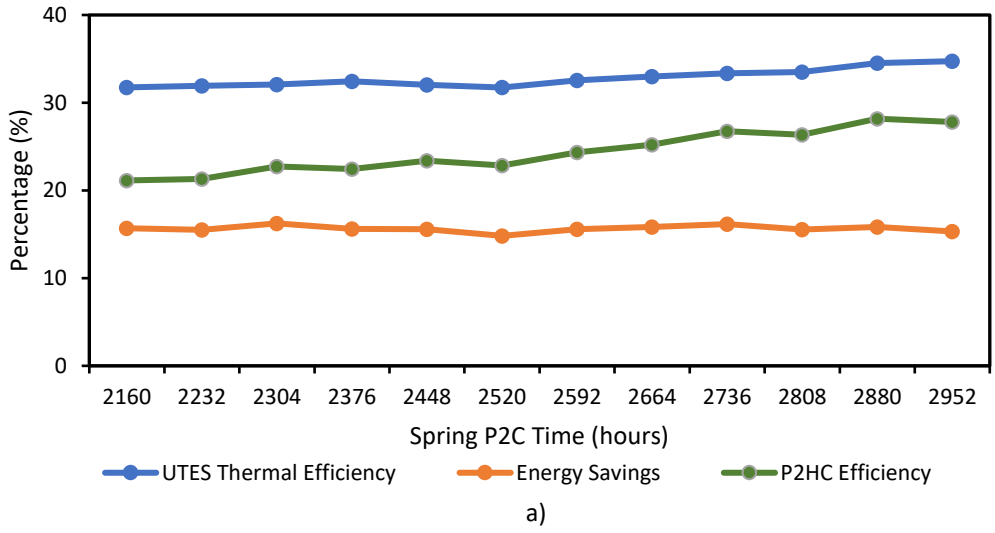

a)

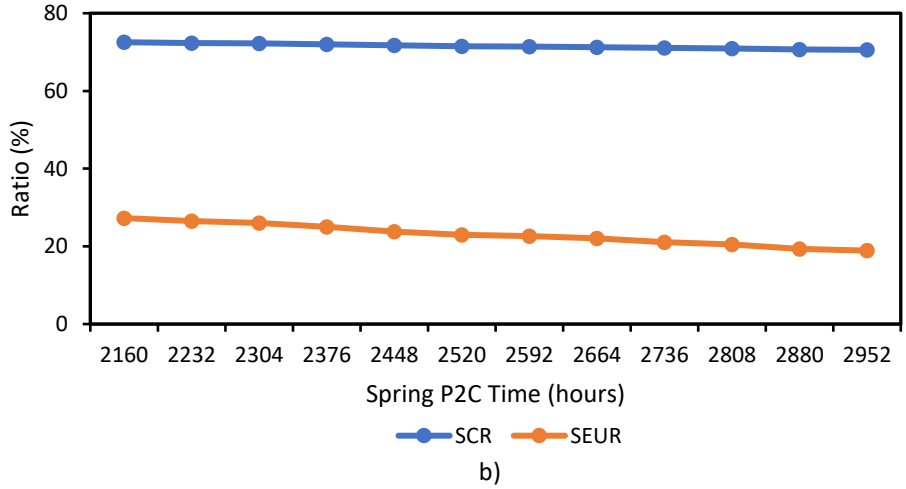

b)

Figure 5.48:: Effects of change in the duration of spring P2C operation

When P2H operation is postponed, the thermal energy needed to raise ground temperature decreases, leading to an increase in UTES thermal efficiency from 29% at 5832 hours to 36% at 6624 hours. Furthermore, this delay curtails electricity consumption from surplus generation. As depicted in Figure 5.49 b), this dual impact resulted in a slight decrease in SCR by 3% from 5832 hours to 6624 hours and a 10% reduction in SEUR by delaying from 5832 hours to 6624 hours. Essentially, delaying P2H operations emerges as a strategic move, offering manifold benefits from improved thermal efficiency to diminished electricity usage. These findings underscore the pivotal role of timing optimization in maximizing system performance. More detailed calculations regarding this trend are provided in Table A-5 of the appendix.

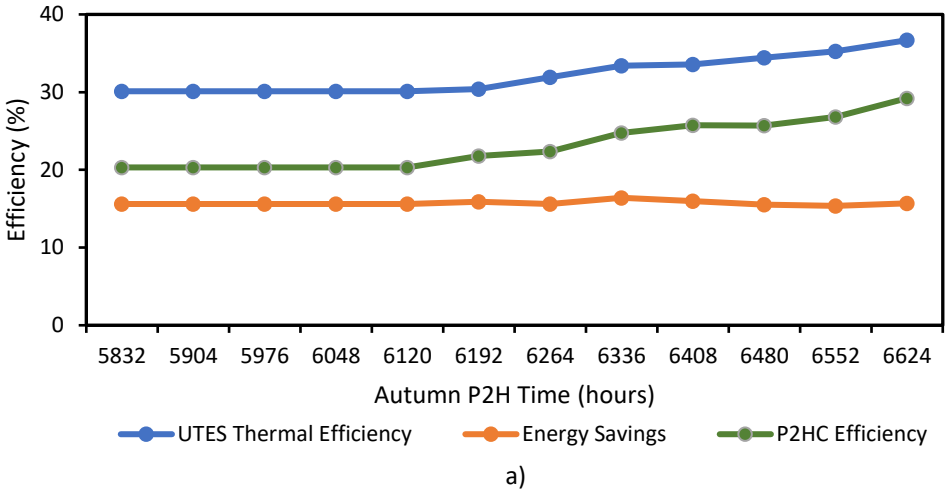

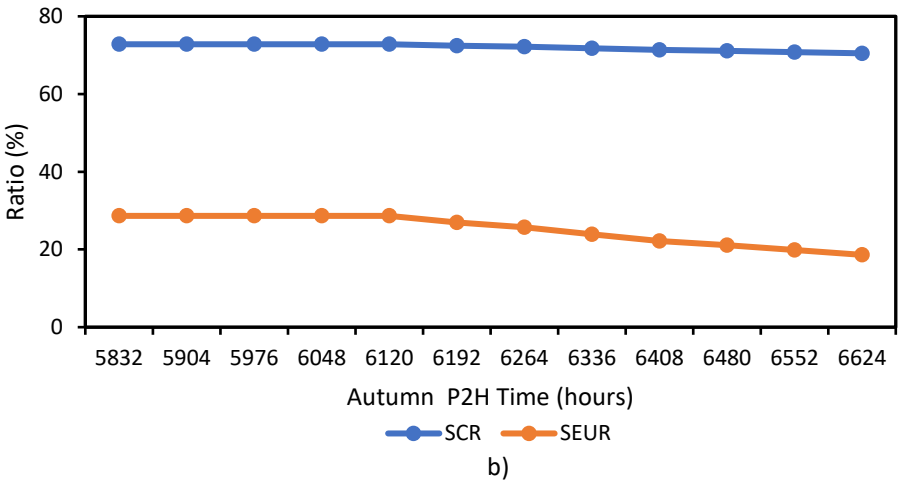

Figure 5.49: Effects of change in the duration of spring P2C operation

5.5 Economic Advantage of Integrating Shallow UTES

This study examined the economic feasibility of integrating the UTES system to utilize the excess electricity produced by the installed solar PV. It is important to note that this section does not provide a critical economic analysis of the entire system. However, it highlights the economic implication of using the UTES system for minimizing the amount of energy which are generated by the solar PV system that may be exported to the national grid, which may cause voltage and frequency instability, as well as a high ramping rate or may go to waste in the case of developing countries where Feed-in-Tariff (FiT) and net metering are yet to be fully implemented. For the system cases studied in this research, energy savings of 18%, 16%, 13%, and 20% were obtained for Cases 1, 2, 3, and 4, respectively. This implies that by integrating the UTES system, surplus electricity generation in buildings will be utilized and save a significant amount of energy spent in meeting the building space heating and cooling.

Additionally, LCoH was utilized in this study to determine the economic viability of the integrated 800 m^3 UTES system by considering its initial capital cost, annual operation, and maintenance cost, annual heat extracted for heating and cooling purposes, the discount rate, and the lifespan of 25 years. The result of this investigation indicated LCoH of USD 0.45/kWh. These results will be helpful in making informed decisions regarding the cost and long-term benefits of the system. Overall, calculating LCOH offers a comprehensive and standardized approach to evaluating the economic viability, long-term sustainability, and financial implications of heating systems. The LCoH obtained in this study shows the integration of the UTES system is economically feasible. It is crucial in guiding investment decisions, optimizing system performance, and advancing the transition to cost-effective and sustainable heating solutions.

CHAPTER 6: CONCLUSIONS AND RECOMMENDATIONS

6.1 Conclusions

In this study, the primary goal was to model and simulate a solar-assisted dual-source heat pump system integrated with underground thermal energy storage (UTES) for use in heating and building space conditioning. To accomplish this task, various specific objectives must be achieved.

First, the inverse grey-box model for vertical and horizontal configurations of UTES systems, with insulation on the top and sides of their storage volumes for the purpose of minimizing thermal losses, was developed using thermal network analysis and the TRNSYS simulation tool. An experimental study on the actual system was performed, and the data from this field experiment were used to calibrate the developed models for heating and cooling applications using heat pumps. Although the purpose of the conducted experiment was to obtain the data required for calibrating the developed IGB models, its assessment for both configurations was done. The evaluation of the experimental study demonstrated that both the vertical and horizontal UTES systems exhibit considerable abilities to store and release heat during the charging and discharging phases. However, the horizontal setup shows superior charging and discharging rates when comparing the two configurations under the installation and experimental conditions of different lengths of the piping materials and flow rates. In general, the provision of insulation of 0.2 m thickness on the side and top of each configuration's storage volume minimized the heat losses from the top and sides of the storage volumes of both configurations, redirecting most of the heat loss through the bottom of the systems. The performance of both system configurations validates their use for the calibration of the developed IGB models.

The IGB models were successfully calibrated and evaluated. The IGB model developed in TRNSYS and the 4R2C IGB model developed using a thermal network were calibrated using measured data. Similarly, the 4R2C IGB model was calibrated with data generated from the calibrated (trained) TRNSYS model. In summary, when comparing the calibrated models, the TRNSYS model trained using measured data in the horizontal setup demonstrated the highest performance with CVRMSE of 2.97%, followed by the inverse model also trained with measured data which produced 3.17% CVRMSE, then the inverse model trained with the

TRNSYS generated data with CVRMSE of 4.42%. Conversely, the detailed TRNSYS model trained with measured data in the vertical configuration showed superior performance, with CVRMSE of 3.16%, followed by the inverse model trained with the TRNSYS generated data with CVRMSE of 5.42%, then inverse model trained with measured data with CVRMSE of 7.91%. Despite variations in calibration performance across scenarios, the calibrated models aligned reasonably well with field experimental data within the ASHRAE guidelines' recommended range of 0 – 20% coefficient of variation root mean square error (CVRMSE). Falling within this range indicates that the model's predictions closely approximate actual data, enabling effective heating and cooling system behavior simulation.

Ultimately, based on the sensitivity study of the IGB models, their performance hinges greatly on the duration of their training and testing durations. Extending the training period while holding the testing time constant notably enhances the model's performance, with errors gradually converging. Moreover, the model exhibits superior performance when the testing duration is less than the trained data duration. Furthermore, in long-term evaluations, the model's effectiveness improves with the training duration, reaching convergence after 20 weeks. Past this training duration, minimal to no performance enhancement is noticeable. This 20-week convergence point signifies a brief training duration capable of predicting the model's output over an extended period, a distinct advantage of the proposed IGB model over machine learning approaches like artificial neural networks (ANN), which necessitate longer training data for extended output predictions.

The second specific objective of this study developed a simulation model composed of a heat pump, UTES system, solar PV system, building space, and other sub-components, employing simple and adequate control methods to utilize the surplus electricity that is generated by the solar PV system installed on 4000 m^2 area, for assisting the 160 kW heat pump (50kW and 40 kW heating and cooling capacities, respectively) in providing the electricity and thermal energy requirement of the case study building through the use of 800 m^3 sized UTES for P2HC strategy. For the case study building, a public school building in Jincheon, Korea, was used to evaluate this developed system configuration and its control strategy. Simulation of this system configuration and its control strategy shows that it is capable of utilizing excess surplus electricity generated from the installed solar PV inter-seasonally to charge the UTES system. P2H operation was achieved in the spring season, and the stored cold heat was extracted during

the summer season for building space cooling with the use of a heat pump. Similarly, P2H operation was accomplished during autumn, and warm heat was extracted during winter for building space heating using a heat pump.

Thirdly, in this study, different heat pumps, such as the ASAL with shallow UTES (Case 1), ASWL with shallow UTES (Case 2), ASWL with deep UTES (Case 3), and dual-source dual-load heat pump (Case 4), which operates as ASWL during non-heating and non-cooling periods, and WSAL during heating and cooling periods with deep UTES systems, were modeled and simulated to evaluate the system configuration and its control methods. Conventional (baseline) cases for each of the configurations without UTES P2HC strategy were modeled for performance evaluation, except for Case 4, where the baseline case for Case 1 was used for comparison. Six performance indexes were defined for their performance evaluation: the SCR, P2HC efficiency, annual percentage of energy savings, SEUR, UTES thermal efficiency, and SCOP. Generally, all the study cases showcased good performance that validates the system configuration and control technique. Regarding SCR in general, Case 1 exhibited the highest value, consuming about 73% of the solar PV generated per year on-site. This was followed by Cases 2 and 3 and then by Case 4, which recorded yearly on-site PV consumption of approximately 71%, 71%, and 70%. The conventional Case for all cases indicated an SCR of approximately 64% except for Case 2 and Case 3. In terms of P2HC efficiency and percentage of the energy saved, Case 4 outperformed other cases, achieving a P2HC efficiency of 28%, followed by Case 2, Case 3, and Case 1 with P2HC efficiencies of 26%, 22%, and 16%, respectively. For the energy savings, Case 1 achieved the best energy savings with 20%, followed by Cases 1, 2, and 3 with percentage energy savings of 18%, 16%, and 13%, respectively. Furthermore, the SEUR was higher in case 1, with about 34% of yearly surplus energy from the solar PV system consumed successfully, followed by Cases 2, 3, and 4 with SEUR of 21%, 21%, and 19%, respectively. In addition, the UTES thermal efficiency indicates that case 4 achieved the highest UTES thermal efficiency compared to other cases, and this was followed by Cases 2, 3, and 1 with UTES thermal efficiencies of 34%, 28%, and 22%, respectively. Finally, the SCOP for all the study cases was improved significantly over the conventional cases. During the heating season, Case 4 outperformed its counterparts, improving the SCOP by 19%, followed by Case 1, 2, and 3, which improved the SCOP during winter heating by 15%, 12%, and 10%, respectively. Similarly, during the summer cooling,

Case 4 performed best, enhancing the SCOP by 34%, followed by Case 2, 3, and 1, which enhanced the SCOP by 26%, 25%, and 10%, respectively.

The fourth specific objective of the study was to perform a sensitivity analysis of the system. For this objective, one of the systems (Case 2) was selected for parametric analysis to determine how the model responds to changes in some parameters, such as the size of the PV, the size of the UTES, the P2C duration, and the P2H duration. The proposed system demonstrates sensitivity to various parameters tested. This necessitates a systematic approach for optimal performance. The increase in the PV system inversely affects UTES thermal efficiency and P2HC efficiency while marginally enhancing energy savings, eventually reaching a point of convergence. This convergence point should represent the optimal size with a safety margin to ensure cost-effectiveness and accommodate unforeseen variables. Prior studies have linked UTES's total installation cost, including drilling expenses, to its size; therefore, for cost-efficiency in UTES sizing, a moderate volume is recommended based on our analysis, as it tends to enhance performance. Within this context, a UTES size ranging from 700 m3 to 940 m3 is suggested for similar system setups, as further increases beyond this range yield diminishing returns in energy savings and P2HC efficiency while maintaining UTES thermal efficiency at a satisfactory level. Additionally, delaying P2C or P2H operations enhances UTES thermal efficiency, P2HC efficiency, and energy savings to a minor extent. However, the applicability of this phenomenon depends on the sizes of system components, and caution must be exercised to prevent overcharging without proper control mechanisms. Therefore, postponing both P2C and P2H durations appears cost-effective, as demonstrated in our study.

Finally, the integrated UTES system underwent a brief economic analysis using the levelized cost of heat (LCoH) to ascertain its economic viability. For the system cases studied in this research, energy savings of 18%, 16%, 13%, and 20% were obtained for Cases 1, 2, 3, and 4, respectively. This implies that by integrating the UTES system, surplus electricity generation in buildings will be utilized and save a significant amount of energy spent in meeting the building space heating and cooling. Additionally, the LCoH of $0.45/kWh was obtained. These results indicate the utilization of UTES for the P2HC strategy in utilizing the redundant electricity from the solar PV system.

6.2 Recommendations

In this study, a simplified 4R2C IGB model for shallow UTES systems in vertical and horizontal configurations was developed and calibrated for application. Several assumptions were made to achieve the presented results. The study utilized Two capacitances on the grouting node and the ground (soil) node. It is possible that adding another capacitance at the T_w node may yield a more accurate result. Similarly, reducing the capacitance and resistances may affect the system performance. Therefore, some modifications, such as comparing the present 4R2C model with 4R3C, 3R1C, and 2R1C models, should be made in future research. This will provide more insight into the thermal network that will best describe the systems. Additionally, the inlet and exit pipe of the U-tube borehole heat exchangers may be considered, along with the resistances and capacitances on its heat conduction path, to create a 5R4C model that may be compared with the aforementioned reduced order models for the UTES system.

Furthermore, a more detailed building can be modeled using the Type56 from the TRNSYS component library in developing the model configuration. This will model in detail the heat interactions in the building. With this in mind, developing this model with a ground-source water-load (GSWL) heat pump for performance comparison is also important. This type of heat pump is highly applicable in commercial buildings such as public schools. In addition to this modification, this methodology can be applied for small-scale consumption, such as in residential buildings. In this case, daily charging and discharging of the UTES using surplus electricity from the PV that is redundant, especially during the peak hours in residential buildings may be considered along with the model's inter-seasonal operation, which was accomplished in this study. This approach in residential buildings may be interesting as it has the potential to save significant energy for domestic homes in countries where selling to the grid poses a challenge.

Due to the time and resources required, the present work was limited to a simplified economic analysis, focusing on the LCoH of the integrated UTES system. Despite this, the findings proved that this system configuration is economically viable. However, in future research, a separate topic focusing on the technical and economic analysis of solar-assisted dual-source or dual-load heat pumps with integrated underground thermal energy storage should be considered for either residential or commercial applications. This will give an in-depth insight

into the technical and financial feasibility of widely adopting this system in heating and cooling, especially in domestic buildings.

REFERENCES

Abualqumboz, M., Rodley, D., 2018. Mathematical modelling of smart solar heating system with the deployment of borehole thermal energy storage to increase renewable heat share in Dundee, UK. Energy Procedia 151, 37–46.

Adenle, A.A., 2019. Assessment of solar energy technologies in Africa-opportunities and challenges in meeting the 2030 agenda and sustainable development goals. Energy Policy 111180. https://doi.org/10.1016/j.enpol.2019.111180

Alahmer, A., Ajib, S., 2020. Solar cooling technologies: State of art and perspectives. Energy Convers. Manag. 214, 112896. https://doi.org/10.1016/j.enconman.2020.112896

Amarasinghe, K., Wijayasekara, D., Carey, H., Manic, M., Dawei He, Wei-Peng Chen, 2015. Artificial neural networks based thermal energy storage control for buildings, in: IECON 2015 - 41st Annual Conference of the IEEE Industrial Electronics Society. Presented at the IECON 2015 - 41st Annual Conference of the IEEE Industrial Electronics Society, IEEE, Yokohama, pp. 005421–005426. https://doi.org/10.1109/IECON.2015.7392953

Aranzabal, I., Gomez-Cornejo, J., López, I., Zubiria, A., Mazón, J., Feijoo-Arostegui, A., Gaztañaga, H., 2023. Optimal Management of an Energy Community with PV and Battery-Energy-Storage Systems. Energies 16, 789.

Arunachala, U.C., Kundapur, A., 2020. Cost-effective solar cookers: A global review. Sol. Energy 207, 903–916. https://doi.org/10.1016/j.solener.2020.07.026

ASHRAE, 2014. ASHRAE Guideline 14-2014—Measurement of Energy, Demand, and Water Savings.

ASHRAE, 2001. The 2001 ASHRAE Fundamental Handbook, 2001 Edition. ed. ASHRAE.

Aydin, M., Jung, Y.-S., Lee, H.-I., Kim, K.-D., Yang, J.-E., 2012. Calculation of Thermal Conductivity and Heat Capacity from Physical Data for Some Representative Soils of Korea. Korean J. Soil Sci. Fertil. 45, 1–8. https://doi.org/10.7745/KJSSF.2012.45.1.001

Babatunde, O.M., Munda, J.L., Hamam, Y., 2022. Hybridized off-grid fuel cell/wind/solar PV /battery for energy generation in a small household: A multi-criteria perspective. Int. J. Hydrog. Energy 47, 6437–6452. https://doi.org/10.1016/j.ijhydene.2021.12.018

Başer, T., McCartney, J.S., 2020. Transient evaluation of a soil-borehole thermal energy storage system. Renew. Energy 147, 2582–2598. https://doi.org/10.1016/j.renene.2018.11.012

Bee, E., Prada, A., Baggio, P., Psimopoulos, E., 2019. Air-source heat pump and photovoltaic systems for residential heating and cooling: Potential of self-consumption in different European climates. Build. Simul. 12, 453–463. https://doi.org/10.1007/s12273-018-0501-5

Belmonte, J.F., Díaz-Heras, M., Almendros-Ibáñez, J.A., Cabeza, L.F., 2022. Simulated performance of a solar-assisted heat pump system including a phase-change storage tank for residential heating applications: A case study in Madrid, Spain. J. Energy Storage 47, 103615. https://doi.org/10.1016/j.est.2021.103615

Bordignon, S., Quaggiotto, D., Vivian, J., Emmi, G., De Carli, M., Zarrella, A., 2022. A solar-assisted low-temperature district heating and cooling network coupled with a ground-source heat pump. Energy Convers. Manag. 267, 115838. https://doi.org/10.1016/j.enconman.2022.115838

Braun, J., Chaturvedi, N., 2002. An Inverse Gray-Box Model for Transient Building Load Prediction. HVACR Res. 8, 73–99. https://doi.org/10.1080/10789669.2002.10391290

Brown, C.S., Kolo, I., Falcone, G., Banks, D., 2023. Repurposing a deep geothermal exploration well for borehole thermal energy storage: Implications from statistical modelling and sensitivity analysis. Appl. Therm. Eng. 220, 119701. https://doi.org/10.1016/j.applthermaleng.2022.119701

Brown, C.S., Kolo, I., Lyden, A., Franken, L., Kerr, N., Marshall-Cross, D., Watson, S., Falcone, G., Friedrich, D., Diamond, J., 2024. Assessing the technical potential for underground thermal energy storage in the UK. Renew. Sustain. Energy Rev. 199, 114545. https://doi.org/10.1016/j.rser.2024.114545

Buker, M.S., Riffat, S.B., 2016. Solar assisted heat pump systems for low temperature water heating applications: A systematic review. Renew. Sustain. Energy Rev. 55, 399–413. https://doi.org/10.1016/j.rser.2015.10.157

Calise, F., Cappiello, F.L., Cimmino, L., Dentice d'Accadia, M., Vicidomini, M., 2023. Dynamic simulation and thermoeconomic analysis of a power to gas system. Renew. Sustain. Energy Rev. 187, 113759. https://doi.org/10.1016/j.rser.2023.113759

Çengel, Y.A., Ghajar, A.J., 2015. Heat and mass transfer: fundamentals & applications, Fifth edition. ed. McGraw Hill Education, New York, NY.

Chakraborty, D., Elzarka, H., 2018. Performance testing of energy models: are we using the right statistical metrics? J. Build. Perform. Simul. 11, 433–448. https://doi.org/10.1080/19401493.2017.1387607

Cox, J., Belding, S., Lowder, T., 2022. Application of a novel heat pump model for estimating economic viability and barriers of heat pumps in dairy applications in the United States. Appl. Energy 310, 118499. https://doi.org/10.1016/j.apenergy.2021.118499

Deguenon, L., Yamegueu, D., Moussa Kadri, S., Gomna, A., 2023. Overcoming the challenges of integrating variable renewable energy to the grid: A comprehensive review of electrochemical battery storage systems. J. Power Sources 580, 233343. https://doi.org/10.1016/j.jpowsour.2023.233343

Dehghani-Sanij, A.R., Tharumalingam, E., Dusseault, M.B., Fraser, R., 2019. Study of energy storage systems and environmental challenges of batteries. Renew. Sustain. Energy Rev. 104, 192–208. https://doi.org/10.1016/j.rser.2019.01.023

Drucker, C.T., Senger, L.W., Pacioles, C.T., 2023. Application of the weibull model to describe the kinetic behaviors of thiol decolorizers in chlorogenic acid-lysine solutions. J. Food Eng. 339, 111287. https://doi.org/10.1016/j.jfoodeng.2022.111287

Duffie, J.A., Beckman, W.A., 2013. Solar Engineering of Thermal Processes, 1st ed. Wiley. https://doi.org/10.1002/9781118671603

Duffie, J.A., Beckman, W.A., Blair, N., 2020. Solar engineering of thermal processes, photovoltaics and wind. John Wiley & Sons.

Eastop, T.D., McConkey, A., 1993. Applied Thermodynamics for Engineering and Technologists.

Ebersviller, S.M., Jetter, J.J., 2020. Evaluation of performance of household solar cookers. Sol. Energy 208, 166–172. https://doi.org/10.1016/j.solener.2020.07.056

Eze, F., Egbo, M., Anuta, U.J., Ntiriwaa, O.-B.R., Ogola, J., Mwabora, J., 2024a. A review on solar water heating technology: Impacts of parameters and techno-economic studies. Bull. Natl. Res. Cent. 48, 29. https://doi.org/10.1186/s42269-024-01187-1

Eze, F., Lee, W., An, Y.S., Joo, H., Lee, K., Ogola, J., Mwabora, J., 2024b. Experimental and simulated evaluation of inverse model for shallow underground thermal storage. Case Stud. Therm. Eng. 59, 104535. https://doi.org/10.1016/j.csite.2024.104535

Eze, F., Ogola, J., Kivindu, R., Egbo, M., Obi, C., 2022. Technical and economic feasibility assessment of hybrid renewable energy system at Kenyan institutional building: A case study. Sustain. Energy Technol. Assess. 51, 101939. https://doi.org/10.1016/j.seta.2021.101939

Fambri, G., Mazza, A., Guelpa, E., Verda, V., Badami, M., 2023. Power-to-heat plants in district heating and electricity distribution systems: A techno-economic analysis. Energy Convers. Manag. 276, 116543. https://doi.org/10.1016/j.enconman.2022.116543

Fleischer, A.S., 2015. Thermal Energy Storage Using Phase Change Materials Fundamentals and Applications.

Gaonwe, T.P., Hohne, P.A., Kusakana, K., 2022. Optimal energy management of a solar-assisted heat pump water heating system with a storage system. J. Energy Storage 56, 105885. https://doi.org/10.1016/j.est.2022.105885

Grossi, I., Dongellini, M., Piazzi, A., Morini, G.L., 2018. Dynamic modelling and energy performance analysis of an innovative dual-source heat pump system. Appl. Therm. Eng. 142, 745–759. https://doi.org/10.1016/j.applthermaleng.2018.07.022

Gultekin, A., Aydin, M., Sisman, A., 2016. Thermal performance analysis of multiple borehole heat exchangers. Energy Convers. Manag. 122, 544–551. https://doi.org/10.1016/j.enconman.2016.05.086

Herrando, M., Simón, R., Guedea, I., Fueyo, N., 2021. The challenges of solar hybrid PVT systems in the food processing industry. Appl. Therm. Eng. 184, 116235. https://doi.org/10.1016/j.applthermaleng.2020.116235

Hohne, P.A., 2023. A simplified control method for a water heating load coupled to a hybrid energy system to improve inverter longevity. Energy Rep. 9, 145–150. https://doi.org/10.1016/j.egyr.2023.08.045

Hohne, P.A., Kusakana, K., Numbi, B.P., 2019. A review of water heating technologies : An application to the South African context. Energy Rep. 5, 1–19. https://doi.org/10.1016/j.egyr.2018.10.013

Hong, T., Kim, C.-J., Jeong, J., Kim, J., Koo, C., Jeong, K., Lee, M., 2016. Framework for Approaching the Minimum CV(RMSE) using Energy Simulation and Optimization Tool. Energy Procedia 88, 265–270. https://doi.org/10.1016/j.egypro.2016.06.157

Hossain, Md.S., Abboodi Madlool, N., Al-Fatlawi, A.W., El Haj Assad, M., 2023. High Penetration of Solar Photovoltaic Structure on the Grid System Disruption: An Overview of Technology Advancement. Sustainability 15, 1174. https://doi.org/10.3390/su15021174

Ismaeel, H.H., Yumrutaş, R., 2020a. Thermal performance of a solar-assisted heat pump drying system with thermal energy storage tank and heat recovery unit. Int. J. Energy Res. 44, 3426–3445. https://doi.org/10.1002/er.4966

Ismaeel, H.H., Yumrutaş, R., 2020b. Investigation of a solar assisted heat pump wheat drying system with underground thermal energy storage tank. Sol. Energy 199, 538–551.

Jakubek, D., Ocłoń, P., Nowak-Ocłoń, M., Sułowicz, M., Varbanov, P.S., Klemeš, J.J., 2023. Mathematical modelling and model validation of the heat losses in district heating networks. Energy 267, 126460. https://doi.org/10.1016/j.energy.2022.126460

Jeon, B.-K., Kim, E.-J., Shin, Y., Lee, K.-H., 2018. Learning-Based Predictive Building Energy Model Using Weather Forecasts for Optimal Control of Domestic Energy Systems. Sustainability 11, 147. https://doi.org/10.3390/su11010147

Jha, K., Shaik, A.G., 2023. A comprehensive review of power quality mitigation in the scenario of solar PV integration into utility grid. E-Prime - Adv. Electr. Eng. Electron. Energy 3, 100103. https://doi.org/10.1016/j.prime.2022.100103

Karami, M., Abdshahi, H., 2023. Energy and exergy analysis of the transient performance of a qanat-source heat pump using TRNSYS-MATLAB co-simulator. Energy Environ. 34, 560–585. https://doi.org/10.1177/0958305X211068152

Kazimierczuk, A.H., 2019. Wind energy in Kenya: A status and policy framework review. Renew. Sustain. Energy Rev. 107, 434–445. https://doi.org/10.1016/j.rser.2018.12.061

Khan, M.K., Khan, F., 2012. A Comparative Study of White Box, Black Box and Grey Box Testing Techniques. Int. J. Adv. Comput. Sci. Appl. 3, 12–15.

Kim, J., Nam, Y., 2020. Development of the Performance Prediction Equation for a Modular Ground Heat Exchanger. Energies 13, 6005. https://doi.org/10.3390/en13226005

Kim, K., Kim, J., Nam, Y., Lee, E., Kang, E., Entchev, E., 2021. Analysis of Heat Exchange Rate for Low-Depth Modular Ground Heat Exchanger through Real-Scale Experiment. Energies 14, 1893. https://doi.org/10.3390/en14071893

Kim, M.-H., Kim, D., Heo, J., Lee, D.-W., 2019. Techno-economic analysis of hybrid renewable energy system with solar district heating for net zero energy community. Energy 187, 115916. https://doi.org/10.1016/j.energy.2019.115916

Kodešová, R., Vlasáková, M., Fér, M., Teplá, D., Jakšík, O., Neuberger, P., Adamovský, R., 2013. Thermal properties of representative soils of the Czech Republic. Soil Water Res. 8, 141–150. https://doi.org/10.17221/33/2013-SWR

Koşan, M., Aktaş, M., 2021. Experimental investigation of a novel thermal energy storage unit in the heat pump system. J. Clean. Prod. 311, 127607. https://doi.org/10.1016/j.jclepro.2021.127607

Kupiec, K., Larwa, B., Gwadera, M., 2015. Heat transfer in horizontal ground heat exchangers. Appl. Therm. Eng. 75, 270–276. https://doi.org/10.1016/j.applthermaleng.2014.10.003

Laloui, L., Rotta Loria, A.F., 2020. Analytical modelling of transient heat transfer, in: Analysis and Design of Energy Geostructures. Elsevier, pp. 409–456. https://doi.org/10.1016/B978-0-12-816223-1.00009-6

Lamarche, L., 2019. Horizontal ground heat exchangers modelling. Appl. Therm. Eng. 155, 534–545. https://doi.org/10.1016/j.applthermaleng.2019.04.006

Lee, D., Ooka, R., Ikeda, S., Choi, W., Kwak, Y., 2020. Model predictive control of building energy systems with thermal energy storage in response to occupancy variations and time-variant electricity prices. Energy Build. 225, 110291. https://doi.org/10.1016/j.enbuild.2020.110291

Li, B., Liu, Z., Wu, Y., Wang, P., Liu, R., Zhang, L., 2023. Review on photovoltaic with battery energy storage system for power supply to buildings: Challenges and opportunities. J. Energy Storage 61, 106763.

Li, X., Yilmaz, S., Patel, M.K., Chambers, J., 2023. Techno-economic analysis of fifth-generation district heating and cooling combined with seasonal borehole thermal energy storage. Energy 285, 129382. https://doi.org/10.1016/j.energy.2023.129382

Li, Y., O'Neill, Z., Zhang, L., Chen, J., Im, P., DeGraw, J., 2021. Grey-box modeling and application for building energy simulations - A critical review. Renew. Sustain. Energy Rev. 146, 111174. https://doi.org/10.1016/j.rser.2021.111174

Li, Y., Zhang, N., Ding, Z., 2020. Investigation on the energy performance of using air-source heat pump to charge PCM storage tank. J. Energy Storage 28, 101270. https://doi.org/10.1016/j.est.2020.101270

Lin, Y., Bu, Z., Yang, W., Zhang, H., Francis, V., Li, C.-Q., 2022. A Review on the Research and Development of Solar-Assisted Heat Pump for Buildings in China. Buildings 12, 1435. https://doi.org/10.3390/buildings12091435

Liu, H., Cai, J., 2021. A robust gray-box modeling methodology for variable-speed direct-expansion systems with limited training data. Int. J. Refrig. 129, 128–138. https://doi.org/10.1016/j.ijrefrig.2021.05.007

Lu, S., Huang, S., Wang, R., Yu, Z., 2023. Performance study and heating simulation on novel latent heat thermal energy storage device suit for air source heat pump. J. Energy Storage 65, 107259. https://doi.org/10.1016/j.est.2023.107259

Ma, Y., Xi, J., Cai, J., Gu, Z., 2023. TRNSYS simulation study of the operational energy characteristics of a hot water supply system for the integrated design of solar coupled air source heat pumps. Chemosphere 338, 139453. https://doi.org/10.1016/j.chemosphere.2023.139453

Maestre, I.R., Gallero, F.J.G., Gómez, P.Á., Pérez-Lombard, L., 2015. A new RC and g-function hybrid model to simulate vertical ground heat exchangers. Renew. Energy 78, 631–642. https://doi.org/10.1016/j.renene.2015.01.045

Maestre, I.R., González Gallero, F.J., Álvarez Gómez, P., Mena Baladés, J.D., 2013. Performance assessment of a simplified hybrid model for a vertical ground heat exchanger. Energy Build. 66, 437–444. https://doi.org/10.1016/j.enbuild.2013.07.041

Mahon, H., O'Connor, D., Friedrich, D., Hughes, B., 2022. A review of thermal energy storage technologies for seasonal loops. Energy 239, 122207. https://doi.org/10.1016/j.energy.2021.122207

Mane, S.R., Kale, Dr.R.V., 2021. Investigation of Performance Parameters Affecting the Efficiency of Solar Water Heater: A Review. IOP Conf. Ser. Mater. Sci. Eng. 1091, 012021. https://doi.org/10.1088/1757-899X/1091/1/012021

Marinelli, S., Lolli, F., Gamberini, R., Rimini, B., 2019. Life Cycle Thinking (LCT) applied to residential heat pump systems: A critical review. Energy Build. 185, 210–223. https://doi.org/10.1016/j.enbuild.2018.12.035

Martínez-Gracia, A., Uche, J., del Amo, A., Bayod-Rújula, Á.A., Usón, S., Arauzo, I., 2022. Energy and environmental benefits of an integrated solar photovoltaic and thermal hybrid, seasonal storage and heat pump system for social housing. Appl. Therm. Eng. 213, 118662.

Miglioli, A., Aste, N., Del Pero, C., Leonforte, F., 2023. Photovoltaic-thermal solar-assisted heat pump systems for building applications: Integration and design methods. Energy Built Environ. 4, 39–56. https://doi.org/10.1016/j.enbenv.2021.07.002

Mohana, Y., Mohanapriya, R., Anukiruthika, T., Yoha, K.S., Moses, J.A., Anandharamakrishnan, C., 2020. Solar dryers for food applications: Concepts, designs, and recent advances. Sol. Energy 208, 321–344. https://doi.org/10.1016/j.solener.2020.07.098

Najib, A., Zarrella, A., Narayanan, V., Grant, P., Harrington, C., 2019. A revised capacitance resistance model for large diameter shallow bore ground heat exchanger. Appl. Therm. Eng. 162, 114305. https://doi.org/10.1016/j.applthermaleng.2019.114305

Nam, Y., Ooka, R., Hwang, S., 2008. Development of a numerical model to predict heat exchange rates for a ground-source heat pump system. Energy Build. 40, 2133–2140. https://doi.org/10.1016/j.enbuild.2008.06.004

Naranjo-Mendoza, C., Oyinlola, M.A., Wright, A.J., Greenough, R.M., 2019. Experimental study of a domestic solar-assisted ground source heat pump with seasonal underground thermal energy storage through shallow boreholes. Appl. Therm. Eng. 162, 114218. https://doi.org/10.1016/j.applthermaleng.2019.114218

Naranjo-Mendoza, C., Wright, A.J., Oyinlola, M.A., Greenough, R.M., 2018. A comparison of analytical and numerical model predictions of shallow soil temperature variation with experimental measurements. Geothermics 76, 38–49. https://doi.org/10.1016/j.geothermics.2018.06.003

Ndiritu, S.W., Engola, M.K., 2020. The effectiveness of feed-in-tariff policy in promoting power generation from renewable energy in Kenya. Renew. Energy 161, 593–605. https://doi.org/10.1016/j.renene.2020.07.082

Nikiforova, T., Savytskyi, M., Limam, K., Bosschaerts, W., Belarbi, R., 2013. Methods and Results of Experimental Researches of Thermal Conductivity of Soils. Energy Procedia 42, 775–783. https://doi.org/10.1016/j.egypro.2013.12.034

Nwaji, G.N., Okoronkwo, C.A., Ogueke, N.V., Anyanwu, E.E., 2019. Hybrid solar water heating/nocturnal radiation cooling system I: A review of the progress, prospects and challenges. Energy Build. 198, 412–430. https://doi.org/10.1016/j.enbuild.2019.06.017

Oh, H., Akar, S., Beckers, K., Bonnema, E., Vivas, C., Salehi, S., 2024. Techno-economic feasibility of geothermal energy production using inactive oil and gas wells for district heating and cooling systems in Tuttle, Oklahoma. Energy Convers. Manag. 308, 118390. https://doi.org/10.1016/j.enconman.2024.118390

Okay, K., Eray, S., Eray, A., 2022. Development of prototype battery management system for PV system. Renew. Energy 181, 1294–1304.

Olabi, A.G., Wilberforce, T., Sayed, E.T., Abo-Khalil, A.G., Maghrabie, H.M., Elsaid, K., Abdelkareem, M.A., 2022. Battery energy storage systems and SWOT (strengths, weakness, opportunities, and threats) analysis of batteries in power transmission. Energy 254, 123987. https://doi.org/10.1016/j.energy.2022.123987

Pan, A., Lu, L., Tian, Y., 2020. A new analytical model for short vertical ground heat exchangers with Neumann and Robin boundary conditions on ground surface. Int. J. Therm. Sci. 152, 106326. https://doi.org/10.1016/j.ijthermalsci.2020.106326

Pandey, A.K., Ali Laghari, I., Reji Kumar, R., Chopra, K., Samykano, M., Abusorrah, A.M., Sharma, K., Tyagi, V.V., 2021. Energy, exergy, exergoeconomic and enviroeconomic (4-E) assessment of solar water heater with/without phase change material for building and other applications: A comprehensive review. Sustain. Energy Technol. Assess. 45, 101139. https://doi.org/10.1016/j.seta.2021.101139

Pang, Z., Niu, F., O'Neill, Z., 2020. Solar radiation prediction using recurrent neural network and artificial neural network: A case study with comparisons. Renew. Energy 156, 279–289. https://doi.org/10.1016/j.renene.2020.04.042

Pintelas, E., Livieris, I.E., Pintelas, P., 2020. A Grey-Box Ensemble Model Exploiting Black-Box Accuracy and White-Box Intrinsic Interpretability. Algorithms 13, 17. https://doi.org/10.3390/a13010017

Plytaria, M.T., Tzivanidis, C., Bellos, E., Antonopoulos, K.A., 2018. Energetic investigation of solar assisted heat pump underfloor heating systems with and without phase change materials. Energy Convers. Manag. 173, 626–639. https://doi.org/10.1016/j.enconman.2018.08.010

Qu, M., Lu, M., Li, Z., Song, X., Chen, J., Ziviani, D., Braun, J.E., 2020. Thermal energy storage based (TES-based) reverse cycle defrosting control strategy optimization for a cascade air source heat pump. Energy Build. 219, 110014. https://doi.org/10.1016/j.enbuild.2020.110014

Ramde, E.W., 2017. Solar Thermal Technologies. Postgraduate Lecture Material (personal communication)

Ramos, A., Chatzopoulou, M.A., Guarracino, I., Freeman, J., Markides, C.N., 2017. Hybrid photovoltaic-thermal solar systems for combined heating , cooling and power provision in the urban environment. Energy Convers. Manag. https://doi.org/10.1016/j.enconman.2017.03.024

Rana, M.M., Uddin, M., Sarkar, M.R., Shafiullah, G.M., Mo, H., Atef, M., 2022. A review on hybrid photovoltaic – Battery energy storage system: Current status, challenges, and future directions. J. Energy Storage 51, 104597. https://doi.org/10.1016/j.est.2022.104597

Rashmi, W., Mahesh, V., Anirban, S., Sharnil, P., Khalid, M., 2021. Hybrid Solar PVT Systems for Thermal Energy Storage: Role of Nanomaterials, Challenges, and Opportunities, in: Tripathi, D., Sharma, R.K. (Eds.), Energy Systems and Nanotechnology, Advances in Sustainability Science and Technology. Springer Singapore, Singapore, pp. 131–160. https://doi.org/10.1007/978-981-16-1256-5_9

Ren, G., Chuttar, A., Banerjee, D., 2022. Exploring efficacy of machine learning (artificial neural networks) for enhancing reliability of thermal energy storage platforms utilizing

phase change materials. Int. J. Heat Mass Transf. 189, 122628. https://doi.org/10.1016/j.ijheatmasstransfer.2022.122628

Salah Saidi, A., 2022. Impact of grid-tied photovoltaic systems on voltage stability of tunisian distribution networks using dynamic reactive power control. Ain Shams Eng. J. 13, 101537. https://doi.org/10.1016/j.asej.2021.06.023

Selamat, S., Miyara, A., Kariya, K., 2016. Numerical study of horizontal ground heat exchangers for design optimization. Renew. Energy 95, 561–573. https://doi.org/10.1016/j.renene.2016.04.042

Sezen, K., Gungor, A., 2023. Comparison of solar assisted heat pump systems for heating residences: A review. Sol. Energy 249, 424–445. https://doi.org/10.1016/j.solener.2022.11.051

Sezen, K., Gungor, A., 2022. Performance analysis of air source heat pump according to outside temperature and relative humidity with mathematical modeling. Energy Convers. Manag. 263, 115702. https://doi.org/10.1016/j.enconman.2022.115702

Shafiullah, M., Ahmed, S.D., Al-Sulaiman, F.A., 2022. Grid Integration Challenges and Solution Strategies for Solar PV Systems: A Review. IEEE Access 10, 52233–52257. https://doi.org/10.1109/ACCESS.2022.3174555

Shoeibi, S., Kargarsharifabad, H., Mirjalily, S.A.A., Muhammad, T., 2022. Solar district heating with solar desalination using energy storage material for domestic hot water and drinking water–environmental and economic analysis. Sustain. Energy Technol. Assess. 49, 101713.

Shrivastava, R.L., Kumar, V., Untawale, S.P., 2017. Modeling and simulation of solar water heater: A TRNSYS perspective. Renew. Sustain. Energy Rev. 67, 126–143. https://doi.org/10.1016/j.rser.2016.09.005

Sukumaran, S., Laht, J., Volkova, A., 2023. Overview of Solar Photovoltaic Applications for District Heating and Cooling. Environ. Clim. Technol. 27, 964–979. https://doi.org/10.2478/rtuect-2023-0070

Tahiri, A., Smith, K.M., Thorsen, J.E., Hviid, C.A., Svendsen, S., 2023. Staged control of domestic hot water storage tanks to support district heating efficiency. Energy 263, 125493. https://doi.org/10.1016/j.energy.2022.125493

Thornton, J.W., Bradley, D.E., Blair, N.J., McDowell, T.P., Duffy, M.J., LaHam, N.D., Naik, A.V., 2014. HVAC Library Mathematical Reference. TESSLibs 17 06.

Toapanta;, L.F., Xavier, A.A., Sarzosa, W.Q., 2020. CFD Analysis of a solar flat plate collector with different cross section. https://doi.org/10.29019/enfoque.v11n2.601

TRNSYS - Official Website [WWW Document], n.d. URL https://sel.me.wisc.edu/trnsys/features/features.html (accessed 2.22.24).

Tu, S., Zhang, X., Zhou, X., 2017. A revised thermal resistance and capacity model for the ground heat exchanger under freezing soil conditions and thermal performance analysis. Procedia Eng. 205, 19–26. https://doi.org/10.1016/j.proeng.2017.09.929

United Nations, 2019. World Population Prospects 2019: Highlights. https://www.un.org/development/desa/publications/world-population-prospects-2019-highlights.html

Vaziri Rad, M.A., Kasaeian, A., Niu, X., Zhang, K., Mahian, O., 2023. Excess electricity problem in off-grid hybrid renewable energy systems: A comprehensive review from challenges to prevalent solutions. Renew. Energy 212, 538–560. https://doi.org/10.1016/j.renene.2023.05.073

Vengadesan, E., Senthil, R., 2020. A review on recent development of thermal performance enhancement methods of flat plate solar water heater. Sol. Energy 206, 935–961. https://doi.org/10.1016/j.solener.2020.06.059

Wang, Y., Wang, J., He, W., 2022. Development of efficient, flexible and affordable heat pumps for supporting heat and power decarbonisation in the UK and beyond: Review and perspectives. Renew. Sustain. Energy Rev. 154, 111747. https://doi.org/10.1016/j.rser.2021.111747

Welsch, B., Göllner-Völker, L., Schulte, D.O., Bär, K., Sass, I., Schebek, L., 2018. Environmental and economic assessment of borehole thermal energy storage in district heating systems. Appl. Energy 216, 73–90. https://doi.org/10.1016/j.apenergy.2018.02.011

Welsch, B., Rühaak, W., Schulte, D.O., Bär, K., Sass, I., 2016. Characteristics of medium deep borehole thermal energy storage: Characteristics of medium deep borehole thermal energy storage. Int. J. Energy Res. 40, 1855–1868. https://doi.org/10.1002/er.3570

Wetter, M., Benne, K., Tummescheit, H., Winther, C., 2023. Spawn: coupling Modelica Buildings Library and EnergyPlus to enable new energy system and control applications. J. Build. Perform. Simul. 1–19. https://doi.org/10.1080/19401493.2023.2266414

Wu, R., Wang, L., Xu, H., Wang, X., Ni, C., Hong, Y., 2022. Energy Efficiency Optimization of CCHP Microgrid Energy Hub with Multiple Scenario Model, in: 2022 5th International Conference on Mechatronics, Robotics and Automation (ICMRA). Presented at the 2022 5th International Conference on Mechatronics, Robotics and Automation (ICMRA), IEEE, Wuhan, China, pp. 172–176. https://doi.org/10.1109/ICMRA56206.2022.10145727

Xue, Z., Ma, H., Wei, Y., Wu, W., Sun, Z., Chai, M., Zhang, C., Chen, Z., 2024. Integrated technological and economic feasibility comparisons of enhanced geothermal systems associated with carbon storage. Appl. Energy 359, 122757. https://doi.org/10.1016/j.apenergy.2024.122757

Yang, T., Liu, W., Kramer, G.J., Sun, Q., 2021. Seasonal thermal energy storage: A techno-economic literature review. Renew. Sustain. Energy Rev. 139, 110732. https://doi.org/10.1016/j.rser.2021.110732

Yang, T., Liu, W., Sun, Q., Hu, W., Kramer, G.J., 2023. Techno-economic-environmental analysis of seasonal thermal energy storage with solar heating for residential heating in China. Energy 283, 128389. https://doi.org/10.1016/j.energy.2023.128389

Yıldız, Ç., Seçilmiş, M., Arıcı, M., Mert, M.S., Nižetić, S., Karabay, H., 2023. An experimental study on a solar-assisted heat pump incorporated with PCM based thermal energy storage unit. Energy 278, 128035. https://doi.org/10.1016/j.energy.2023.128035

Youssef, W., Ge, Y.T., Tassou, S.A., 2017. Effects of latent heat storage and controls on stability and performance of a solar assisted heat pump system for domestic hot water production. Sol. Energy 150, 394–407. https://doi.org/10.1016/j.solener.2017.04.065

Zhang, M., Yan, T., Wang, W., Jia, X., Wang, J., Klemeš, J.J., 2022. Energy-saving design and control strategy towards modern sustainable greenhouse: A review. Renew. Sustain. Energy Rev. 164, 112602. https://doi.org/10.1016/j.rser.2022.112602

Zhou, J., Zeng, C., Wang, Z., Lyu, W., Tang, Y., Wu, D., Ji, W., Yuan, Y., 2022. Indirect expansion solar assisted heat pump system: A review. Sustain. Energy Technol. Assess. 53, 102409. https://doi.org/10.1016/j.seta.2022.102409

Zou, L., Liu, Y., Yu, M., Yu, J., 2023. A review of solar assisted heat pump technology for drying applications. Energy **283,** 129215. https://doi.org/10.1016/j.energy.2023.129215

Internet References

IEA, 2023. World Energy Outlook 2023. Int. Energy Agency.

IEA, 2022. World Energy Outlook 2022. Int. Energy Agency.

IEA, 2019. World Energy Outlook 2019. World Energy Outlook 2019 1.

APPENDICES

In this section the detailed description of materials relevant for further understanding of the current research work is presented. It provides the supplementary result data sheet, as well as the detailed TRNSYS and MATLAB models with the corresponding code for training of the MATLAB model. The detail table of results for all the parametric analysis carried out are presented in Table A-1 to Table A-4. Due to the large nature of the TRNSYS and MATLAB models, they may be difficult to view. However, zooming to appropriate percent allows the viewing of a particular detail.

Table A- 1: Summary result for effects of PV size on the model performance

E_{HnC} for conventional case = 36590.06 kWh													
PV Size (m2)	$Q_{utes,d}$ (kWh)	$Q_{utes,c}$ (kWh)	$E_{pv,HnC}$ (kWh)	$E_{pv,P2HC}$ (kWh)	$E_{pv,etc}$ (kWh)	$E_{pv,total}$ (kWh)	$E_{pv,used}$ (kWh)	$E_{pv,surplus}$ (kWh)	UTES Thermal Efficiency (%)	Energy Savings (%)	P2HC Efficiency (%)	SCR (%)	SEUR (%)
1200	14816.75	26774.15	31145.00	0.00	77582.43	108727.42	108727.42	0.00	55.34	14.88	69.58	100.00	-
1600	16570.09	38226.89	31032.00	2825.39	99652.26	144972.31	142146.93	2825.39	43.35	15.19	48.49	98.05	100.00
2000	17151.41	42917.88	30782.33	14298.24	121562.31	181217.16	166642.88	14574.28	39.96	15.87	40.62	91.96	98.11
2400	18021.70	48280.06	31002.31	16806.01	142989.28	217461.98	190797.60	26664.38	37.33	15.27	33.25	87.74	63.03
2800	18321.49	50665.98	30966.75	18771.69	164666.55	253706.81	214404.98	39301.82	36.16	15.37	29.96	84.51	47.76
3200	18507.16	53137.14	30508.97	20021.68	183253.39	289951.68	233784.04	56167.64	34.83	16.62	30.37	80.63	35.65
3600	18813.82	55080.25	30922.27	21039.13	193783.45	326196.44	245744.85	80451.59	34.16	15.49	26.94	75.34	26.15
4000	19064.48	55400.04	30909.60	22120.39	204661.72	362441.28	257691.71	104749.57	34.41	15.52	25.68	71.10	21.12
4400	19328.78	57268.04	30803.92	22453.57	215438.25	398686.13	268695.75	129990.39	33.75	15.81	25.77	67.40	17.27
4800	19430.45	57975.22	30846.49	23236.36	226409.46	434930.97	280492.32	154438.66	33.52	15.70	24.72	64.49	15.05
5200	19668.26	58537.53	30749.65	23695.43	237203.10	471175.80	291648.18	179527.62	33.60	15.96	24.65	61.90	13.20
5600	19754.34	58631.76	30892.79	23994.00	247949.24	507420.62	302836.03	204584.60	33.69	15.57	23.74	59.68	11.73

Table A- 2: Summary result for effects of UTES size on the model performance

E_{HnC} for conventional case = 36590.06 kWh													
UTES Volume (m3)	$Q_{utes,d}$ (kWh)	$Q_{utes,c}$ (kWh)	E_{HnC} (kWh)	$E_{PV,P2HC}$ (kWh)	$E_{pv,etc}$ (kWh)	$E_{PV,total}$ (kWh)	$E_{pv,used}$ (kWh)	$E_{PV,surplus}$ (kWh)	UTES Thermal Efficiency (%)	Energy Savings (%)	P2HC Efficiency (%)	SCR (%)	SEUR (%)
100	3107.14	6303.55	31793.92	31793.92	204000.77	362441.06	256603.98	105837.08	49.29	13.01	22.91	70.80	19.63
220	6593.69	13710.32	31489.73	31489.73	204029.94	362441.06	257029.21	105411.85	48.09	13.68	23.37	70.92	20.31
340	9594.71	21260.36	31327.76	31327.76	204538.15	362441.09	256978.99	105462.10	45.13	14.52	25.10	70.90	20.07
460	12294.05	29213.98	31604.25	31604.25	204361.03	362441.20	256916.63	105524.57	42.08	14.28	24.66	70.89	20.08
580	14728.15	38215.79	31056.50	31056.50	204631.75	362441.12	257139.03	105302.09	38.54	15.70	26.52	70.95	20.57
700	16545.52	47985.84	30737.35	30737.35	204791.81	362441.22	257445.29	104995.92	34.48	16.44	27.24	71.03	21.03
820	19141.15	56580.39	30572.67	30572.67	204846.49	362441.29	257740.16	104701.13	33.83	16.07	26.50	71.11	21.19
940	21806.85	66168.18	30785.43	30785.43	204745.33	362441.39	257486.18	104955.21	32.96	16.19	26.83	71.04	21.03
1060	23554.63	76912.14	30732.99	30732.99	204974.00	362441.47	257552.62	104888.85	30.63	16.87	27.86	71.06	21.13
1180	23827.25	83910.78	30771.08	30771.08	204719.59	362441.47	257370.72	105070.75	28.40	16.42	27.23	71.01	21.01
1300	24359.08	88452.79	30614.97	30614.97	204874.91	362441.50	257294.84	105146.67	27.54	16.16	27.19	70.99	20.68
1420	25266.40	92887.74	30459.35	30459.35	204240.73	362441.54	256630.49	105811.05	27.20	15.62	26.56	70.81	20.33

Table A- 3: Summary result for effects of P2C duration on the model performance

E_{HnC} for conventional case = 36590.06 kWh													
P2C Time (hrs)	$Q_{utes,d}$ (kWh)	$Q_{utes,c}$ (kWh)	E_{HnC} (kWh)	$E_{PV,P2HC}$ (kWh)	$E_{pv,etc}$ (kWh)	$E_{PV,total}$ (kWh)	$E_{pv,used}$ (kWh)	$E_{PV,surplus}$ (kWh)	UTES Thermal Efficiency (%)	Energy Savings (%)	P2HC Efficiency (%)	SCR (%)	SEUR (%)
2160	19993.58	62943.45	30853.82	27137.01	204930.49	362440.96	262921.32	99519.65	31.76	15.68	21.14	72.54	27.27
2232	19968.92	62558.79	30921.38	26582.94	204765.00	362441.02	262269.32	100171.70	31.92	15.49	21.32	72.36	26.54
2304	19841.44	61865.87	30646.45	26158.86	205050.89	362441.06	261856.20	100584.86	32.07	16.24	22.72	72.25	26.01
2376	19761.26	60950.70	30880.96	25429.38	204638.09	362441.03	260948.43	101492.60	32.42	15.60	22.45	72.00	25.06
2448	19109.17	59663.22	30887.01	24373.18	204660.25	362441.16	259920.44	102520.72	32.03	15.59	23.40	71.71	23.77
2520	19149.04	60348.58	31167.81	23743.13	204296.18	362441.20	259207.11	103234.09	31.73	14.82	22.84	71.52	23.00
2592	19165.19	58867.13	30885.14	23440.34	204625.31	362441.17	258950.78	103490.39	32.56	15.59	24.34	71.45	22.65
2664	19266.16	58391.00	30794.96	23000.16	204549.22	362441.30	258344.34	104096.95	33.00	15.84	25.20	71.28	22.09
2736	18998.31	56950.79	30677.35	22107.84	204906.67	362441.30	257691.86	104749.44	33.36	16.16	26.74	71.10	21.14
2808	18774.23	56064.01	30899.72	21612.60	204527.09	362441.38	257039.40	105401.98	33.49	15.55	26.33	70.92	20.50
2880	18558.30	53779.03	30801.08	20543.45	204847.70	362441.40	256192.23	106249.17	34.51	15.82	28.18	70.69	19.34
2952	18603.09	53560.01	30984.17	20165.05	204636.87	362441.40	255786.09	106655.31	34.73	15.32	27.80	70.57	18.91

Table A- 4: Summary result for effects of P2H duration on the model performance

E_{HnC} for conventional case = 36590.06 kWh													
P2H Time (hrs)	$Q_{utes,d}$ (kWh)	$Q_{utes,c}$ (kWh)	E_{HnC} (kWh)	$E_{PV,P2HC}$ (kWh)	$E_{pv,etc}$ (kWh)	$E_{PV,total}$ (kWh)	$E_{pv,used}$ (kWh)	$E_{PV,surplus}$ (kWh)	UTES Thermal Efficiency (%)	Energy Savings (%)	P2HC Efficiency (%)	SCR (%)	SEUR (%)
5832	20145.97	67461.89	30752.43	28227.03	204919.56	362441.12	263899.02	98542.09	29.86	15.95	20.68	72.81	28.64
5904	20145.97	67461.89	30752.43	28227.03	204919.56	362441.12	263899.02	98542.09	29.86	15.95	20.68	72.81	28.64
5976	20145.97	67461.89	30752.43	28227.03	204919.56	362441.12	263899.02	98542.09	29.86	15.95	20.68	72.81	28.64
6048	20145.97	67461.89	30752.43	28227.03	204919.56	362441.12	263899.02	98542.09	29.86	15.95	20.68	72.81	28.64
6120	20145.97	67461.89	30752.43	28227.03	204919.56	362441.12	263899.02	98542.09	29.86	15.95	20.68	72.81	28.64
6192	20052.13	66892.14	30806.02	26927.70	204845.84	362441.19	262579.56	99861.63	29.98	15.81	21.48	72.45	26.97
6264	19961.20	63774.64	30909.81	25945.43	204727.89	362441.18	261583.13	100858.06	31.30	15.52	21.89	72.17	25.72
6336	19984.35	60473.70	30678.00	24496.86	204940.32	362441.17	260115.17	102325.99	33.05	16.16	24.13	71.77	23.94
6408	19389.45	57857.44	30784.72	23055.48	204812.72	362441.28	258652.92	103788.36	33.51	15.87	25.18	71.36	22.21
6480	18998.31	56950.79	30677.35	22107.84	204906.67	362441.30	257691.86	104749.44	33.36	16.16	26.74	71.10	21.11
6552	18950.23	54671.64	30722.31	21053.07	204846.05	362441.35	256621.43	105819.91	34.66	16.04	27.87	70.80	19.90
6624	18824.37	52140.51	30884.56	19911.12	204666.65	362441.35	255462.33	106979.03	36.10	15.59	28.65	70.48	18.61

Figure A- 1: MATLAB Simulink Model

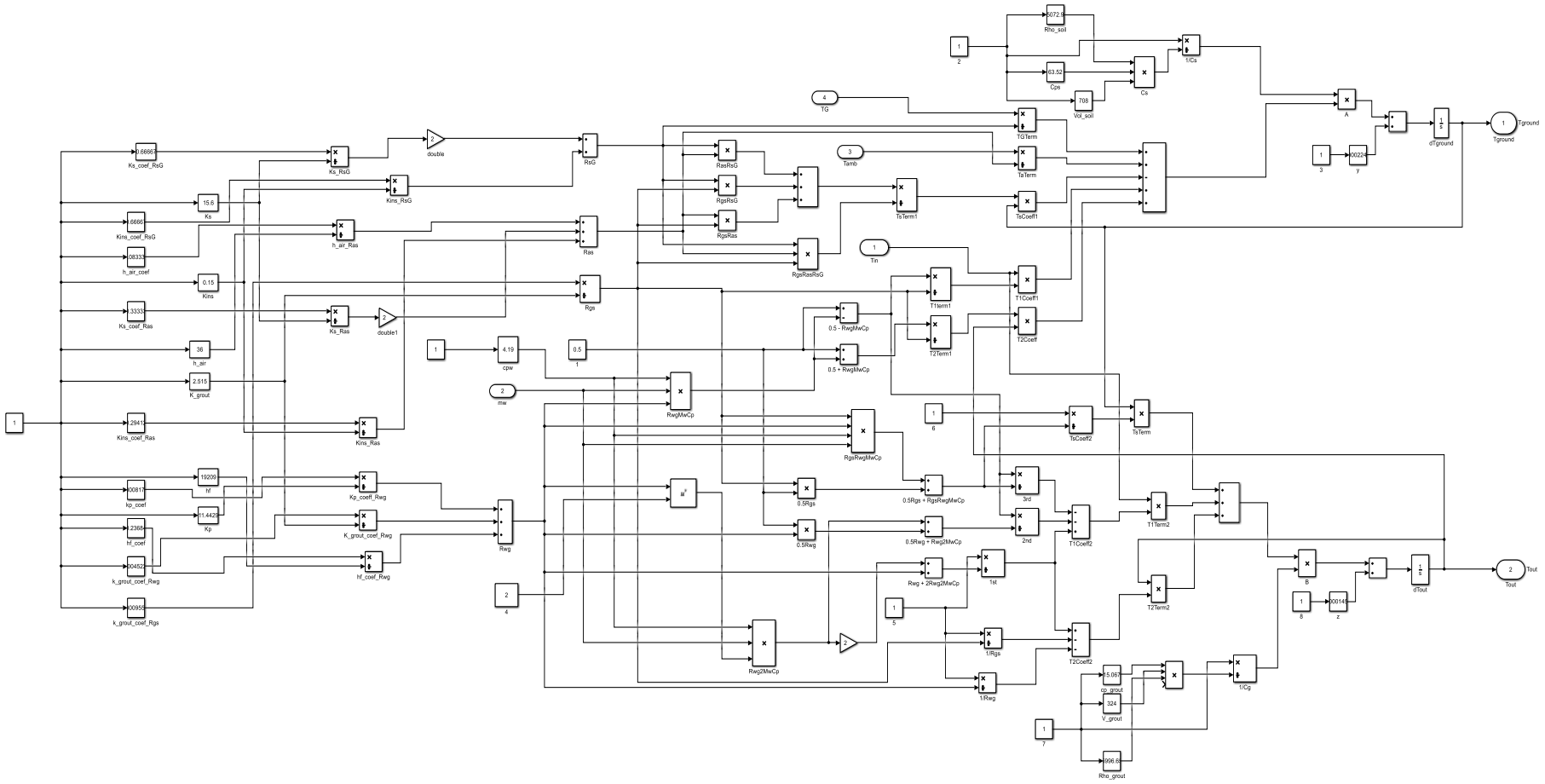

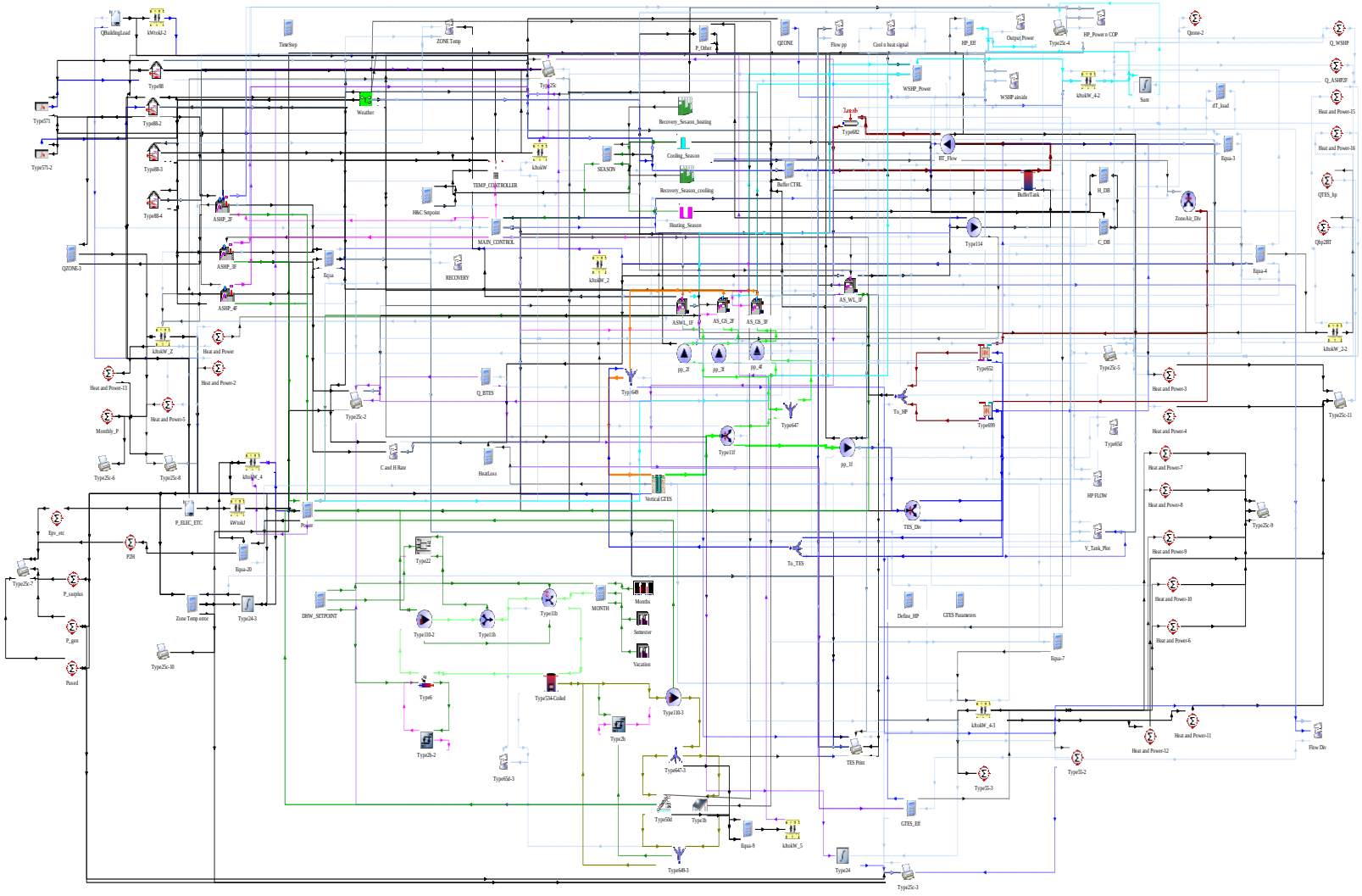

Figure A- 2: TRNSYS Model for the overall system configuration and control strategy

A.1 Matlab Training Code:

```
function [pOpt, Info] = spe_Horizontal_Model_With_TG_0227(p)
%SPE_HORIZONTAL_MODEL_WITH_TG_0227
% Solve a parameter estimation problem for the Horizontal_Model_With_TG_0227 model.
% The function returns estimated parameter values, pOpt,
% and estimation termination information, Info.
% The input argument, p, defines the model parameters to estimate,
% if omitted the parameters specified in the function body are estimated.
% Modify the function to include or exclude new experiments or
% change the estimation options.
% Auto-generated by SPETOOL on 16-May-2024 15:29:23.

%% Open the model.
open_system('Horizontal_Model_With_TG_0227')

%% Specify Model Parameters to Estimate
if nargin < 1 || isempty(p)
    p =
sdo.getParameterFromModel('Horizontal_Model_With_TG_0227',{'Rho_grout','Rho_soil','cpg','cps','y','z','Ks','
Kp','K_grout','Kins','h_air','hf'});
    p(1).Minimum = 1200;
    p(1).Maximum = 10000;
    p(2).Minimum = 1200;
    p(2).Maximum = 10000;
    p(3).Minimum = 10;
    p(3).Maximum = 300;
    p(3).Scale = 16;
    p(4).Minimum = 30;
    p(4).Maximum = 300;
    p(4).Scale = 64;
    p(5).Scale = 0.000244140625;
    p(6).Scale = 0.000244140625;
    p(7).Minimum = 4.6;
    p(7).Maximum = 16;
    p(8).Minimum = 1.44;
    p(8).Maximum = 12;
    p(9).Minimum = 2.5;
    p(9).Maximum = 12;
    p(10).Minimum = 0.2;
    p(10).Maximum = 0.8;
    p(11).Minimum = 9;
    p(11).Maximum = 90;
    p(12).Minimum = 14700;
    p(12).Maximum = 32000;
end

%% Define the Estimation Experiments
%

Exp = sdo.Experiment('Horizontal_Model_With_TG_0227');

%%
% Specify the experiment input data used to generate the output.
Exp_Sig_Input_1 = Simulink.SimulationData.Signal;
Exp_Sig_Input_1.Values      = getData('Exp_Sig_Input_1_Value');
Exp_Sig_Input_1.BlockPath = 'Horizontal_Model_With_TG_0227/Tin';
Exp_Sig_Input_1.PortType    = 'outport';
```

```
Exp_Sig_Input_1.PortIndex = 1;
Exp_Sig_Input_1.Name          = 'Tin';
Exp_Sig_Input_2 = Simulink.SimulationData.Signal;
Exp_Sig_Input_2.Values        = getData('Exp_Sig_Input_2_Value');
Exp_Sig_Input_2.BlockPath = 'Horizontal_Model_With_TG_0227/mw';
Exp_Sig_Input_2.PortType    = 'outport';
Exp_Sig_Input_2.PortIndex = 1;
Exp_Sig_Input_2.Name          = 'mw';
Exp_Sig_Input_3 = Simulink.SimulationData.Signal;
Exp_Sig_Input_3.Values        = getData('Exp_Sig_Input_3_Value');
Exp_Sig_Input_3.BlockPath = 'Horizontal_Model_With_TG_0227/Tamb';
Exp_Sig_Input_3.PortType    = 'outport';
Exp_Sig_Input_3.PortIndex = 1;
Exp_Sig_Input_3.Name          = 'Tamb';
Exp_Sig_Input_4 = Simulink.SimulationData.Signal;
Exp_Sig_Input_4.Values        = getData('Exp_Sig_Input_4_Value');
Exp_Sig_Input_4.BlockPath = 'Horizontal_Model_With_TG_0227/TG';
Exp_Sig_Input_4.PortType    = 'outport';
Exp_Sig_Input_4.PortIndex = 1;
Exp_Sig_Input_4.Name          = 'TG';
Exp.InputData = [Exp_Sig_Input_1; Exp_Sig_Input_2; Exp_Sig_Input_3; Exp_Sig_Input_4];

%%
% Specify the experiment input data used to generate the output.
Exp_Sig_Output = Simulink.SimulationData.Signal;
Exp_Sig_Output.Values        = getData('Exp_Sig_Output_Value');
Exp_Sig_Output.BlockPath = 'Horizontal_Model_With_TG_0227/dTout';
Exp_Sig_Output.PortType    = 'outport';
Exp_Sig_Output.PortIndex = 1;
Exp_Sig_Output.Name          = 'Tout';
Exp.OutputData = Exp_Sig_Output;

%%
% Specify the experiment initial states.
State =
sdo.getStateFromModel('Horizontal_Model_With_TG_0227',{'Horizontal_Model_With_TG_0227/dTout'});
State(1).Value = 16.16100822064208;
Exp.InitialStates = State;

%%
% Create a model simulator from an experiment
Simulator = createSimulator(Exp);

%%
% Add experiment specific parameters/states to the list of parameters
% to estimate.
s = getValuesToEstimate(Exp);
p = [p; s];

%% Create Estimation Objective Function
%
% Create a function that is called at each optimization iteration
% to compute the estimation cost.
%
% Use an anonymous function with one argument that calls Horizontal_Model_With_TG_0227_optFcn.
optimfcn = @(P) Horizontal_Model_With_TG_0227_optFcn(P,Simulator,Exp);

%% Optimization Options
```

```
%
% Specify optimization options.
Options = sdo.OptimizeOptions;
Options.Method = 'lsqnonlin';
Options.OptimizedModel = Simulator;

%% Estimate the Parameters
%
% Call sdo.optimize with the estimation objective function handle,
% parameters to estimate, and options.
[pOpt,Info] = sdo.optimize(optimfcn,p,Options);

%%
% Update the experiments with the estimated parameter values.
Exp = setEstimatedValues(Exp,pOpt);

%% Update Model
%
% Update the model with the optimized parameter values.
sdo.setValueInModel('Horizontal_Model_With_TG_0227',pOpt(1:12));
end

function Vals = Horizontal_Model_With_TG_0227_optFcn(P,Simulator,Exp)
%HORIZONTAL_MODEL_WITH_TG_0227_OPTFCN
%
% Function called at each iteration of the estimation problem.
%
% The function is called with a set of parameter values, P, and returns
% the estimation cost, Vals, to the optimization solver.
%
% See the sdoExampleCostFunction function and sdo.optimize for a more
% detailed description of the function signature.
%

%%
% Define a signal tracking requirement to compute how well the model
% output matches the experiment data.
r = sdo.requirements.SignalTracking(...
       'Method', 'Residuals');
%%
% Update the experiment(s) with the estimated parameter values.
Exp = setEstimatedValues(Exp,P);

%%
% Simulate the model and compare model outputs with measured experiment
% data.
F_r = [];
Simulator = createSimulator(Exp,Simulator);
Simulator = sim(Simulator);

SimLog = find(Simulator.LoggedData,get_param('Horizontal_Model_With_TG_0227','SignalLoggingName'));
Sig = find(SimLog,Exp.OutputData.Name);

Error = evalRequirement(r,Sig.Values,Exp.OutputData.Values);
F_r = [F_r; Error(:)];

%% Return Values.
%
```

```
% Return the evaluated estimation cost in a structure to the
% optimization solver.
Vals.F = F_r;
end

function Data = getData(DataID)
%GETDATA
%
% Helper function to store data used by spe_Horizontal_Model_With_TG_0227.
%
% The input, DataID, specifies the name of the data to retrieve. The output,
% Data, contains the requested data.
%

SaveData = load('spe_Horizontal_Model_With_TG_0227_Data');
Data = SaveData.Data.(DataID);
end
```

A.2 Publications from the Study

Below is the list of published articles from this research, including a conference paper.

Eze, F., Lee, W., An, Y. S., Joo, H., Lee, K., Ogola, J., and Mwabora, J. (2024). Experimental and simulated evaluation of inverse model for shallow underground thermal storage. *Case Studies in Thermal Engineering*, *59*, 104535. https://doi.org/10.1016/j.csite.2024.104535

Eze, F., Lee, W.-J., An, Y. S., Joo, H., Lee, K., Ogola, J., and Mwabora, J. (2024). Development and simulated evaluation of inter-seasonal power-to-heat and power-to-cool with underground thermal storage for self-consumption of surplus solar energy in buildings. *Energy Conversion and Management*, *320*, 119013. https://doi.org/10.1016/j.enconman.2024.119013

Eze, F., Egbo, M., Anuta, U. J., Ntiriwaa, O.-B. R., Ogola, J., and Mwabora, J. (2024). A review on solar water heating technology: Impacts of parameters and techno-economic studies. *Bulletin of the National Research Centre*, *48*(1), 29. https://doi.org/10.1186/s42269-024-01187-1

Eze, F., Lee, W., An, Y., Joo, H., Lee, K., Ogola, J., and Mwabora, J. (2023). Calibrated Models of Shallow Ground Thermal Energy Storage for Heating and Cooling Applications. *Proceeding of International Heat Transfer Conference 17*, 9. https://doi.org/10.1615/IHTC17.430-180

International Conference Presentations

Eze, F., Lee, W., An, Y., Joo, H., Lee, K., Ogola, J., and Mwabora, J. (2023). Calibrated Models of Shallow Ground Thermal Energy Storage for Heating and Cooling Applications. *17th International Heat Transfer Conference Cape Town, South Africa*.

Eze, F., Lee, W., An, Y., Joo, H., Lee, K., Ogola, J., and Mwabora, J. (2023). Simulation on the Potential of Long-Term Thermal Energy Storage: Application with Ideal Thermal Energy Storage in Heat Pump for Inter-Seasonal Use of Surplus Solar Energy in Buildings. *12th Asia-Pacific Forum on Renewable Energy, Jeju Island, South Korea Pg 322 -322.*